# A COMPUTATIONAL STUDY OF INTERFACIAL INSTABILITIES IN THE INTERSTELLAR MEDIUM

By

ROBERT M. HUECKSTAEDT

A DISSERTATION PRESENTED TO THE GRADUATE SCHOOL
OF THE UNIVERSITY OF FLORIDA IN PARTIAL FULFILLMENT
OF THE REQUIREMENTS FOR THE DEGREE OF
DOCTOR OF PHILOSOPHY

UNIVERSITY OF FLORIDA

2001

# ACKNOWLEDGEMENTS

Throughout the process of conducting research and preparing this manuscript, I have been fortunate to receive advice and assistance from many people. I am particularly indebted to my advisor, James Hunter Jr., for his guidance. I am grateful to all members of my graduate committee for their many helpful suggestions. I also thank Haywood Smith Jr. and Richard Lyon for their assistance as I sally forth into the postdoc market.

The primary code used for this study was made available from Los Alamos National Laboratory in part through the efforts of R.W. Whitaker. I am especially grateful to N.T. Padial and B.A. Kashiwa for their help in modifying the code for astrophysical use. Their patience and willingness to answer questions is exemplary. I'd also like to thank J. Adams for making his code publicly available. The cooling rates used in this study were supplied by D. Neufeld. The widget tools made available by R. Piña helped speed up my analysis considerably.

We are fortunate in this department to have a tremendous office staff who make our lives easier. I am grateful to Glenda Smith, Ann Elton, Audrey Sims, and Debra Hunter for all of those things they do. I would also like to thank my fellow graduate students for making UF such a welcome place. A large part of the soundtrack for the past year was due to Elvis Costello and Ana Gabriel. Their contributions are appreciated. I recognize the contributions made throughout the centuries by the great men and women of science who have made possible the things we accomplish today.

On a more personal note, I give special thanks to my office-mate and friend Tomas Waldemarsson. I find it no coincidence that many of the good times I've known during my time in Gainesville have involved Tomas and his soon-to-be better half Karen. Lastly, I thank T.Jay Vaccaro for being a fellow Lightning fan in the worst of times, and I thank Lisa Ojanen for being the very embodiment of the best of times.

## TABLE OF CONTENTS

ACKNOWLEDGEMENTS . . . . . . . . . . . . . . . . . . . . . . . . . . . ii

LIST OF TABLES . . . . . . . . . . . . . . . . . . . . . . . . . . . . vi

LIST OF FIGURES . . . . . . . . . . . . . . . . . . . . . . . . . . . vii

ABSTRACT . . . . . . . . . . . . . . . . . . . . . . . . . . . . . . . xii

CHAPTERS

1 INTRODUCTION . . . . . . . . . . . . . . . . . . . . . . . . . . 1

- 1.1 Molecular Clouds and Star Formation . . . . . . . . . . . . . . . 1
- 1.2 Hydrodynamic Simulations of the ISM . . . . . . . . . . . . . . . 4
- 1.3 Thesis Structure . . . . . . . . . . . . . . . . . . . . . . . . . 6

2 COMPUTATIONAL TECHNIQUES . . . . . . . . . . . . . . . . . . 8

- 2.1 The Hydrodynamic Code . . . . . . . . . . . . . . . . . . . . . . 8
- 2.2 Self-Gravity Routines . . . . . . . . . . . . . . . . . . . . . . . 19
- 2.3 Cooling Routines . . . . . . . . . . . . . . . . . . . . . . . . . 28

3 SELF-GRAVITY DRIVEN INTERFACIAL INSTABILITIES . . . . . 34

- 3.1 Theory . . . . . . . . . . . . . . . . . . . . . . . . . . . . . . 34
- 3.2 Models . . . . . . . . . . . . . . . . . . . . . . . . . . . . . . 38
- 3.3 Results for Unperturbed Models . . . . . . . . . . . . . . . . . . 46
- 3.4 Results for Perturbed Models . . . . . . . . . . . . . . . . . . . 49
  - 3.4.1 Moderate Temperature Models . . . . . . . . . . . . . . . 52
  - 3.4.2 High Temperature Models . . . . . . . . . . . . . . . . . 55
  - 3.4.3 Low Temperature Models . . . . . . . . . . . . . . . . . 71
- 3.5 Discussion . . . . . . . . . . . . . . . . . . . . . . . . . . . . 92

4 COLLIDING GAS FLOWS IN CARTESIAN GEOMETRY . . . . . . 95

- 4.1 Background . . . . . . . . . . . . . . . . . . . . . . . . . . . . 96
- 4.2 Models . . . . . . . . . . . . . . . . . . . . . . . . . . . . . . 99
- 4.3 Results . . . . . . . . . . . . . . . . . . . . . . . . . . . . . . 101
  - 4.3.1 Earlier Perturbation Time . . . . . . . . . . . . . . . . . 108
  - 4.3.2 Later Perturbation Time . . . . . . . . . . . . . . . . . . 122
- 4.4 Discussion . . . . . . . . . . . . . . . . . . . . . . . . . . . . 132

5 COLLIDING FLOWS IN CYLINDRICAL GEOMETRY . . . . . . . . 134

5.1 Models . . . . . . . . . . . . . . . . . . . . . . . . . . . . . . 134
5.2 Results . . . . . . . . . . . . . . . . . . . . . . . . . . . . . . 136
5.2.1 Free Outer Boundaries and Full Cooling . . . . . . . . . . . 143
5.2.2 Reflective Outer Boundaries and Full Cooling . . . . . . . . 154
5.2.3 Free Outer Boundaries and Reduced Cooling . . . . . . . . 158
5.2.4 Different Minimum Temperatures . . . . . . . . . . . . . . 170
5.2.5 Higher Initial Velocities . . . . . . . . . . . . . . . . . . . . 176
5.3 Discussion . . . . . . . . . . . . . . . . . . . . . . . . . . . . . 181

6 CONCLUDING REMARKS . . . . . . . . . . . . . . . . . . . . . . 189

6.1 The Self-Gravity Interfacial Instability . . . . . . . . . . . . . . . 189
6.2 The Nonlinear Thin Shell Instability . . . . . . . . . . . . . . . . 191
6.3 Further Considerations . . . . . . . . . . . . . . . . . . . . . . . 192

REFERENCES . . . . . . . . . . . . . . . . . . . . . . . . . . . . . . 194

BIOGRAPHICAL SKETCH . . . . . . . . . . . . . . . . . . . . . . . 197

# LIST OF TABLES

3.1 Comparison of numerical and analytical results . . . . . . . . . . . . . 42

3.2 Model Parameters . . . . . . . . . . . . . . . . . . . . . . . . . . . . . . 51

3.3 Experimental growth rates for SGI and RT models . . . . . . . . . . . 93

5.1 Maximum densities at $t = 1.1 \times 10^{13} s$ . . . . . . . . . . . . . . . . . . . . 170

## LIST OF FIGURES

2.1 Chart of subroutines called by CFDLIB main program. . . . . . . . . 9

2.2 Configuration of the Rayleigh-Taylor simulation. . . . . . . . . . . . . . 18

2.3 Rayleigh-Taylor instability growth. . . . . . . . . . . . . . . . . . . . . 20

2.4 An example of switching grid resolutions to alter the nature of a function. 24

2.5 A schematic look at the grid schedule in the FMV method. . . . . . . 25

2.6 Initial density distribution for the collapsing sphere. . . . . . . . . . . 27

2.7 Comparison between numerical and analytical methods for calculating the potential of a solid sphere. . . . . . . . . . . . . . . . . . . . . . . . 29

2.8 Time evolution of a collapsing sphere. . . . . . . . . . . . . . . . . . . 30

2.9 Cooling rates. . . . . . . . . . . . . . . . . . . . . . . . . . . . . . . 32

3.1 Initial density and temperature distributions for SGI model cnsg257e1. 43

3.2 Initial density and temperature distributions for RT model cart257e1. 46

3.3 Pressure comparison for model cnsg257d0 at $t=0$ and $t=10t_e$. . . . . 47

3.4 Pressure comparison for model cnsg257e0 at $t=0$ and $t=10t_e$. . . . . 48

3.5 Pressure comparison for model cart257d0 at $t=0$ and $t=10t_e$. . . . . 49

3.6 Pressure comparison for model cart257e0 at $t=0$ and $t=10t_e$. . . . . 50

3.7 Evolution of the SGI for model masg129d1. . . . . . . . . . . . . . . . 53

3.8 Comparison of moderate temperature models with varying $k_x$. . . . . 54

3.9 Evolution of the SGI for model hasg129d1. . . . . . . . . . . . . . . . 56

3.10 Evolution of the SGI for model hasg257d1. . . . . . . . . . . . . . . . 57

3.11 Velocity growth for model hasg257d1. . . . . . . . . . . . . . . . . . . 59

3.12 Evolution of the SGI for model hnsg257d1. . . . . . . . . . . . . . . . 60

3.13 Model hnsg257d1 at $t=5t_e$. . . . . . . . . . . . . . . . . . . . . . . . 61

3.14 Velocity growth for model hnsg257d1. . . . . . . . . . . . . . . . . . . . 63

3.15 Evolution of the RT instability for model hart257d1. . . . . . . . . . . 64

3.16 Velocity growth for RT model hart257d1. . . . . . . . . . . . . . . . . . 65

3.17 Evolution of the SGI for model hnsg257d2. . . . . . . . . . . . . . . . . 67

3.18 Evolution of the RT instability for model hart257d2. . . . . . . . . . . 68

3.19 Velocity growth for SGI model hnsg257d2. . . . . . . . . . . . . . . . . 69

3.20 Velocity growth for RT model hart257d2. . . . . . . . . . . . . . . . . . 70

3.21 Evolution of the SGI for model cnsg257e1. . . . . . . . . . . . . . . . . 72

3.22 Evolution of the RT instability for model cart257e1. . . . . . . . . . . 73

3.23 Velocity growth for SGI model cnsg257e1. . . . . . . . . . . . . . . . . 75

3.24 Velocity growth for RT model cart257e1. . . . . . . . . . . . . . . . . . 76

3.25 Comparison of cold SGI models with varying $k_x$. . . . . . . . . . . . . . 77

3.26 Evolution of the SGI for model cnsg257d2. . . . . . . . . . . . . . . . . 79

3.27 Velocity growth for RT model cnsg257d2. . . . . . . . . . . . . . . . . . 80

3.28 Evolution of the RT instability for model cart257d2. . . . . . . . . . . 81

3.29 Velocity growth for RT model cart257d2. . . . . . . . . . . . . . . . . . 82

3.30 Evolution of the SGI for model cnsg257d1. . . . . . . . . . . . . . . . . 84

3.31 Velocity growth for SGI model cnsg257d1. . . . . . . . . . . . . . . . . 85

3.32 Evolution of the RT instability for model cart257d1. . . . . . . . . . . 87

3.33 Velocity growth for RT model cart257d1. . . . . . . . . . . . . . . . . . 88

3.34 Evolution of the SGI for model cnsg257d3. . . . . . . . . . . . . . . . . 89

3.35 Model cnsg257d3 at $t = 5t_e$. . . . . . . . . . . . . . . . . . . . . . . . . 90

3.36 Velocity growth for SGI model cnsg257d3. . . . . . . . . . . . . . . . . 91

4.1 Propagation of an adiabatic $\gamma = 1.4$ accretion shock. . . . . . . . . . 103

4.2 Adiabatic accretion shock line cuts at $t = 0.8 \times 10^{12} s$ . . . . . . . . . 104

4.3 Instability development for an unperturbed slab with $q = 1$. . . . . . 105

4.4 Instability development for an unperturbed slab with $q = 0.3$. . . . . 106

4.5 Temperature profiles for unperturbed models at $1.5 \times 10^{13}s$. . . . . . 107

4.6 Instability development for a perturbed slab with $q = 1$. . . . . . . . 109

4.7 Instability development for a perturbed slab with $q = 0.8$. . . . . . . . 110

4.8 Instability development for a perturbed slab with $q = 0.6$. . . . . . . . 111

4.9 Instability development for a perturbed slab with $q = 0.4$. . . . . . . . 112

4.10 Instability development for a perturbed slab with $q = 0.3$. . . . . . . . 113

4.11 Instability development for a perturbed slab with $q = 0.2$. . . . . . . . 114

4.12 Instability development for a perturbed slab with $q = 0.1$. . . . . . . . 115

4.13 Perturbed slab morphology for a $q = 1$ model at $t = 1.1 \times 10^{13}s$. . . . 117

4.14 Perturbed slab morphology for a $q = 0.3$ model at $t = 1.1 \times 10^{13}s$. . . 118

4.15 Morphology for a $q = 0.3$ model perturbed with a sine function. . . . 120

4.16 Morphology of a self-gravitating, perturbed slab with $q = 1$ at $t = 1.1 \times 10^{13}s$. . . . . . . . . . . . . . . . . . . . . . . . . . . . 121

4.17 Morphology of a self-gravitating, perturbed slab with $q = 0.3$ at $t = 1.1 \times 10^{13}s$. . . . . . . . . . . . . . . . . . . . . . . . . . . . 123

4.18 Evolution of a $q = 1$ model perturbed at $1.0 \times 10^{13}s$. . . . . . . . . . 124

4.19 Perturbed slab morphology for a $q = 1$ model at $t = 1.6 \times 10^{13}s$. . . . 125

4.20 Evolution of a $q = 0.3$ model perturbed at $1.0 \times 10^{13}s$. . . . . . . . . 127

4.21 Perturbed slab morphology for a $q = 0.3$ model at $t = 1.6 \times 10^{13}s$. . . 128

4.22 Morphology of a self-gravitating, perturbed slab with $q = 1$ at $t = 1.6 \times 10^{13}s$. . . . . . . . . . . . . . . . . . . . . . . . . . . . 130

4.23 Morphology of a self-gravitating, perturbed slab with $q = 0.3$ at $t = 1.6 \times 10^{13}s$. . . . . . . . . . . . . . . . . . . . . . . . . . . . 131

5.1 Onset of instability in an unperturbed $q = 1$ disk. . . . . . . . . . . . 137

5.2 Onset of instability in an unperturbed $q = 0.3$ disk. . . . . . . . . . . 138

5.3 Instability growth for a $q = 1$ disk on a 129×129 grid. . . . . . . . . . 140

5.4 Perturbed disk morphology for a $q = 1$ model at $t = 1.1 \times 10^{13}s$. . . . 141

5.5 Instability growth for a $q = 0.3$ disk on a 129×129 grid. . . . . . . . . 142

5.6 Perturbed disk morphology for a $q = 0.3$ model at $t = 1.1 \times 10^{13}s$. . . 144

5.7 Radial density and temperature distributions for an unperturbed $q = 1$ disk at $5 \times 10^{12} s$. . . . . . . . . . . . . . . . . . . . . . . . . . . . . 145

5.8 Instability growth for a $q = 1$ disk perturbed at $5 \times 10^{12} s$. . . . . . . 146

5.9 Morphology of a $q = 1$ disk at $1.1 \times 10^{13} s$. . . . . . . . . . . . . . . . 147

5.10 Evolution of an unperturbed $q = 1$ disk when gravity is activated at $5 \times 10^{12} s$. . . . . . . . . . . . . . . . . . . . . . . . . . . . . . . . 149

5.11 Radial density and temperature distributions for an unperturbed, self-gravitating $q = 1$ disk at $1.1 \times 10^{13} s$. . . . . . . . . . . . . . . . . . . . 150

5.12 Instability growth for a self-gravitating $q = 1$ disk perturbed at $5 \times 10^{12} s$. . . . . . . . . . . . . . . . . . . . . . . . . . . . . . . . 151

5.13 Morphology of a self-gravitating $q = 1$ disk at $1.1 \times 10^{13} s$. . . . . . . 152

5.14 Maximum density along the symmetry axis versus time for models with a free outer boundary. . . . . . . . . . . . . . . . . . . . . . . . . 153

5.15 Total mass versus time for models with $v_i = 5\, km\, s^{-1}$. . . . . . . . . . 155

5.16 Onset of instability in an unperturbed $q = 1$ disk with reflective outer boundary. . . . . . . . . . . . . . . . . . . . . . . . . . . . . . . . . 157

5.17 Radial density and temperature distributions for an unperturbed $q = 1$ disk with a reflective outer boundary at $5 \times 10^{12} s$. . . . . . . . . . . . 158

5.18 Instability growth for a $q = 1$ disk with a reflective outer boundary perturbed at $5 \times 10^{12} s$. . . . . . . . . . . . . . . . . . . . . . . . . . . 159

5.19 Morphology of a $q = 1$ disk with a reflective outer boundary at $1.1 \times 10^{13} s$. . . . . . . . . . . . . . . . . . . . . . . . . . . . . . . 160

5.20 Evolution of an unperturbed $q = 1$ disk with a reflective outer boundary when gravity is activated at $5 \times 10^{12} s$. . . . . . . . . . . . . 161

5.21 Instability growth for a self-gravitating $q = 1$ disk with a reflective outer boundary perturbed at $5 \times 10^{12} s$. . . . . . . . . . . . . . . . . . 162

5.22 Morphology of a self-gravitating $q = 1$ disk with a reflective outer boundary at $1.1 \times 10^{13} s$. . . . . . . . . . . . . . . . . . . . . . . . . . 163

5.23 Maximum density along the symmetry axis for models with a reflective outer boundary. . . . . . . . . . . . . . . . . . . . . . . . . . . . . . 164

5.24 Instability growth for a $q = 0.3$ disk perturbed at $5 \times 10^{12} s$. . . . . . 166

5.25 Morphology of a $q = 0.3$ disk at $1.1 \times 10^{13} s$. . . . . . . . . . . . . . . 167

5.26 Instability growth for a self-gravitating $q = 0.3$ disk perturbed at $5 \times 10^{12} s$. . . . . 168

5.27 Morphology of a self-gravitating $q = 0.3$ disk at $1.1 \times 10^{13} s$. . . . . . 169

5.28 Instability growth for a model with $T_{min} = 3\,K$. . . . . . . . . . . . . 171

5.29 Morphology of a perturbed disk with $T_{min} = 3\,K$ at $1.1 \times 10^{13} s$. . . . 172

5.30 Instability growth for a model with $T_{min} = 10\,K$. . . . . . . . . . . . 173

5.31 Morphology of a perturbed disk with $T_{min} = 10\,K$ at $1.1 \times 10^{13} s$. . . 174

5.32 Maximum density along the symmetry axis versus time for perturbed models with varying $T_{min}$. . . . . . . . . . . . 175

5.33 Total mass versus time for perturbed models with varying $T_{min}$. . . . 176

5.34 Onset of instability in an unperturbed disk with $v_i = 7.5\,km\,s^{-1}$. . . . 178

5.35 Evolution of a disk with $v_i = 7.5\,km\,s^{-1}$ perturbed at $3 \times 10^{12} s$. . . . 179

5.36 Morphology of a perturbed disk with $v_i = 7.5\,km\,s^{-1}$ at $7.0 \times 10^{12} s$. . 180

5.37 Evolution of an unperturbed disk with $v_i = 7.5\,km\,s^{-1}$ when gravity is activated at $3 \times 10^{12} s$. . . . . . . . . . . . 182

5.38 Evolution of a self-gravitating disk with $v_i = 7.5\,km\,s^{-1}$ perturbed at $3 \times 10^{12} s$. . . . . . . . . . . . 183

5.39 Morphology of a self-gravitating, perturbed disk with $v_i = 7.5\,km\,s^{-1}$ at $7.0 \times 10^{12} s$. . . . . . . . . . . . 184

5.40 Maximum density along the symmetry axis versus time for models with $v_i = 7.5\,km\,s^{-1}$. . . . . . . . . . . . 185

5.41 Total mass versus time for models with $v_i = 7.5\,km\,s^{-1}$. . . . . . . . . 186

Abstract of Dissertation Presented to the Graduate School
of the University of Florida in Partial Fulfillment of the
Requirements for the Degree of Doctor of Philosophy

# A COMPUTATIONAL STUDY OF INTERFACIAL INSTABILITIES IN THE INTERSTELLAR MEDIUM

By

Robert M. Hueckstaedt

August 2001

Chairman: Dr. James H. Hunter Jr.
Major Department: Astronomy

One of the most important problems in astronomy today is the development of a comprehensive theory for the origins of stars and planetary systems. In order to understand star formation, we must understand the interstellar medium (ISM) in which the process occurs. The evolution of the ISM is driven by a variety of phenomena, including gravity, turbulence, shearing flows, magnetic fields, and the thermal properties of the gas. As a result, the ISM is susceptible to a wide range of hydrodynamic instabilities. In this dissertation, two very different types of instabilities are studied using computational hydrodynamics simulations. The first is a recently discovered instability which acts upon an interface of discontinuous density. Theory predicts that this self-gravity driven interfacial instability persists in the static limit and in the absence of a constant background acceleration. Disturbances to a density interface are found to grow on a time-scale of the order of the free-fall time, even when the perturbation wavelength is much less than the Jeans length. Here, I present the first numerical simulations of this instability. The theoretical growth rate is confirmed and the nonlinear morphology displayed. The self-gravity interfacial instability is shown to be fundamentally different from the Rayleigh-Taylor instability, although both exhibit similar morphologies under the condition of a high density contrast such as is commonly found in the ISM. Such instabilities are a possible mechanism by which observed features, such as the pillars of gas seen near the boundaries of interstellar clouds, are formed.

The second instability considered in this study is a dynamic instability which occurs when supersonic gas streams collide. It is driven by a combination of ram pressure and strong cooling. I examine the stability of a cold, dense slab formed by the head-on collision of supersonic gas streams. Special emphasis is placed on the effects of altering the cooling rate. A series of models are performed in cylindrical geometry to determine whether the instability of the slab acts to increase or decrease the likelihood of forming collapsing regions capable of undergoing star formation.

# CHAPTER 1
# INTRODUCTION

One of the most important problems in astronomy today is the development of a comprehensive theory for the origins of stars and planetary systems. This is a problem of great complexity that involves changes over many orders of magnitude in size, density, and temperature. Advances in observational and computational tools are fueling progress, but many questions remain unanswered. In order to understand star formation, we must understand the environment in which the process occurs-molecular clouds. The morphology and evolution of molecular clouds are driven by a variety of physical phenomena, some of which aid the star forming process while others oppose it. This dissertation describes a theoretical study that uses computational techniques to investigate hydrodynamic instabilities which may trigger the formation of self-gravitating regions conducive to star formation. In this chapter, I summarize current theories of molecular cloud morphology and star formation. I also give a brief history detailing the use of numerical simulations to study hydrodynamic flows in the interstellar medium (ISM). The hydrodynamic instabilities that are the focus of this dissertation are introduced. This chapter concludes with an outline for the remainder of the dissertation.

## 1.1 Molecular Clouds and Star Formation

Because all present day star formation is observed to take place inside giant molecular clouds (GMCs), knowing how molecular clouds form and evolve is crucial for understanding the initial conditions for star formation. Observational work using radio and infrared telescopes has produced a wealth of information about GMCs. A typical GMC is gravitationally bound, magnetized, and compressible. GMCs in the solar neighborhood are observed to have masses of $10^{5-6}\,M_\odot$ and a mean diameter of 45 $pc$ (Blitz 1993). Molecular clouds are observed to be clumpy. The clumps vary in geometry from spherical to highly filamentary. Molecular linewidths are wider than thermal linewidths inferred from excitation temperatures, indicating a turbulent medium. The observed structures of molecular clouds are self-similar on different length scales and obey power-law scaling relations (Larson 1981). The relations among the internal velocity dispersion $\Delta v$, mean gas particle density $n$, cloud radius $R$, and cloud mass $M$ are (from Falgarone and Puget 1986)

$$\left(\frac{\Delta v}{0.36\,km\,s^{-1}}\right)^4 \simeq \left(\frac{n}{570\,cm^{-3}}\right)^{-2} \simeq \left(\frac{R}{pc}\right)^2 \simeq \left(\frac{M}{100\,M_\odot}\right) . \tag{1.1}$$

Recent evidence reveals that the self-similarity does not extend to small ($\lesssim 0.2\,pc$) scales (Williams 1999), indicating that once a core begins to collapse due to self-gravity it takes on characteristics very different from the parent cloud.

Over the last century, star formation has been the subject of extensive scientific study. According to the classic theory of Jeans (1929), a static, homogeneous, spherical cloud will collapse if its mass exceeds a critical value, $M_J$, given by

$$M_J = \frac{1}{6}\pi\rho\left(\frac{\pi c^2}{G\rho}\right)^{\frac{3}{2}} . \tag{1.2}$$

In the above, $\rho$ is the gas volume density, $c$ the sound speed, and $G$ the gravitational constant. The time scale for collapse is the free-fall time, $t_{ff} = (3\pi/32G\rho)^{(1/2)}$. For densities typical of molecular clouds, a free-fall time of $t_{ff} \sim 10^6\,yr$ is expected. Although no current star formation is observed outside of molecular clouds, there are clouds in which no star formation is observed. This presents two possibilities: either there are some clouds in which conditions are intrinsically unsuitable for star formation, or there are clouds in which star formation has not yet begun. This second possibility implies that molecular clouds have lifetimes that exceed the time needed for star formation. If clouds are to have lifetimes longer than their free-fall times, some means of support against gravitational collapse is needed. One possible support mechanism is provided by magnetic fields. Magnetic field strengths in molecular clouds, determined by measuring the Zeeman effect, show a range from 10 – 3100 $\mu G$ (e.g. Crutcher 1999). Magnetic fields can support a cloud provided the cloud mass does not exceed a critical value, $M_{crit}$, such that (Lada and Shu 1990)

$$M_{crit} \approx 10^5 M_\odot \left(\frac{B}{30\,\mu G}\right)\left(\frac{R}{20\,pc}\right)^2 . \tag{1.3}$$

According to the popular bimodal theory of star formation, this critical mass divides two regimes of star formation. Clouds that exceed the critical mass are called supercritical, and clouds with a mass below the critical mass are called subcritical. In a supercritical cloud, magnetic support can not prevent collapse. The cloud will contract and fragment into smaller clouds that may or may not be supported by magnetic fields themselves. For cases in which the magnetic field strength is low, a large cloud that contracts and fragments may ultimately form a cluster of stars. If little or no fragmentation occurs, the process produces high mass stars. In subcritical clouds, magnetic fields slow the collapse. Ions are coupled to the lines, but neutral molecular gas is free to diffuse across magnetic field lines. When neutral molecules attempt to cross a field line due to gravitational contraction, their motion is retarded by collisional interaction with the ions. This process of ambipolar diffusion slows the cloud contraction so that the time needed for collapse is increased by an order of magnitude. The typical end result of a subcritical cloud undergoing ambipolar diffusion is an isolated, low mass star.

In the bimodal model, the magnetic field strength is the determining factor between isolated and clustered star formation. However, observational studies have failed to identify any magnetically subcritical clouds (Crutcher 1999). Furthermore, observations indicate that typically only a few percent of a cloud's mass is converted into stars (Leisawitz et al. 1989). Mechanisms are needed that can lend global support to a cloud while facilitating regions of local collapse within the cloud. The dynamic nature of the ISM must be considered. The free-fall time for gravitational collapse is greatly modified if the initial state of the gas is not static. Convergent supersonic velocity fields can reduce the mass needed for collapse to a value below the classical Jeans mass (Hunter 1979, Hunter and Fleck 1982). Recently, Klessen et al. (2000) performed simulations which demonstrate that random, supersonic motions can support a cloud against global collapse, while colliding streams within the cloud give rise to regions unstable to local collapse. Thus, star formation can occur on small scales within a cloud even though the cloud is supported against global collapse. A new model for the ISM has emerged that further emphasizes the role of turbulence. This theory holds that clouds are density enhancements created by the interaction of larger scale turbulent flows (Elmegreen 1993b, Fleck 1996, Ballesteros-Paredes et al. 1999a). The self-similar nature of clouds is then explained. Convergent flows within a cloud give rise to density enhancements that appear to form smaller, denser clouds. Ballesteros-Paredes et al. (1999b) speculate that clouds and stars may form on time-scales far shorter than anticipated by quasi-static theories. They suggest that the Taurus molecular cloud formed and evolved into a star forming region in less than three million years.

## 1.2 Hydrodynamic Simulations of the ISM

The role of turbulence and hydrodynamic instabilities in shaping the ISM has been investigated for the last half century. In one early work, von Weizsäcker (1951) considered the evolution of stars and galaxies in a turbulent and compressible medium. Chandrasekhar and Münch (1952) studied the ISM as a "fluctuating continuous distribution of matter". In both of these visionary works, the authors abandoned the idea that the ISM can be characterized by discrete clouds. They recognized the importance of dynamical forces in the ISM.

Due to its highly nonlinear nature, turbulence cannot be modeled analytically. Further complications arise for astrophysical systems. Unlike terrestrial laboratory turbulence, interstellar turbulence is highly supersonic, magnetized, self-gravitating, and contains embedded sources (Elmegreen 1993a). And whereas terrestrial turbulence is driven by the injection of energy only on large scales, energy is injected into interstellar turbulence on many scales. Galactic shear and superbubbles induce turbulent motions on large scales ($\geq 1\,kpc$). Mechanisms which operate at moderate scales ($\geq 100\,pc$) include supernovae and expanding H II regions. On small scales within molecular clouds ($< 10\,pc$), stellar winds and protostellar outflows impart kinetic energy to the surrounding environment. Numerical modeling is needed to investigate the complex forces at work. Advances in computing power have led to an explosion in the number of simulations of the ISM. (A recent review is given by Vázquez-Semadeni et al. 2000.) The first simulations of colliding clouds (Stone 1970a, 1970b) required a high degree of symmetry. Far more complicated simulations are now possible. Although the formation of a comprehensive model for the ISM is still infeasible today, the range of physical processes under consideration is expanding. Researchers now recognize the importance of thermodynamic processes in the ISM. For instance, approximating the ISM as an isothermal gas is inappropriate in most situations (e.g. Hunter et al. 1986, Tohline et al. 1987, Vázquez-Semadeni et al. 1996). The development of magnetohydrodynamics codes has allowed the inclusion of magnetic fields and plasma flows. As computational simulations continue to advance, astronomers must remember to carefully consider the physical processes driving the dynamics and evolution of the ISM. Fully understanding the physics of the ISM requires careful isolation and study of each process in turn. Only then can processes be coupled together in efforts to form models which are more in line with the observational picture of the ISM.

The ISM is susceptible to a wide range of hydrodynamic instabilities. Instabilities fall largely into two categories, global and interfacial. Global instabilities act throughout an entire volume of gas. Examples include the Jeans instability (Jeans

1929), thermal instability (Weymann 1960, Field 1965), and Parker instability (Parker 1966). Interfacial instabilities act locally at an interface. Examples include the Rayleigh-Taylor instability, Kelvin-Helmholtz instability, and thermal-dynamic instability (Hunter and Whitaker 1989). The effort to understand how instabilities develop is complicated when conditions give rise to multiple instabilities at the same time. Recreating astrophysical conditions on Earth is very difficult at best. Numerical simulations are the best tools for isolating and studying instabilities. Extensive numerical studies have been performed to examine the Rayleigh-Taylor instability (e.g. Youngs 1984, Jun et al. 1995) and the Kelvin-Helmholtz instability (e.g. Murray et al. 1993, Frank et al. 1996, Vietri et al. 1997). However, some instabilities have not received a great deal of attention. Two such instabilities provide the focus for this dissertation. The first is a recently discovered (Hunter et al. 1997) instability which acts across an interface of discontinuous density and is driven solely by self-gravity. The second is a dynamic instability which occurs when supersonic gas streams collide. This instability is driven by ram pressure and strong cooling (Hunter et al. 1986, Stevens et al. 1992). At issue is whether interacting streams give rise to collapsing regions. If so, then one epoch of star formation may trigger the subsequent birth of additional stars (Elmegreen and Lada 1977). Both instabilities are described in great detail in later chapters.

## 1.3 Thesis Structure

This dissertation is divided into six chapters. The first is this introductory chapter. In chapter 2, I describe the numerical methods. In chapter 3, I present the first computational study to focus on interfacial instabilities driven by self gravity. Chapters 4 and 5 are devoted to the study of colliding gas streams and the instabilities that develop. In chapter 4, I concentrate on models in Cartesian geometry in which the role of molecular cooling is emphasized. In chapter 4, I discuss cylindrical models with a focus on the formation of collapsing clumps. I conclude this work in chapter 6 with a summary of the results and some remarks about future considerations.

# CHAPTER 2
# COMPUTATIONAL TECHNIQUES

The study of nonlinear phenomena requires the use of numerical modeling. For problems concerning hydrodynamic instabilities in the ISM, the equations governing the flow of gas are discretized and solved on a computer. The computer code advances the hydrodynamic state of the gas in time. The code used for this study is the Computational Fluid Dynamics LIBrary (CFDLIB) created at the Los Alamos National Laboratory (LANL). In order to model the environment of interstellar space, specialized subroutines are needed to simulate cooling processes and self-gravitational forces. These routines were written and implemented to run within the structure of CFDLIB. Figure 2.1 shows the main subroutines as called by CFDLIB along with a brief description of each. An input file is used to specify the computational parameters, grid parameters, and initial values for the state variables. CFDLIB generates a grid and begins the computational cycle. Each cycle consists of several distinct phases. Subsequent sections of this chapter describe the hydrodynamic, self-gravity, and cooling portions of the code.

## 2.1 The Hydrodynamic Code

Hydrodynamic calculations are performed using CFDLIB, a package of FORTRAN codes from LANL capable of solving a wide range of computational fluid dynamics problems. CFDLIB is well suited for handling flows of any speed, from low velocity, incompressible flows to high velocity, compressible flows. The programs within CFDLIB are connected by a common data structure and numerical method, which allows for easy modifications and additions to the code library. CFDLIB uses

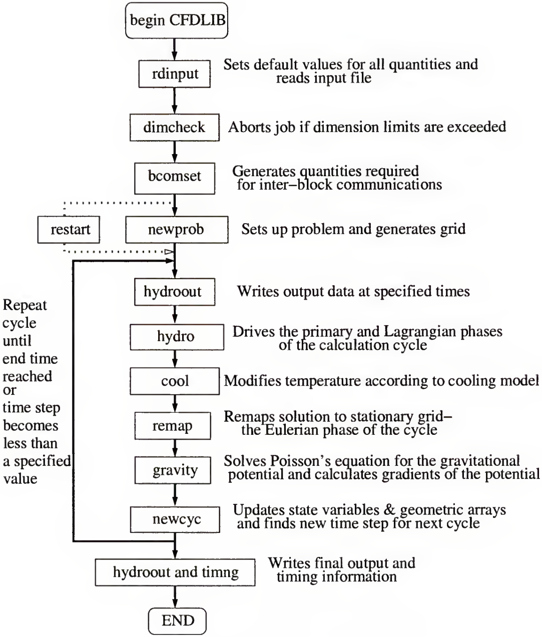
begin CFDLIB
rdinput
Sets default values for all quantities and reads input file
dimcheck
Aborts job if dimension limits are exceeded
bcomset
Generates quantities required for inter–block communications
restart
newprob
Sets up problem and generates grid
hydroout
Writes output data at specified times
Repeat cycle until end time reached or time step becomes less than a specified value
hydro
Drives the primary and Lagrangian phases of the calculation cycle
cool
Modifies temperature according to cooling model
remap
Remaps solution to stationary grid– the Eulerian phase of the cycle
gravity
Solves Poisson's equation for the gravitational potential and calculates gradients of the potential
newcyc
Updates state variables & geometric arrays and finds new time step for next cycle
hydroout and timng
Writes final output and timing information
END

Figure 2.1: Chart of subroutines called by CFDLIB main program.

Finite-Volume computational schemes on structured grids in which all state variables are cell-centered. In Finite-Volume methods, the integral form of the conservation equations are solved over a grid in which each cell is treated as a control volume (Kashiwa et al. 1994). Fluid flow is modeled by tracking the fluxes of material, momentum, and energy between adjacent cells. Features of CFDLIB allow the user to choose boundary conditions, geometry, an equation of state, and whether to include magnetic fields in the calculation. Calculations may be done in two dimensions or in three dimensions, although run parameters are more limited in three dimensions. Also, CFDLIB is capable of performing multi-fluid calculations. One of the advantages of CFDLIB over other codes is the incorporation of the full viscous stress tensor into the equations of hydrodynamics. Other codes rely on an artificial viscosity term to represent distortions of the scalar pressure. The full tensor gives a more realistic solution, especially in shocked regions.

The underlying method used by CFDLIB is called split Arbitrary-Lagrangian-Eulerian (ALE). This method allows the grid to move in an arbitrary way. The user may choose to use an Eulerian mesh of spatially fixed grid points, a Lagrangian mesh that moves with the fluid, or a combination of the two. Regardless of the choice, each computational cycle is split into three phases. In the primary phase, the equation of state is used to solve for the pressure, and auxiliary variables that are not explicitly time dependent are calculated. Next, the effects of the physical processes are computed in the Lagrangian phase. Lastly, in the Eulerian phase, the state variables are advected and mapped to a common control volume. CFDLIB combines the ALE method with a semi-implicit scheme known as ICE (Implicit Continuous-fluid Eulerian). The ICE scheme is semi-implicit in that the implicitness is restricted to the Lagrangian phase of the calculation. The ALE method was developed for modeling compressible fluids, but the addition of the ICE technique allows the code to work for any flow speed (Hirt et al. 1974). In other words, CFDLIB is stable for any value of the Courant number based on the sound speed. Following the description of Addessio et al. (1992), I present here the basic ideas of the finite volume method at the heart of CFDLIB. Throughout this chapter, vector quantities are denoted by boldface characters.

Neglecting magnetic fields, the equations of fluid dynamics which describe the conservation of mass, momentum, and energy can be expressed in the familiar differential form

$$\frac{\partial \rho}{\partial t} + \nabla \cdot (\rho \mathbf{u}) = 0, \tag{2.1}$$

$$\frac{\partial \rho \mathbf{u}}{\partial t} + \nabla \cdot (\rho \mathbf{u}\mathbf{u}) = -\nabla p + \nabla \cdot \mathbf{\Pi} + \rho \mathbf{F}, \tag{2.2}$$

$$\frac{\partial \rho E}{\partial t} + \nabla \cdot (\rho E \mathbf{u}) = -\nabla \cdot p\mathbf{u} + \nabla \cdot \mathbf{\Pi} \cdot \mathbf{u} + \rho \mathbf{F} \cdot \mathbf{u} - \nabla \cdot \mathbf{h} + Q. \tag{2.3}$$

In these equations, $\rho$ is the mass density, $\mathbf{u}$ the fluid velocity, and $p$ the fluid pressure. The total energy per unit mass $E$ is given by $E = e + (1/2)\mathbf{u}\cdot\mathbf{u}$, where $e$ is the internal energy per unit mass. The pressure is determined from $\rho$ and $E$ via the equation of state. The stress tensor, $\mathbf{\Pi}$, describes any viscosity or turbulence. For some problems, additional physics may be needed as described by a body force per unit mass $\mathbf{F}$, a heat-flux vector $\mathbf{h}$, or an energy release rate per unit volume $Q$. Gravitational forces are included in $\mathbf{F}$. Equation (2.2) is known as the Navier-Stokes equation for viscous flows. In the Finite-Volume method, the integral form of the equations is used. The integral form expresses the idea that a conserved quantity (mass, momentum, or energy) may only change within a particular control volume by an amount equal to the net flux of that quantity across the bounding surface of the control volume. The values within a cell are updated by keeping track of the amount of material, momentum, and energy entering and leaving the cell. When expressed in integral form, the equations are

$$\frac{d}{dt} \int_{V_m(t)} \rho dV + \int_{S_m(t)} \rho(\mathbf{u} - \mathbf{u}_m) \cdot \mathbf{n} dS = 0, \tag{2.4}$$

$$\frac{d}{dt}\int_{V_m(t)} \rho\mathbf{u}dV + \int_{S_m(t)} \rho\mathbf{u}(\mathbf{u}-\mathbf{u}_m)\cdot\mathbf{n}dS = -\int_{S_m(t)} p\mathbf{n}dS + \int_{S_m(t)} \mathbf{n}\cdot\mathbf{\Pi}dS + \int_{V_m(t)} \rho\mathbf{F}dV, \tag{2.5}$$

$$\frac{d}{dt}\int_{V_m(t)} \rho EdV + \int_{S_m(t)} \rho E(\mathbf{u}-\mathbf{u}_m)\cdot\mathbf{n}dS = -\int_{S_m(t)} p\mathbf{u}\cdot\mathbf{n}dS + \int_{S_m(t)} \mathbf{n}\cdot\mathbf{\Pi}\cdot\mathbf{u}dS - \int_{S_m(t)} \mathbf{h}\cdot\mathbf{n}dS + \int_{V_m(t)} \rho\mathbf{F}\cdot\mathbf{u}dV \int_{V_m(t)} QdV. \tag{2.6}$$

Each cell acts as a control volume $V_m(t)$ with a surface of $S_m(t)$ and outward unit normal $\mathbf{n}$. The control volume moves with velocity $\mathbf{u}_m$. The volume in each cell is conserved, so that

$$\frac{dV_m(t)}{dt} = \int_{S_m(t)} \mathbf{u}_m\mathbf{n}dS. \tag{2.7}$$

In the Lagrangian limit, the control volume moves at the same velocity as the fluid so $\mathbf{u}-\mathbf{u}_m = 0$. This simplifies the equations. For example, the equation of continuity, equation (2.4), becomes

$$\frac{d}{dt}\int_{V_L} \rho dV = 0. \tag{2.8}$$

The Lagrangian control volume is designated $V_L$. The ICE-ALE method takes advantage of the simplified equations by updating the variables in the Lagrangian limit and then remapping the solution onto the control grid.

CFDLIB implements the ICE-ALE method in a way that is modified from the original algorithm of Hirt et. al (1974). The use of the Lagrangian and Eulerian phases remains the same, but a new primary phase of the calculation is added to improve the efficiency of the code and generalize the code for multiphase flows. Following Kashiwa et al. (1994), I summarize the CFDLIB implementation of the ICE-ALE method beginning with the Eulerian phase and proceeding backwards to the primary phase. This way the motivation for the primary phase shall be made clear. The main variables in CFDLIB are the mass density $\rho$, the velocity $\mathbf{u}$, and the temperature $T$. The choices of velocity over momentum and temperature over energy help to avoid generating numerical noise. The code need not divide by the total mass to define the velocity nor convert from total energy to temperature. It is especially important to resolve the temperature as accurately as possible for problems with chemical reactions. In an ideal, polytropic gas, the temperature and specific internal energy are related simply as $e = c_v T$, with $c_v$ defining the specific heat at constant volume. The equation of state relates the temperature, density, and pressure so that any two can be used to determine the third. For an ideal gas, the equation of state is

$$p = \frac{\gamma R}{\mu} \rho T, \tag{2.9}$$

where $\gamma$ is the ratio of specific heats, $\mu$ the molecular weight, and $R$ the gas constant, ($R{=}8.314{\times}10^7\, ergs\, K^{-1}\, mol^{-1}$). Both the ideal gas law and the polytropic relation, $p \propto \rho^\gamma$, are used throughout this study.

Although CFDLIB has been generalized to handle multiple species of fluid, I describe the single fluid version to simplify the notation. The variable $q$ is used to represent any state variable. In this description, $q$ is considered the average value within a control volume V so that $\int_V q dV = qV$. The advection equation that relates the total change in $q$ on a computational mesh moving at $\mathbf{u}_m$ to the change in $q$ due to the physical processes within V is

$$\frac{d}{dt}(qV) + \int \mathbf{n} \cdot q(\mathbf{u} - \mathbf{u}_m) dS = \frac{\Delta(qV)}{\Delta t}. \tag{2.10}$$

The right hand side represents the change due to physical processes, which is the solution from the Lagrangian phase of the calculation. Using superscripts to denote the time step, equation (2.10) is discretized and written

$$q^{n+1} V^{n+1} - q^n V^n + \Delta t A(q) = q^L V^L - q^n V^n. \tag{2.11}$$

The $q^n V^n$ terms cancel leaving a relationship between the updated value on the mesh and the Lagrangian value. The advection operator $\Delta t A(q)$ is defined as

$$\Delta t A(q) = \sum_i \Delta t \mathbf{S}_i \cdot (\mathbf{u}^* - \mathbf{u}_m)_i \langle\langle q \rangle\rangle_i^u . \tag{2.12}$$

The sum is taken over all surfaces defining $V^n$, with $\mathbf{S}_i$ representing the area times outward normal of each side. The face-centered fluxing velocity $\mathbf{u}^*$ is one of the main results of the primary phase. The bracketed term is an upwind-centered value of $q$, expanded in a spatial Taylor series to a point just upstream of $i$. The Taylor series is second-order in space and uses gradients that are limited using the method of van Leer (1977). The Lagrangian volume $V^L$ and the new mesh volume $V^{n+1}$ are both updated to reflect changes to the velocity fields,

$$V^L = V^n + \Delta t \sum_i (\mathbf{S} \cdot \mathbf{u}^*)_i \tag{2.13}$$

$$V^{n+1} = V^n + \Delta t \sum_i (\mathbf{S} \cdot \mathbf{u_m})_i \tag{2.14}$$

The updated volumes are used along with equation (2.11) to arrive at the final equations for the updated state variables,

$$\rho^{n+1} = [\rho^L V^L - \Delta t A(\rho^n)]/V^{n+1} \tag{2.15}$$

$$\mathbf{u}^{n+1} = [\mathbf{u}^L V^L - \Delta t A(\mathbf{u}^n)]/V^{n+1} \tag{2.16}$$

$$T^{n+1} = [T^L V^L - \Delta t A(T^n)]/V^{n+1}. \tag{2.17}$$

The values of $\rho^L$, $\mathbf{u}^L$, and $T^L$ are determined in the Lagrangian phase.

In the Lagrangian phase, the effects of the physical processes are calculated. The Lagrangian values for density, velocity, and temperature are determined in a manner similar to that of equations (2.15-2.17), namely

$$\rho^L = [\rho^n V^n + \Delta m]/V^L \tag{2.18}$$

$$\mathbf{u}^L = \mathbf{u}^n[1 - (\Delta m/m^L] + (\Delta m \mathbf{u})/m^L \tag{2.19}$$

$$T^L = T^n[1 - (e^n/c_v T^n)(\Delta m)/m^L] + (\Delta m e)/m^L. \tag{2.20}$$

The value of $\Delta m$ reflects the exchange of mass between different species of fluid. For the case of a single fluid, the $\Delta m$ term vanishes, leaving a simplified set of equations,

$$\rho^L = \rho^n V^n / V^L \tag{2.21}$$

$$\mathbf{u}^L = \mathbf{u}^n + (\Delta m \mathbf{u})/m^L \tag{2.22}$$

$$T^L = T^n + (\Delta m e)/m^L. \tag{2.23}$$

For the remainder of this section, I adopt the notation of Kashiwa et al. (1994) and use $V^n \nabla^c$ to denote the discrete form of a cell-centered integral over the sides of a computational cell which acts on face-centered quantities. The $\Delta m\mathbf{u}$ and $\Delta me$ terms contain the physics for the problem,

$$(\Delta m \mathbf{u})/m^L = (\mathbf{F}/m)\Delta t - (\rho^{-1}\Delta t V^n \nabla^c p^*)/V^L + (\Delta t V^n \nabla^c \cdot \boldsymbol{\tau})/m^L, \tag{2.24}$$

$$(\Delta m e)/m^L = (\rho c)^{-2}(p^n \Delta p)/V^L. \tag{2.25}$$

The quantity $c$ is the sound speed ($c^2 = \gamma P/\rho$). These equations do not include turbulence and are valid only for single-phase fluids. The momentum equation, equation (2.24), contains the momentum change due to body forces, pressure forces, and forces from stress. Gravitational forces are included in the body force term $\mathbf{F}$, and $\boldsymbol{\tau}$ represents the stress. The energy equation, equation (2.25), looks deceptively simple. However, the expression for $\Delta p$ is rather complicated. The quantities $p^*$ and $\Delta p$ are determined in the primary phase.

The primary phase of the calculation is responsible for calculating quantities which are not explicit functions of time. The equation of state, equation (2.9) for an ideal gas, is evaluated to find the pressure. Also calculated in the primary phase are the auxiliary quantities used in the Lagrangian and Eulerian phases. The required quantities are the face-centered fluxing velocity $\mathbf{u}^*$ (used in equations 2.12

and 2.13), the face-centered equilibration pressure $p^*$ (used in equation 2.24), and the cell-centered change in the equilibration pressure $\Delta p$ (used in equation 2.25). For ease of notation, let $\nabla^f$ represent a face-centered gradient operating on surrounding cell-centered data. Also, let $v$ represent the specific volume (volume per unit mass). In models involving multiple fluids, the value of $v$ must be tracked for each individual fluid. In the single fluid case, $v$ is simply the reciprocal of the density, $v = \rho^{-1}$. For further convenience, the quantity $v^f$ is defined as $v^f = 1/(\rho_l + \rho_r)$, with the subscripts $l$ and $r$ denoting the values in the cell to the left or right of the cell face being considered.

The equilibration pressure is defined for multiple fluids as the pressure that enables specified masses of separated materials to fill an entire volume with no ongoing compression or expansion. In the single fluid limit, the equilibration pressure is simply the pressure at a cell face, as opposed to the cell-centered pressure calculated from the equation of state. The change in the equilibration pressure is determined from

$$[V^n(v/c^2) - \Delta t^2 V^n \nabla^c \cdot v^f \nabla^f]\Delta p = -\Delta t V^n \nabla^c \cdot \tilde{\mathbf{u}}, \tag{2.26}$$

where

$$\tilde{\mathbf{u}} = \left(\frac{\rho_l \mathbf{u}_l + \rho_r \mathbf{u}_r}{\rho_l + \rho_r}\right) - v^f \Delta t \nabla^f p^n + \mathbf{g}\Delta t/2. \tag{2.27}$$

The vector $\mathbf{g}$ represents the acceleration due to all body forces, not just gravity. Finding $\Delta p$ means solving a linear system of equations that involves every computational cell. Once this has been done, the fluxing velocity is defined as

$$\mathbf{u}^* = \left(\frac{\rho_l \mathbf{u}_l + \rho_r \mathbf{u}_r}{\rho_l + \rho_r}\right) - v^f \Delta t \nabla^f p^L + \mathbf{g}\Delta t/2. \tag{2.28}$$

Notice that the equation for the fluxing velocity is the same as equation (2.27) except that $p^n$ has been replaced by $p^L = p^n + \Delta p$. This is one of the major factors in the stability of the ICE method. Linear stability is assured when $p^L$ is used in the equation for the pressure because $p^L$ provides a good estimate of the advanced-time pressure. The equilibration pressure $p^*$ used in the equation of motion is given by

$$p^* = \left(\frac{v_r p_r^L + v_l p_l^L}{v_r + v_l}\right) + \phi \frac{\Delta x}{\Delta t} \langle \frac{uv}{c^2} \rangle \frac{(\Delta p_r^L - \Delta p_l^L)}{v_r + v_l} + \phi \frac{[u_r(u_r - u^*) - u_l(u^* - u_l)]}{v_r + v_l}. \quad (2.29)$$

A flux limiter $\phi$ is applied to the second two terms in order to minimize diffusion. The idea is to limit any non-physical spatial distribution in the velocity field that arises out of numerical noise. The limiter has a value between zero and one, with the value tending towards zero when the velocity field is smooth.

The overall algorithm of the ICE-ALE algorithm as implemented by CFDLIB begins by calculating the equation of state and auxiliary variables in the primary phase. Next, the physical processes are computed in the Lagrangian phase. Finally, the solution is advected onto the control mesh in the Eulerian phase. If the user chooses to run the code as purely Lagrangian, the Eulerian step is unnecessary. The time interval between cycles is limited by the Courant timestep as determined from the greater of the flow speed or the sound speed. Examples of model runs done with CFDLIB are given by Kashiwa et al. (1994). What follows is an example of a purely hydrodynamic model done with CFDLIB that is applicable to astrophysical scales.

When a fluid is placed on top of a more tenuous fluid in a gravitational field (such that the denser fluid is accelerated into the tenuous fluid), the interface exists in an unstable equilibrium. If the interface is disturbed, the denser fluid will displace the lighter fluid, ultimately resulting in the inversion of the original configuration. The name given to this phenomenon is the Rayleigh-Taylor (RT) instability. For an incompressible gas, the linear growth of an RT instability is well documented (e.g. Chandrasekhar 1961). For a perturbation proportional to $e^{-i(wt-kx)}$, the growth rate is given by

$$\omega^2 = \left(\frac{\rho_2 - \rho_1}{\rho_2 + \rho_1}\right) \mathbf{g} \cdot \mathbf{k}, \quad (2.30)$$

where $\omega$ is the growth rate, $k$ the horizontal wavenumber, and $\mathbf{g}$ the gravitational acceleration in the vertical direction. Figure (2.2) shows the configuration of the RT

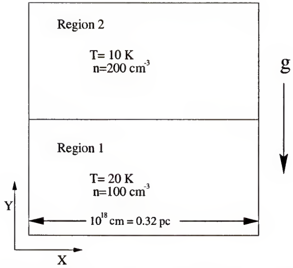

Figure 2.2: Configuration of the Rayleigh-Taylor simulation.

test problem. The simulation is performed on an 80×80 Cartesian grid with a fixed cell size of $\Delta x = \Delta y = 1.25 \times 10^{16}\, cm$. The grid is constrained by reflective boundary conditions on all four sides. The grid is treated as though filled with molecular hydrogen gas with molecular weight $\mu = 2.0$ and a ratio of specific heats $\gamma = 1.4$. The number density and temperature below the interface are $n_1 = 100\, cm^{-3}$ and $T_1 = 20\, K$, respectively. The number density and temperature above the interface are $n_2 = 200\, cm^{-3}$ and $T_2 = 10\, K$, respectively. The pressure is continuous at the interface. The temperature remains constant throughout each region, but the density falls off as

$$n(y)_{1,2} = n(0)_{1,2} e^{-\frac{|y-y(0)|}{H_{1,2}}}, \tag{2.31}$$

where $y(0) = 5.0 \times 10^{17}\, cm$ is the position of the interface. The gravitational scale height is

$$H = \frac{k_B T}{\mu m_H g}, \tag{2.32}$$

where $k_B = 1.38067 \times 10^{-16}\, erg\, K^{-1}$ is Boltzmann's constant, and $m_H = 1.6735 \times 10^{-24}\, g$ is the mass of a hydrogen atom. The gravitational acceleration is chosen so that the density falls to $0.25e^{1/2}n(0)$ over region 2, resulting in $\mathbf{g} = -1.03125 \times$

$10^{-10}\, cm\, s^{-2}$. At $t=0$ a perturbation is applied to the vertical velocity at the interface such that

$$v_y(x,y) = .001 c_2 \sin\left(\frac{2\pi x}{\lambda}\right) e^{\frac{2\pi}{\lambda}|y-y(0)|}, \tag{2.33}$$

where $c_2$ is the sound speed in region 2, $c_2^2 = \gamma k_B T_2/\mu m_H$. A small fraction of the sound speed is chosen as the maximum perturbation amplitude in order to approximate an incompressible fluid. The chosen wavelength is one-fourth the total grid size, $\lambda = 2.5 \times 10^{17}\, cm$, which corresponds to a horizontal wave number $k = 2\pi/\lambda = 2.51 \times 10^{-17}\, cm^{-1}$. Solving for the linear growth rate using equation (2.30) yields $\omega = 2.94 \times 10^{-14}\, s^{-1}$. Inverting the growth rate results in the e-folding time for the problem, $t_e = \omega^{-1} = 3.40 \times 10^{13}\, s$. Figure (2.3) shows the density distribution at 4,6,8, and 10 $e$-folding times. Early in the simulation, the visible growth of the instability is small due to the large cell size, small velocity perturbation, and small gravitational acceleration. The initial wavelength is preserved well into the nonlinear phase of the instability. The boundary conditions give rise to some asymmetry near the left and right boundaries. As the instability evolves, the downward velocity of the heavy fluid increases. At late times, the velocity shear is great enough to give rise to mushroom caps due to the Kelvin-Helmholtz instability. These results compare well to laboratory scale calculations by Jun et al. (1995). More detailed RT simulations are presented in the next chapter.

## 2.2 Self-Gravity Routines

On astrophysical scales, gravitational forces play an enormous role in the evolution of gas clouds. In order for a gas cloud to evolve into a protostar, gravity must at some point overwhelm the pressure forces acting against collapse. To study the effects of self-gravity upon interfacial instabilities, I built a gravity solver to be implemented within the structure of CFDLIB. This section describes the methods used for the gravity solver and shows the test problem of a collapsing sphere.

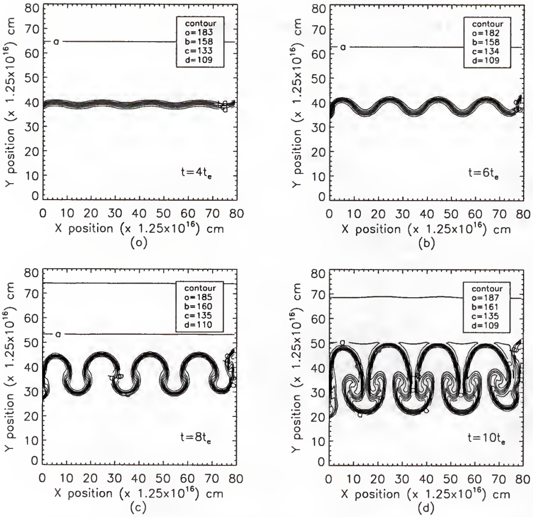

Figure 2.3: Rayleigh-Taylor instability growth. Contours show the number density of molecular hydrogen at a)$4t_e$; b)$6t_e$; c)$8t_e$; and d)$10t_e$. The e-folding time $t_e = 3.40 \times 10^{13}\,s$.

Forces arising from self-gravity are easily added into the ICE-ALE procedure by incorporating them into the body force terms in the primary and Lagrangian steps. The forces themselves are given by the gradient of the self-gravitational potential, $\mathbf{f} = \nabla\Phi$. It is simpler and quicker to solve for the scalar potential than the vector forces. The self-gravitational potential $\Phi$ for a fluid is found by solving the Poisson equation

$$\nabla^2\Phi = -4\pi G\rho, \tag{2.34}$$

where $G$ is Newton's Gravitational constant ($G = 6.6742 \times 10^{-8}\, cm^3 g^{-1} s^{-2}$). Whereas the equations of fluid dynamics, equations (2.1-2.3), are hyperbolic equations, the Poisson equation is an elliptic equation. Elliptic equations are also called boundary value problems (both hyperbolic and parabolic equations are initial value problems) and require different methods to solve than hyperbolic equations. Poisson's equation contains no time dependence; the potential value in each cell throughout the mesh must be solved for simultaneously. Finding the solution comes down to solving a set of nonlinear algebraic equations by linearization and iteration. The solution is very sensitive to the boundary conditions. Many methods exist to solve elliptic equations, such as Fourier techniques, conjugate gradient methods, or multigrid methods. The solver implemented in CFDLIB is a multigrid solver. The multigrid method is as fast as other methods, and it retains more generality in choosing boundary conditions and cell sizes. The name of the employed multigrid code is MUDPACK (Adams 1989,1991), a freely available program developed by John Adams at the National Center for Atmospheric Research. MUDPACK is a collection of Fortran subroutines created to make multigrid methods available in a user friendly form. The self-gravity routine added to CFDLIB consists of parts of MUDPACK along with code to allow communication between CFDLIB and MUDPACK. The potential values are calculated after the state variables have been remapped to the Eulerian grid to ensure that the cell size is a constant in each direction.

Multigrid methods combine the use of basic iteration techniques with a process of stepping the solution down to coarser grids to speed convergence. With iteration techniques, a sequence of approximate solutions is generated until convergence to a solution is achieved. As an example, consider the one-dimensional, second order discrete form of the Poisson equation,

$$\Phi_{i-1} - 2\Phi_i + \Phi_{i+1} = -4\pi G\rho_i h^2, \tag{2.35}$$

where $h$ is the cell size. Letting $b_i = -4\pi G\rho_i h^2$, this equation can be written in matrix form as $\mathbf{Ax} = \mathbf{b}$ with the definitions,

$$\mathbf{A} = \begin{pmatrix} -2 & 1 & 0 & 0 & \cdots \\ 1 & -2 & 1 & \ddots & \ddots \\ 0 & 1 & \ddots & \ddots & 0 \\ 0 & \ddots & \ddots & -2 & 1 \\ \vdots & \ddots & 0 & 1 & -2 \end{pmatrix}, \mathbf{x} = \begin{pmatrix} \Phi_1 \\ \Phi_2 \\ \Phi_3 \\ \vdots \\ \vdots \end{pmatrix}, \mathbf{b} = \begin{pmatrix} -4\pi G\rho_1 h^2 \\ -4\pi G\rho_2 h^2 \\ -4\pi G\rho_3 h^2 \\ \vdots \\ \vdots \end{pmatrix}.$$

The matrix $\mathbf{A}$ is symmetric, tridiagonal, and sparse. Iterative techniques exploit the sparse nature of the matrix. The simplest iterative method is the Jacobi method. This method starts off with an initial guess for $\mathbf{x}$. All the components of $\mathbf{x}$ are then updated simultaneously using the simple relation,

$$x_i^{(k+1)} = (b_i - \sum_{j\neq i} a_{i,j} x_j^{(k)})/a_{i,i}. \tag{2.36}$$

Since $\mathbf{A}$ is sparse, most of the $a_{i,j}$ terms are zero, so each value of $x_i$ is updated as a function only of its closest neighbors. The iteration continues until convergence is achieved. Notice that in the Jacobi method, each updated value $x_i^{(k+1)}$ is a function only of values from the previous iteration. The order in which the updated values are calculated does not matter. The Gauss-Seidel method is similar to the Jacobi method, except that updated values are used as soon as they are calculated. The order in which the components of $\mathbf{x}$ are updated becomes important. For example, values can be updated according to the relation

$$x_i^{(k+1)} = (b_i - \sum_{j<i} a_{i,j} x_j^{(k+1)} \sum_{j>i} a_{i,j} x_j^{(k)})/a_{i,i}. \tag{2.37}$$

The Gauss-Seidel method requires less storage than the Jacobi method, and will converge with fewer iterations for most problems. The direction of the iteration need not be the same each time. In the symmetric Gauss-Seidel method the update order is alternated between the ascending and descending directions. Another variation involves updating the even and odd components in alternating order. For the tridiagonal matrix **A**, the even components are updated as a function of the odd components, and vice versa. This process is called the red-black Gauss-Seidel method. More advanced iterative methods such as successive over-relaxation and weighted function methods exist as well, but with multigrid techniques the simplest iterative techniques are sufficient.

MUDPACK uses the red-black Gauss-Seidel method as the iteration technique. Like most iterative techniques, the Gauss-Seidel method suffers from some major drawbacks. Convergence is often very slow. If the initial guess is very wrong, convergence may never happen. Multigrid techniques provide a way to overcome these problems. Iterative techniques have a smoothing property (Briggs 1987) in that they quickly eliminate oscillatory (high frequency) modes while leaving smooth (low frequency) modes intact. Just a few iterations are sufficient to remove the oscillatory modes, but to remove the smooth modes requires many more. The key to multigrid techniques is that a smooth mode on one grid appears more oscillatory on a coarser grid. Figure (2.4) shows an example of this phenomenon. A sine wave that is smooth on a 12 point grid becomes more oscillatory if every other data point is transferred onto a grid with one-half the resolution. In a multigrid process, a problem might begin on the finest grid. After a few iterations on the fine grid, a method of restriction is used to transfer the problem to a coarser (usually by a factor of 2 in each direction) grid where another sequence of iterations is performed. A process of interpolation can be used to transfer the solution back onto the finer mesh. Typically more than two grid sizes are used. The problem is simply transferred from grid to

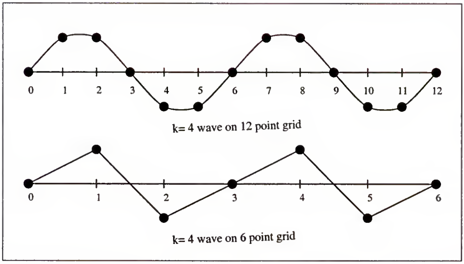

Figure 2.4: An example of switching grid resolutions to alter the nature of a function. A smooth function on a fine 12 point grid appears more oscillatory on a coarser 6 point grid.

grid as needed to achieve convergence of the overall problem in a short time. In cases in which there is no initial guess available to begin the iteration on the finest grid, the process can begin on the coarsest grid and advance to finer and finer grids. A starting initial value is determined for each grid in turn. The ordering of the grids is shown in figure (2.5) for this procedure. A sequence of cycles is used to build up to an initial approximation to the solution on the finest grid. A full cycle down to the coarsest grid and back up to the finest grid is then completed to improve the solution. This process is known as the full multigrid V-cycle (FMV) and is one of the processes used by MUDPACK. Other variations make use of even more cycles to improve the solution on the finest grid. Because only a few iterations are needed on each grid the overall process remains very efficient.

MUDPACK accepts three types of boundary conditions: periodic, specified value (Dirichlet), and mixed derivative (Neumann). The appropriate type of boundary condition is determined by the nature of the simulation. Periodic boundary conditions approximate an infinitely extended grid. For some problems periodic

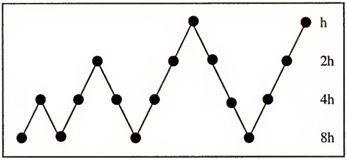

Figure 2.5: A schematic look at the grid schedule in the FMV method. The process begins on the coarsest grid and ends on the finest grid. The characteristic cell size of the finest grid is h, and each subsequent step to a coarser grid results in twice the cell size. A sequence of iterations is performed on each grid.

boundaries work very well, provided that the grid is made large enough that the area of interest is well removed from the boundaries. For models that use cylindrical symmetry, periodic boundaries are not applicable at the symmetry axis or outer radial boundary. Therefore, a model with cylindrical symmetry, or Cartesian symmetry if not well approximated by an infinitely extended grid, requires specified value or derivative boundaries. The choice between specified value or derivative boundaries is usually determined by practical considerations. The derivative boundary conditions are applied on all grids, whereas specified value boundaries are only specified on the finest grid. When the potential remains relatively unchanged for long intervals of time, an approximate analytical formula for the boundaries can be applied. This is typically the case when a simulation is started from a state of hydrodynamic equilibrium and the total mass over the grid remains constant. A slowly changing potential enables the efficient use of both specified value and specified derivative boundary conditions. On the other hand, if the problem under consideration involves a changing total mass or the gas is highly compressible, the potential will vary greatly over time. In this case, boundary values must be approximated computationally using information within the grid, and specified value boundaries are more practical since they need be calculated only once per time step. For two-dimensional cases with imposed cylindrical symmetry, the potential can be specified for a boundary cell by explicitly summing the contributions from all other cells. Each cell defines an annulus of constant density. The potential in each boundary cell is determined by breaking up each annulus into small pieces and treating each piece as a point mass. The sum of potentials from all pieces is the potential for the boundary cell. Once the boundary values are specified, MUDPACK very quickly solves for the potential over the interior of the grid. Experiments have shown that increasing the number of divisions for each annulus beyond 24 results in only a minor increase in accuracy.

A simple example for which an analytic expression for the potential exists is the problem of a collapsing sphere. A sphere with internal density $\rho$ and temperature $T$ will collapse if its radius exceeds the Jeans length

$$\lambda_J = \sqrt{\frac{\pi\gamma RT}{\mu G\rho}}. \tag{2.38}$$

For a sphere with radius $a$, the interior potential at a distance $r$ from the center is

$$\Phi(r) = (2/3)\pi G\rho(3a^2 - r^2). \tag{2.39}$$

The external potential for $r > a$ is

$$\Phi(r) = (4/3)\pi G\rho a^3 r^{-1}. \tag{2.40}$$

To calculate the potential numerically, a 49x97 grid is created with cylindrical geometry. The cell size is $5 \times 10^{15}\, cm$ for both the $r$ and $z$ directions. A sphere with a radius of 35 cells ($1.75 \times 10^{17}\, cm$) and constant density $1.0 \times 10^{-18}\, g\, cm^{-3}$ is placed on the grid. Figure (2.6) shows the shape of the initial density distribution. The shape is not truly spherical since the individual cells are all rectangular. The density outside the sphere is $1.0 \times 10^{-50}\, g\, cm^{-3}$. A constant temperature of $5\, K$ is applied throughout the entire grid, and an ideal gas equation of state is used with $\gamma = 1.4$. For the temperature and interior density chosen, the Jeans length is less than the radius,

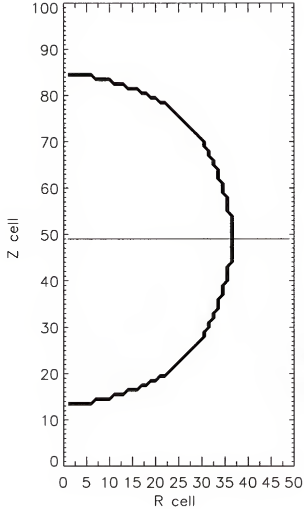

Figure 2.6: Initial density distribution for the collapsing sphere. The sphere has radius $a = 1.75 \times 10^{17}\, cm$ and interior density $\rho_i = 1.0 \times 10^{-18}\, g\, cm^{-3}$. The exterior density is $\rho_e = 1.0 \times 10^{-50}\, g\, cm^{-3}$.

$\lambda_J = 1.17 \times 10^{17}\,cm = 23.4\,cells$. The numerical and analytical solutions for the potential at $t=0$ are shown in figure (2.7) along with the difference and relative difference between them. The numerical and analytic solutions show good agreement considering that the numerical approximation is not a true sphere. The numerical solution for the potential is everywhere greater than the corresponding analytic solution. The maximum difference of 5.4% occurs at the edge of the sphere.

A sphere exceeding the critical Jeans length will collapse in roughly a free-fall time given by

$$t_{ff} = \sqrt{\frac{3\pi}{32G\rho}}. \tag{2.41}$$

For the sphere considered here, $t_{ff} = 2.10 \times 10^{13}\,s$. The collapse of the sphere is depicted in figure (2.8) with density contours displayed at different fractions of the free-fall time. At $t=t_{ff}$, the density at the center of the collapsed sphere has reached a value of $4.88 \times 10^{-16}\,g\,cm^{-3}$, which is nearly the density needed for a single cell to be Jeans unstable. The collapse cannot be followed further without finer mesh resolution.

## 2.3 Cooling Routines

Thermodynamic processes play a key role in the evolution of interstellar material. Indeed, an efficient cooling mechanism is vital to the process of star formation. In dense, cool molecular clouds, the dominant form of cooling is the collisional excitation of atoms and molecules followed by the spontaneous emission of photons. The dominant atomic species H and He lack the low energy transitions to be efficient coolants at low temperatures. The most abundant molecule, $H_2$, is an ineffective coolant at low temperatures due to a lack of low-lying rotational energy states. At high densities, $H_2$ cooling is strongly quenched by collisional de-excitation because the molecule lacks an electric dipole moment. Therefore, carbon and oxygen bearing molecules play a large role in driving the gas cooling in molecular clouds. For the

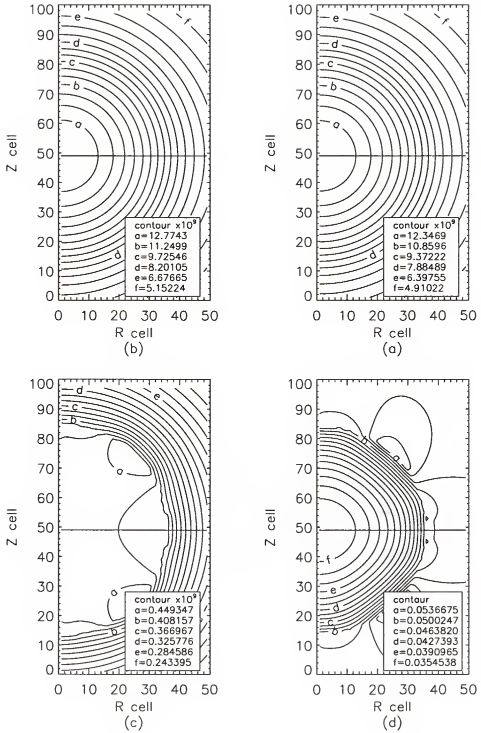

Figure 2.7: Comparison between numerical and analytical solutions for the potential of a solid sphere. a) results from the numerical algorithm; b) results from the analytic formulae; c) (numerical-analytic) d) (numerical-analytic)/analytic.

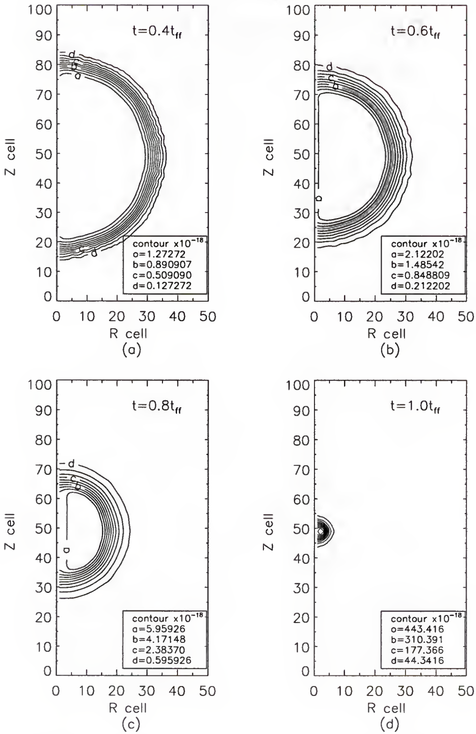

Figure 2.8: Time evolution of a collapsing sphere. The plots show the density contours at times a)$0.4t_{ff}$; b)$0.6t_{ff}$; c)$0.8t_{ff}$; and d)$1.0t_{ff}$. The free-fall time $t_{ff} = 2.10 \times 10^{12}\, s$.

low temperatures and densities considered in this study, CO is the major coolant, with O playing a larger role as the temperature increases and $H_2O$ contributing in the shocked, heated regions.

For a gas with density $\rho$ and pressure $p$, the First Law of Thermodynamics can be written;

$$\frac{dp}{dt} = \frac{\gamma p}{\rho}\frac{d\rho}{dt} + (\gamma - 1)(H - C). \tag{2.42}$$

The term $(H-C)$ accounts for the change in heat, $(H-C) = \rho dQ/dt$, where $H$ is the heating rate and $C$ is the cooling rate. For a gas obeying the ideal gas law, equation (2.9), the First Law can be recast into an equation for the temperature evolution,

$$\frac{dT}{dt} = (\gamma - 1)\frac{T}{\rho}\frac{d\rho}{dt} + \frac{T}{t_c}(\frac{H}{C} - 1). \tag{2.43}$$

The cooling time-scale $t_c$ is defined as $t_c = p/[(\gamma - 1)C]$. For the case in which the cooling rate is much greater than the heating rate ($H/C \lll 1$), equation (2.43) reduces to

$$\frac{dT}{dt} = (\gamma - 1)\frac{T}{\rho}\frac{d\rho}{dt} - \frac{T}{t_c}. \tag{2.44}$$

The first term on the right hand side of equation (2.44) represents the temperature change due to adiabatic processes. The second term represents the change in temperature due to radiative cooling. The cooling time-scale is much less than the dynamical time-scale of the problem. The temperature is updated in each cell once per timestep, and a minimum temperature (typically 5 $K$) is maintained to account for diffuse heating by cosmic rays. The cooling is applied during the Lagrangian phase of the ICE-ALE cycle.

The cooling rates used are the tabulated rates of Neufeld, Lepp, and Melnick (1995, hereafter NLM). The models of NLM provide the total cooling rates for dense molecular gas over a wide range of density and temperature. The rates include a full consideration of chemical abundances for 389 species made up from the elements H, He, O, C, N, Si, S, Na, Cl, Fe, P, and Mg. Cooling functions were obtained for $H_2$,

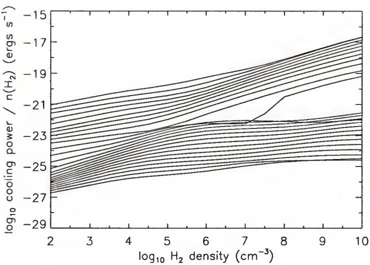

Figure 2.9: Cooling rates. This plot is a reproduction of figure (3a) from Neufeld et al. 1995. Each curve corresponds to a different temperature, with $T = 10\,K$ being the lowest curve and $T = 10^{3.4}\,K$ the highest.

$H_2O$, CO, $O_2$, HCl, C, and O. The total cooling rates are displayed in figure (2.9), which is a reproduction of figure (3a) of NLM extended to lower densities. Each curve tracks the cooling power versus $H_2$ number density for a constant temperature. The temperatures range from $T = 10\,K$ (the lowest curve) to $T = 10^{3.4} K$ (the highest curve) in logarithmic intervals of 0.1 dex in temperature. A large increase occurs at high densities for $T \geq 300\,K$ due to an increase in $H_2O$ abundance and the large dipole moment of the water molecule. For a given density and temperature, a cooling rate is found by linear interpolation between tabulated data values. In determining cooling rates, NLM define an optical depth parameter in terms of the local velocity gradient $dv_z/dz$ as

$$\tilde{N}(M) = \frac{\Gamma n(M)}{|dv_z/dz|}, \tag{2.45}$$

where $n(M)$ is the number density of species M, and $\Gamma$ is a geometric form factor set to unity for the plane parallel case. A value of $\tilde{N}(M) = 10^{20}\,cm^{-2}\,km^{-1}\,s$ is used in this study because it is the lowest optical depth available.

Although no truly comprehensive model for interstellar cooling has been developed, the NLM models are considered to be among the best. The NLM models include the effects of many chemical species in determining the cooling rates, but the models do have some limitations and possible sources of error. The models consider only steady state chemistry and ignore time dependent processes such as the evaporation of icy grain mantles. Direct cooling by grains is also not included. Evidence exists which suggests that dust cooling dominates behind shocks in molecular clouds (Whitworth and Clarke 1997). If this is the case, the NLM models underestimate the cooling rates in shocked regions. NLM assume that heating due to an infrared dust continuum or radioactive decay is negligible, and they only consider fully-shielded regions. If external ultraviolet radiation is able to penetrate a region, photodissociation will alter the chemical abundances in the cloud. Recent observations of the Orion BN/KL region may indicate that the NLM models overestimate the abundances of the two important molecular species $H_2O$ and $O_2$ (Bergin et al. 2000). Although CO is the dominant coolant for low temperature, low density gas, the NLM model predicts that $O_2$ should account for about 20% of the cooling at low density. Water contributes about 10% of the cooling power at low temperatures. If the observations are typical of molecular clouds, the NLM models overestimate the overall cooling rates by a nontrivial amount for regions with low temperatures or low densities. In shocked regions, the abundance of water is observed to be much higher than in quiescent regions. So water remains an important coolant in shocked regions, as predicted by NLM. The possible sources of error in the NLM models are offsetting to some degree. The effects of altering the cooling rates are investigated by parameterizing the amount of cooling for a sequence of otherwise identical models. A coefficient is applied to the cooling term in equation (2.44) to allow various degrees of cooling from zero to the full NLM cooling rates. The results are presented in a later chapter.

# CHAPTER 3
# SELF-GRAVITY DRIVEN INTERFACIAL INSTABILITIES

Interfacial instabilities are an important feature of the ISM. Dynamic gas flows driven by a variety of mechanisms constantly interact in interesting ways. For example, a velocity shear at the interface between two fluids drives the Kelvin-Helmholtz instability. The Rayleigh-Taylor instability arises when a fluid is accelerated into a more tenuous fluid. In a recent paper, Hunter, Whitaker, and Lovelace (1997, hereafter HWL) identified a new type of instability which acts upon an interface of discontinuous density and is driven by self-gravity. In this chapter, I discuss this self-gravity interfacial instability (SGI) in Cartesian geometry. The theory of HWL is summarized, the computational models are described, and results are presented.

## 3.1 Theory

The discovery of the SGI came about as part of an ongoing study of interfacial instabilities in the ISM. To explore the nature of interfacial instabilities, Hunter and Whitaker (1987, 1989) considered the stability of two semi-infinite, uniform fluids in relative motion having constant, but generally unequal, unperturbed densities, temperatures, and magnetic field strengths. They used a normal mode analysis to study compressible Kelvin-Helmholtz instabilities and identify a largely supersonic thermal-dynamic instability which arises due to a coupling between the dynamics and thermodynamics of the fluids. As a next step, HWL included self-gravity in the analysis. By doing so, they were able to identify the SGI, an interfacial instability driven by self-gravity that acts upon any interface of discontinuous density. The SGI persists in the static limit and has a characteristic growth rate of the order of the free-fall time in the denser fluid.

In their initial analysis of the SGI, HWL considered non-stratified, compressible media with an interface characterized by a velocity slip as well as a density discontinuity. In the analysis below, I consider only the static, incompressible case. A full normal mode analysis for the determination of the growth rate is presented by HWL and not reproduced here. HWL also present a truncated derivation of the SGI growth rate using the energy principle method of Bernstein et al. (1958). The result is the same in the static, incompressible limit. A planar interface at $y=0$ is placed in equilibrium between two regions of different densities, $\rho_1$ below the interface and $\rho_2$ above. The background acceleration (effective gravity) is $\mathbf{g} = g\hat{y}$, where $\hat{y}$ is a unit vector in the $y$-direction. A distinction must be made between $\mathbf{g}$ and the acceleration due to the self-gravitational potential $\Phi$. A linear perturbation is applied to the equilibrium configuration such that any perturbed quantity $\eta'$ is written

$$\eta' = \eta_0' e^{-i(\omega t - kx)} e^{|-ky|}. \tag{3.1}$$

The perturbation results in the linear equations,

$$\frac{\partial \rho'}{\partial t} = -\nabla \cdot (\rho v'), \tag{3.2}$$

$$\rho \frac{\partial v'}{\partial t} = -\nabla p' + \mathbf{g}\rho' + \rho \nabla \Phi' + [(\nabla \Phi)\rho'], \tag{3.3}$$

$$\frac{\partial p'}{\partial t} = -v' \cdot \nabla p - \gamma p \nabla \cdot v'. \tag{3.4}$$

In the above, $p$ is the fluid pressure, $v$ the velocity, and $\gamma$ the ratio of specific heats. The perturbed Poisson equation is

$$\nabla^2 \Phi' = -4\pi G \rho'. \tag{3.5}$$

In the incompressible limit, $\rho' = 0$ except at the interface, so the bracketed term in equation (3.3) can be dropped. To examine the perturbed equations, a first order, Lagrangian displacement $\varepsilon$ is defined such that the perturbed velocity is given by $v' = \partial\varepsilon/\partial t$ (Bernstein et al. 1958). The equations for the perturbed density and pressure can then be expressed as

$$\rho' = -\nabla \cdot (\rho\varepsilon) \tag{3.6}$$

and

$$p' = -(\varepsilon \cdot \nabla)p - \gamma p \nabla \cdot \varepsilon. \tag{3.7}$$

The perturbed momentum equation takes the form

$$\rho \frac{\partial^2 \varepsilon}{\partial t^2} = -\mathbf{F}(\varepsilon), \tag{3.8}$$

where $\mathbf{F}$ is a linear, self-adjoint operator on $\varepsilon$. For a perturbation of the form given in equation (3.1), the above equation becomes

$$\omega^2 \rho\varepsilon = -\mathbf{F}(\varepsilon). \tag{3.9}$$

Upon forming the dot product of this equation with $\varepsilon^*$ (the complex conjugate of $\varepsilon$), integration over space and integration by parts leads to an energy principle,

$$\omega^2 \int d^3x \rho\varepsilon^* \cdot \varepsilon = \int d^3x [\gamma p \mid \nabla \cdot \varepsilon \mid^2 + (\nabla \cdot \varepsilon^*)(\varepsilon \cdot \nabla) p] + \int d^3x \mathbf{g} \cdot \varepsilon^* [\nabla \cdot (\rho\varepsilon)] - \int d^3x \rho\varepsilon^* \cdot \nabla\Phi'. \tag{3.10}$$

The integrals appearing on the right hand side of equation (3.10) have evident physical interpretations: the first describes the generally stabilizing influence of compressibility, the second is associated with the familiar Rayleigh-Taylor (RT) instability, and the third represents the destabilizing effect of self-gravity upon the interface. For the incompressible case, $\nabla \cdot \varepsilon = \nabla \cdot \varepsilon^* = 0$, so the first two terms drop out. The remaining integrals are evaluated to give the incompressible growth rate,

$$\omega^2 = \frac{-2\pi G(\rho_2 - \rho_1)^2}{\rho_2 + \rho_1} + \frac{gk(\rho_2 - \rho_1)}{\rho_2 + \rho_1}. \tag{3.11}$$

The second term in equation (3.11) is the growth rate for the incompressible RT instability. The first term gives the new result of HWL, the incompressible growth rate for the SGI. Several important differences are apparent. Self-gravity is destabilizing across any interface of discontinuous density, whereas the interface is RT unstable only if $g(\rho_2 - \rho_1) < 0$. For the SGI, the growth rate depends upon the density of the environment as well as the density contrast at the interface, but not upon the perturbation wavelength. In contrast, the growth of the RT instability depends upon the density contrast and the perturbation wavelength, but not the background density. For a fixed value of $g$, the SGI grows more rapidly than the RT instability in relatively dense regions with relatively long wavelength perturbations, such that $\lambda = 2\pi/k > g/G|\rho_2 - \rho_1|$.

The physical origin of the SGI can be explained as follows (HWL). For specificity, let the density below the interface ($\rho_1$) be greater than the density above the interface ($\rho_2$). The first term in equation (3.11) can be traced to the pressure difference across the interface. An upward distortion of the interface, $\varepsilon_y(x)$, results in a mass excess proportional to $(\rho_1 - \rho_2)\varepsilon_y(x)$. This in turn produces a positive perturbation of the gravitational potential $\Phi$; thus, $\Phi' > 0$ in the nearby space above and below the interface. An increase in the fluid pressure results owing to Bernoulli's equation, which in the static limit reduces to $p' = \rho\Phi'$. The potential is continuous across the interface, so the pressure below the interface, $p_1' = \rho_1\Phi'$, is larger than that above, $p_2' = \rho_2\Phi'$. The pressure difference across the interface causes the distortion to grow.

For their primary analysis, HWL considered non-stratified media above and below the interface, such that the density is constant in each region. In addition, they considered an isothermal case with density stratifications deduced from the solution to Poisson's equation. They found that the growth rate for the stratified case has the same form as equation (3.11) provided the perturbation wavelength is much smaller than the Jeans length. Therefore, numerical models with stratified density distributions are expected to show SGI growth rates in good agreement with equation

(3.11) when perturbation wavelengths are small, but the deviation from equation (3.11) will grow larger as the perturbation wavelength increases to an appreciable fraction of the Jeans length.

## 3.2 Models

In order to study the SGI, models are given initial conditions that correspond to hydrostatic equilibrium. Because the ISM is a turbulent medium, a configuration of hydrostatic equilibrium is extremely unlikely to occur, so the results of these models are not directly comparable to observations. However, an equilibrium is necessary in order to study the SGI in isolation without other processes interfering. Once this is accomplished, more comprehensive models of the ISM can be formed to study the effects of the SGI when coupled to other phenomena, such as magnetic, thermal, or dynamic instabilities. For instance, velocity shear must be added to test the theory of HWL that the SGI enhances the growth of the Kelvin-Helmholtz instability for small to moderate Mach numbers. This type of problem is left for later work. All models in this chapter are presented with time units in terms of the theoretical e-folding time $t_e$, defined as the time needed for a perturbed quantity to grow by a factor of $e$. The e-folding time is the reciprocal of the theoretical growth rate, $1t_e = \omega^{-1}$.

When a fluid is in hydrostatic equilibrium, the forces due to self-gravity and thermal pressure exactly balance, so the gas remains at rest. Typically, hydrostatic equilibrium is invoked in spherical models of stars. However, the same principle may be applied in other geometries as well. The SGI models employ a square Cartesian $(x, y)$ grid with either 129 or 257 cells in each direction. The 2-D equilibrium problem with planar symmetry reduces to a 1-D problem; only the direction normal to the interface need be considered. The equilibrium configuration for each region is solved for independently from the other as a function of $y$, where $y \geq 0$ is the distance from the interface. The initial density and temperature distributions are determined by simultaneously solving the equation of hydrostatic equilibrium and Poisson's equation.

The equation of hydrostatic equilibrium is

$$\frac{1}{\rho}\frac{dp}{dy} = \frac{d\Phi}{dy}. \tag{3.12}$$

A polytropic equation of state is used, so that,

$$p = \kappa \rho^{\gamma}, \tag{3.13}$$

where the constant $\kappa$ is determined by the values of $p$ and $\rho$ at the interface, $\kappa = p_0/{\rho_0}^{\gamma}$. The polytropic relation allows the replacement of the pressure in the hydrostatic equation with a simple function of the density. Poisson's equation, equation (2.34), simplifies in the 1-D Cartesian case to

$$\frac{d^2\Phi}{dy^2} = -4\pi G\rho. \tag{3.14}$$

The combination of equations (3.12-3.14) results in a differential equation for the density distribution,

$$\frac{d^2\rho}{dy^2} + \frac{(\gamma-2)}{\rho}\left(\frac{d\rho}{dy}\right)^2 + \frac{4\pi G\rho^{(3-\gamma)}}{\gamma\kappa} = 0. \tag{3.15}$$

For the special case that $\gamma = 2$, the second term drops out leaving

$$\frac{d^2\rho}{dy^2} = -\frac{2\pi G\rho}{\kappa}. \tag{3.16}$$

The boundary values for this problem are such that at the interface, the density is a maximum ($\rho = \rho_0$) and the gradient of the density goes to zero ($d\rho/dy = 0$). Under these conditions, the solution to equation (3.16) is

$$\rho = \rho_0 \cos\left(\frac{y}{a}\right). \tag{3.17}$$

Valid densities are found from $y = 0$ to $(y/a) = \pi/2$, although for best results the scale height $a$ is chosen so that $y/a$ is still significantly less than $\pi/2$ at the grid boundaries. The scale height is determined by the density and temperature at the interface. For $\gamma = 2$,

$$a^2 = \frac{\kappa}{2\pi G} = \frac{1}{2\pi G}\frac{R}{\mu}\frac{T_0}{\rho_0}, \tag{3.18}$$

where $R$ and $\mu$ are the gas constant and molecular weight, respectively. The ideal gas equation of state, equation (2.9), can be used to determine the temperature distribution once the density and pressure are known. For the $\gamma=2$ case, the temperature follows the same distribution as the density,

$$T = T_0 \cos\left(\frac{y}{a}\right). \tag{3.19}$$

Although unphysical and not applicable to the ISM, the choice of $\gamma = 2$ is useful for several reasons. The very stiff equation of state aids in limiting models to the incompressible regime. More importantly, the analytic solution was used in debugging the computational method used for all SGI models. The analytic solution provides a means by which to test the numerical solver developed for general values of $\gamma$.

In order to better represent the ISM, a method for determining equilibrium conditions for adiabatic models with any value of $\gamma$ has been developed. The general solution of equation (3.15) requires a numerical integration. The problem is simplified by recasting the problem in the so-called Emden variables (e.g. Chandrasekhar 1939). A dimensionless variable $\theta$ is used to parameterize the temperature, density, and pressure of a polytropic gas as

$$T = T_0\theta \qquad \rho = \rho_0\theta^n \qquad p = p_0\theta^{(n+1)}. \tag{3.20}$$

As before, the subscripts denote values at the interface. The polytropic index $n$ is related to $\gamma$ by $n = 1/(\gamma - 1)$. Rewriting equation (3.15) as a function of $\theta$ results in a simpler equation,

$$a^2\frac{d^2\theta}{dy^2} = -\theta^n. \tag{3.21}$$

As in the $\gamma=2$ case, the scale height $a$ is determined from the density and temperature at the interface. For general $n$,

$$a^2 = \left(\frac{\kappa(n+1)}{4\pi G}\right)\rho_0{}^{\left(\frac{1-n}{n}\right)} = \frac{(n+1)}{4\pi G}\frac{R}{\mu}\frac{T_0}{\rho_0}. \tag{3.22}$$

The problem is simplified further by the definition of another dimensionless variable $\xi$ such that $y = a\xi$. When $\xi$ is substituted into equation (3.21), the result is a Cartesian analog to the Lane-Emden equation,

$$\frac{d^2\theta}{d\xi^2} = -\theta^n. \tag{3.23}$$

The choice of $\gamma=2$ ($n=1$) reproduces equation (3.16). A particularly simple solution to equation (3.23) exists for the strictly incompressible case $\gamma = \infty$ ($n = 0$). As mentioned in HWL, the isothermal case $\gamma=1$ ($n = \infty$) has an analytic solution, as does the $\gamma=2/3$ ($n=-3$) case. To solve for the equilibrium state for any other value of $\gamma$, a fourth order Runge-Kutta numerical integration scheme (Press et al. 1992) is employed. The numerical and analytic solutions show excellent agreement for both the $\gamma=1$ and $\gamma=2$ cases. As an example, Table (3.1) compares the numerical values of $\theta(\xi)$ with the analytical values of $\cos(\xi)$ in the denser region for the $\gamma=2$ model masg129d1. The agreement is perfect to the edge of the grid. The Runge-Kutta solver uses a resolution four times finer than the CFDLIB grid for improved accuracy and to obtain $\theta(\xi)$ and $d\theta/d\xi$ at both cell centers and cell faces. Having determined $\theta(\xi)$, density and temperature values throughout the grid are assigned using equations (3.20). An example of the initial density and temperature distributions for the SGI model cnsg257e1 is shown in figure (3.1). This model has a relatively small scale height, which results in the steep density decline in the denser medium.

In setting up an equilibrium configuration, boundary conditions must be carefully considered. For constraining the dynamic processes of the simulation within CFDLIB, reflective boundary conditions have proven most successful in maintaining pressure equilibrium along all four edges. Two types of boundary conditions are implemented in MUDPACK to confine the potential solution. Along the left and right boundaries, periodic boundary conditions are used. This is a logical choice given the symmetry of the problem and results in the necessity for the perturbation function to be periodic as well. The top and bottom boundaries are constrained by values of

Table 3.1: Comparison of numerical and analytical results

| $y^\dagger$ | $\xi = y/a$ | numerical $\theta(\xi)$ | analytical $\cos(\xi)$ |
|---|---|---|---|
| 1.E+16 | 0.0039269908 | 0.999992289 | 0.999992289 |
| 5.E+16 | 0.019634954 | 0.99980724 | 0.99980724 |
| 9.E+16 | 0.0353429172 | 0.999375504 | 0.999375504 |
| 1.3E+17 | 0.0510508804 | 0.998697187 | 0.998697187 |
| 1.7E+17 | 0.0667588436 | 0.997772456 | 0.997772456 |
| 2.1E+17 | 0.0824668068 | 0.99660154 | 0.99660154 |
| 2.5E+17 | 0.09817477 | 0.995184727 | 0.995184727 |
| 2.9E+17 | 0.113882733 | 0.993522367 | 0.993522367 |
| 3.3E+17 | 0.129590696 | 0.99161487 | 0.99161487 |
| 3.7E+17 | 0.14529866 | 0.989462708 | 0.989462708 |
| 4.1E+17 | 0.161006623 | 0.98706641 | 0.98706641 |
| 4.5E+17 | 0.176714586 | 0.984426568 | 0.984426568 |
| 4.9E+17 | 0.192422549 | 0.981543834 | 0.981543834 |
| 5.3E+17 | 0.208130512 | 0.978418919 | 0.978418919 |
| 5.7E+17 | 0.223838476 | 0.975052593 | 0.975052593 |
| 6.1E+17 | 0.239546439 | 0.971445688 | 0.971445688 |
| 6.5E+17 | 0.255254402 | 0.967599093 | 0.967599093 |
| 6.9E+17 | 0.270962365 | 0.963513757 | 0.963513757 |
| 7.3E+17 | 0.286670328 | 0.959190689 | 0.959190689 |
| 7.7E+17 | 0.302378292 | 0.954630955 | 0.954630955 |
| 8.1E+17 | 0.318086255 | 0.94983568 | 0.94983568 |
| 8.5E+17 | 0.333794218 | 0.944806047 | 0.944806047 |
| 8.9E+17 | 0.349502181 | 0.939543297 | 0.939543297 |
| 9.3E+17 | 0.365210144 | 0.93404873 | 0.93404873 |
| 9.7E+17 | 0.380918108 | 0.928323699 | 0.928323699 |
| 1.01E+18 | 0.396626071 | 0.922369619 | 0.922369619 |
| 1.05E+18 | 0.412334034 | 0.916187958 | 0.916187958 |
| 1.09E+18 | 0.428041997 | 0.909780241 | 0.909780241 |
| 1.13E+18 | 0.44374996 | 0.903148049 | 0.903148049 |
| 1.17E+18 | 0.459457924 | 0.89629302 | 0.89629302 |
| 1.21E+18 | 0.475165887 | 0.889216843 | 0.889216843 |
| 1.25E+18 | 0.49087385 | 0.881921265 | 0.881921265 |
| 1.29E+18 | 0.506581813 | 0.874408087 | 0.874408087 |

$^\dagger$In this notation, 5.E+16 = $5.0 \times 10^{16}\,cm$.

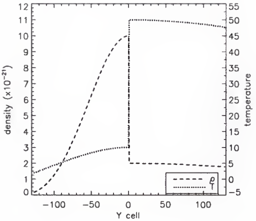

Figure 3.1: Initial density and temperature distributions for SGI model cnsg257e1. The temperature axis has been displaced to better distinguish between the density and temperature.

the potential gradient $d\Phi/dy$ determined for the initial equilibrium distribution. The physical derivative is obtained from the dimensionless derivative via

$$\frac{d\Phi}{dy} = \frac{(n+1)RT_0}{\mu a}\left(\frac{d\theta}{d\xi}\right). \tag{3.24}$$

The gradients are calculated before the simulation begins. In perturbed models, the validity of the gradient values at the top and bottom boundaries decreases as the perturbations grow. However, since the total mass within the grid is held constant by the reflective boundary conditions, the spurious motions induced by not considering the time dependence of the gradient values at the boundaries are very small compared to the motions of interest near the interface. The gravity solver begins to fail only when a perturbation grows large enough to interact directly with the boundaries.

The discussion above explains the methods used to create a state of hydrostatic equilibrium for a self-gravitating gas. As I show later, the equilibria achieved are very good. However, representing a discontinuity on a discrete grid with finite cell sizes cannot be done without introducing some numerical artifacts into the solution. A perfect equilibrium is not attainable; one can only be approximated. Setting up the problem on a computational grid requires careful consideration of whether to place the interface at a cell center or a cell face. CFDLIB uses cell-centered state variables, so the density, temperature, pressure, and velocity terms are initialized at cell centers to begin the simulation. However, face-centered velocity and pressure terms are also used in the computational cycle. Experiments indicate that a better equilibrium is achieved when the interface is placed at a cell face. At an interface of discontinuous density, pressure balance between two perfect gases with the same $\gamma$ and molecular weight is achieved by altering the temperatures so the product of temperature and density remains constant. The different density and temperature values on either side of the grid result in different scale heights, as described by equation (3.22). As a consequence of placing the interface, and hence $\rho_0$ and $T_0$, at a cell face, the maximum cell-centered values in either region are removed from $\rho_0$ and $T_0$ by half a cell. Likewise, the maximum cell-centered pressure is slightly lower than $p_0$ in both regions. Since a configuration of discontinuous density results in a different scale height on either side of the interface, the pressure falls off at different rates in the two regions. As a result, the simulation begins with a slight pressure imbalance at the interface. The more tenuous fluid has a larger scale height, so the cell-centered pressure on that side of the interface is higher than the pressure on the side containing the denser fluid. If the scale heights are increased in both regions, the pressure difference across the interface decreases. A larger scale height also results in smaller gradients for the pressure, density, temperature, and potential, which helps to maintain a stable equilibrium. If the only goal were to create the best equilibrium possible, a very large scale height would be desired. However, a very large scale height is not always obtainable when performing simulations on astrophysical scales. The effects of having relatively short scale heights are examined on static equilibria before considering perturbed cases.

Although an in-depth consideration of the RT instability is not the goal of this study, it is of interest to compare the morphological similarities and differences between the SGI and the RT instability. To provide a better basis for comparisons, RT models are also begun from an initial state of hydrostatic equilibrium. This requires a more careful construction than that in the example of chapter 2. The underlying method is the same as that used for self-gravitating models, but the equations are easier to solve. For a gas that is not self-gravitating, but feels a constant acceleration $g$ (assumed to be positive in the upward direction), the equation of hydrostatic equilibrium is simply

$$\frac{dp}{dy} = g\rho. \tag{3.25}$$

The gravitational acceleration $g$ is determined for each model by setting the RT growth rate (the second term on the right hand side of equation (3.11)) equal to the SGI growth rate (the first term on the right hand side of equation (3.11)) so that for a perturbation wavelength $\lambda$,

$$g = G(\rho_1 - \rho_2)\lambda. \tag{3.26}$$

As a result, SGI and RT models with the same physical parameters at the interface share the same theoretical incompressible growth rate and e-folding time. Again assuming a polytropic equation of state, the equation of hydrostatic equilibrium becomes

$$\rho^{(\gamma-2)} d\rho = \frac{g}{\gamma\kappa} dy. \tag{3.27}$$

Integrating and setting $\rho = \rho_0$ at the interface gives

$$\rho = \rho_0 \left( \frac{(\gamma-1)\mu g}{\gamma R T_0} y + 1 \right)^{\frac{1}{(\gamma-1)}}. \tag{3.28}$$

The temperature distribution is

$$T = \frac{(\gamma-1)\mu g}{\gamma R} y + T_0. \tag{3.29}$$

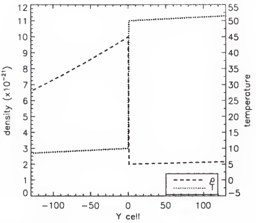

Figure 3.2: Initial density and temperature distributions for RT model cart257e1. The temperature axis has been displaced to better distinguish between the density and temperature.

In the absence of self-gravity, the analytic solution applies to all values of $\gamma$, so no Runge-Kutta solver is needed. The static equilibria are typically more robust for the RT models than for the SGI models. The MUDPACK routines are not used when running RT models, so only the reflective boundary conditions of CFDLIB are applied. Figure (3.2) shows an example of the initial density and temperature distributions for the RT model cart257e1. Other than at the interface, both density and temperature increase in the direction of $\hat{y}$.

## 3.3 Results for Unperturbed Models

For every perturbed model considered, a non-perturbed model was run to test the robustness of the initial equilibrium. The degree to which equilibrium is maintained varies from model to model, with generally good results. In all descriptions that follow, I refer to the denser region below the interface and the more tenuous region above the interface as region 1 and region 2, respectively, with subscripts denoting values at the interface. A key factor is the relative size of the scale height versus the grid size. Equilibrium is better maintained when the scale height of the

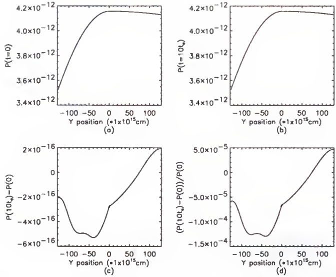

Figure 3.3: Pressure comparison for model cnsg257d0 at $t=0$ and $t=10t_e$. Values are plotted along a constant value of $x$ for a)the pressure distribution at $t=0$; b)the pressure distribution at $t=10t_e$; c)the difference $p(10t_e)-p(0)$; and d)the relative difference $(p(10t_e)-p(0))/p(0)$.

denser fluid $a_1$ is large compared to the spatial extent of the denser region. The scale height is always larger in region 2, so equilibrium is better maintained above the interface than below. The quantity $s_1$ is defined as the ratio of the scale height to the spatial extent in region 1,

$$s_1 = \frac{a_1}{\#\, of\ rows\ in\ region1 \times cell\ size}. \tag{3.30}$$

For example, model cnsg257d0 has a scale height much larger than the spatial extent of region 1, resulting in $s_1=3.2$. After a long time ($t=10t_e$), the maximum $y$-velocity is $0.65\,cm\,s^{-1}$, compared to a sound speed of $24,124\,cm\,s^{-1}$. This is effectively a velocity of zero since the gas cannot traverse a single cell by the end of a simulation. The pressure change over that time is very small. Figure (3.3) shows the pressure along a line of constant $x$ for model cnsg257d0 at $t=0$ and $t=10t_e$. The relative pressure difference is less than 0.02%. Model cnsg257e0 is identical to model cnsg257d0 in every way except that the cell size is five times larger. Because of the larger cell size, the relative size of the scale height compared to the grid size is smaller, $s_1=0.65$.

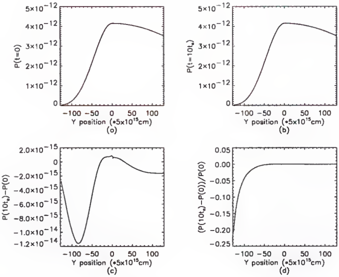

Figure 3.4: Pressure comparison for model cnsg257e0 at $t=0$ and $t=10t_e$.

As a result, the departure from equilibrium is higher. The maximum $y$-velocity at $t = 10t_e$ is $25.1\,cm\,s^{-1}$, and the relative pressure change, shown in figure (3.4), is about 20% at the lower boundary. Although the velocity after $10t_e$ is nearly forty times larger in model cnsg257e0 than in model cnsg257d0, it it still much smaller than the sound speed. This indicates that even when the scale height is small enough to result in very low density and temperature values at the boundaries, the equilibrium is still well maintained. Any departure from equilibrium will not interfere with the growth of induced perturbations at the interface. The requirement that the density and temperature remain positive places an upper limit on the cell size.

RT models do not require a numerical solution for the initial equilibrium or the application of addition boundary conditions for the gravitational potential. As a result, unperturbed RT models maintain better static equilibria. Figure (3.5) shows the pressure along a line of constant $x$ for model cart257d0 at $t=0$ and $t=10t_e$. The pressure difference is several orders of magnitude lower than that shown in figure (3.3) for model cnsg257d0. Likewise, the pressure difference for model cart257e0, shown

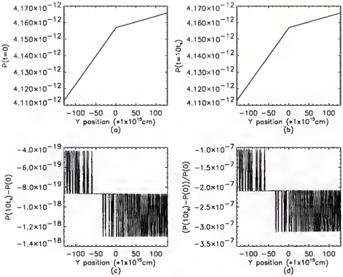

Figure 3.5: Pressure comparison for model cart257d0 at $t=0$ and $t=10t_e$.

in figure (3.6), is several orders of magnitude lower than the pressure difference for model cnsg257e0, shown in figure (3.4).

## 3.4 Results for Perturbed Models

Perturbed models are initiated with a velocity perturbation of the form

$$v(x,y) = v_0 \cos{(k_x x)} e^{|-k_y y|}, \tag{3.31}$$

where $v_0$ is the maximum velocity at the interface. The original set of models (the moderate temperature models) are an exception in that a sine function was used rather than a cosine function. The switch to cosine minimized distortions due to the boundary conditions. The value of $v_0$ is kept small compared to the sound speed in the denser medium ($v_0/c_1 \ll 1$) to approximate incompressible behavior. Unless otherwise noted, $k_y = k_x = k$. A list of parameters for a representative set of models is given in Table (3.2). Although additional models were run, specific remarks are limited to those listed in the table. The perturbation wavelength $\lambda = 2\pi/k$ is always chosen to be less than the Jeans length $\lambda_J$ (see equation 2.38). The ratio $J = \lambda/\lambda_J$ is an important gauge of the overall compressibility of the problem. As $J$ increases,

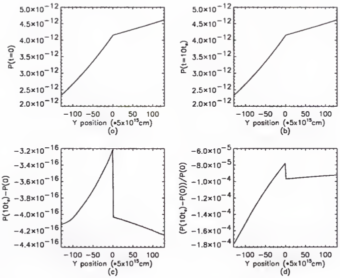

Figure 3.6: Pressure comparison for model cart257e0 at $t=0$ and $t=10t_e$.

the compressibility increases. Because the scale height and the Jeans length vary the same way with density and temperature, a model with a large $J$ value has a small $s$ value. In Table (3.2) only $J$ is listed due to its more significant physical meaning. The theoretical growth rate (equation 3.11) was developed in the incompressible, non-stratified limit, which corresponds to a very low value for $J$. So the models with very low $J$ values come closest to matching the theoretical conditions.

A few words are in order about the convention used in naming the models. The first letter of each name describes the temperature as *m*oderate, *h*ot, or *c*old. The second letter tells whether the initial equilibrium is determined by *a*nalytic or *n*umerical means. The next two letters label the model as either *sg* for SGI or *rt* for RT. Each model is run on a square grid with either *129* or *257* cells in each direction. Models designated with a *d* are low $J$ models, while an *e* designates a high $J$ model. Finally, a number is used to otherwise differentiate among models. Unperturbed models are designated *0*, with perturbed models numbered sequentially higher. Dividing the models according to temperature is a useful way to discuss the SGI under very different conditions. The first set of models are referred to as

Table 3.2: Model Parameters

| model | $\gamma$ | $\rho_1^{\dagger}$ $g\,cm^{-3}$ | $T_1$ $K$ | $\rho_2$ $g\,cm^{-3}$ | $T_2$ $K$ | $v_0/c_1$ | $k_x^{\ddagger}$ $cm^{-1}$ | $k_y$ $cm^{-1}$ | $J_1$ | $\Delta x^{\star}$ $cm$ | $t_e^{+}$ $s$ |
|---|---|---|---|---|---|---|---|---|---|---|---|
| masg129d0 | 2.0 | 2.0 | 131 | 1.0 | 262 | 0.0 | 0.0 | 0.0 | — | 2.0 | 8.458 |
| masg129d1 | 2.0 | 2.0 | 131 | 1.0 | 262 | 0.01 | 9.74 | 9.74 | .0403 | 2.0 | 8.458 |
| masg129d2 | 2.0 | 2.0 | 131 | 1.0 | 262 | 0.01 | 7.31 | 9.74 | .0537 | 2.0 | 8.458 |
| masg129d3 | 2.0 | 2.0 | 131 | 1.0 | 262 | 0.01 | 14.61 | 9.74 | .0269 | 2.0 | 8.458 |
| masg129d4 | 2.0 | 2.0 | 131 | 1.0 | 262 | 0.01 | 19.48 | 9.74 | .0201 | 2.0 | 8.458 |
| hasg129d0 | 2.0 | 2.0 | 1000 | 1.0 | 2000 | 0.0 | 0.0 | 0.0 | — | 2.0 | 8.458 |
| hasg129d1 | 2.0 | 2.0 | 1000 | 1.0 | 2000 | 0.005 | 9.74 | 9.74 | .0146 | 2.0 | 8.458 |
| hasg257d1 | 2.0 | 2.0 | 1000 | 1.0 | 2000 | 0.005 | 9.78 | 9.78 | .0145 | 1.0 | 8.458 |
| hnsg257d0 | 1.4 | 2.0 | 1000 | 1.0 | 2000 | 0.005 | 0.0 | 0.0 | — | 1.0 | 8.458 |
| hnsg257d1 | 1.4 | 2.0 | 1000 | 1.0 | 2000 | 0.005 | 9.78 | 9.78 | .0174 | 1.0 | 8.458 |
| hnsg257d2 | 1.4 | 2.0 | 1000 | 0.4 | 5000 | 0.005 | 9.78 | 9.78 | .0174 | 1.0 | 4.728 |
| hart257d0 | 1.4 | 2.0 | 1000 | 1.0 | 2000 | 0.005 | 0.0 | 0.0 | — | 1.0 | 8.458 |
| hart257d1 | 1.4 | 2.0 | 1000 | 1.0 | 2000 | 0.005 | 9.78 | 9.78 | .0174 | 1.0 | 8.458 |
| hart257d2 | 1.4 | 2.0 | 1000 | 0.4 | 5000 | 0.005 | 9.78 | 9.78 | .0174 | 1.0 | 4.728 |
| cnsg129d0 | 1.4 | 10.0 | 10 | 2.0 | 50 | 0.0 | 0.0 | 0.0 | — | 0.2 | 2.115 |
| cnsg129d1 | 1.4 | 10.0 | 10 | 2.0 | 50 | 0.05 | 97.41 | 97.41 | .0390 | 0.2 | 2.115 |
| cnsg129e0 | 1.4 | 10.0 | 10 | 2.0 | 50 | 0.0 | 0.0 | 0.0 | — | 1.0 | 2.115 |
| cnsg129e1 | 1.4 | 10.0 | 10 | 2.0 | 50 | 0.05 | 9.74 | 9.74 | .390 | 1.0 | 2.115 |
| cnsg129e2 | 1.4 | 10.0 | 10 | 2.0 | 50 | 0.05 | 14.61 | 9.74 | .260 | 1.0 | 2.115 |
| cnsg129e3 | 1.4 | 10.0 | 10 | 2.0 | 50 | 0.05 | 19.48 | 9.74 | .195 | 1.0 | 2.115 |
| cnsg129e4 | 1.4 | 10.0 | 10 | 2.0 | 50 | 0.05 | 24.35 | 9.74 | .156 | 1.0 | 2.115 |
| cnsg257d0 | 1.4 | 10.0 | 10 | 2.0 | 50 | 0.0 | 0.0 | 0.0 | — | 0.1 | 2.115 |
| cnsg257d1 | 1.4 | 10.0 | 10 | 2.0 | 50 | 0.05 | 97.79 | 97.79 | .0388 | 0.1 | 2.115 |
| cnsg257d2 | 1.4 | 10.0 | 10 | 2.0 | 50 | 0.05 | 48.90 | 48.90 | .0776 | 0.1 | 2.115 |
| cnsg257d3 | 1.4 | 10.0 | 10 | 5.0 | 20 | 0.05 | 48.90 | 48.90 | .0776 | 0.1 | 3.783 |
| cnsg257e0 | 1.4 | 10.0 | 10 | 2.0 | 50 | 0.05 | 0.0 | 0.0 | — | 0.5 | 2.115 |
| cnsg257e1 | 1.4 | 10.0 | 10 | 2.0 | 50 | 0.05 | 9.78 | 9.78 | .388 | 0.5 | 2.115 |
| cart257d0 | 1.4 | 10.0 | 10 | 2.0 | 50 | 0.0 | 0.0 | 0.0 | — | 0.1 | 2.115 |
| cart257d1 | 1.4 | 10.0 | 10 | 2.0 | 50 | 0.05 | 97.79 | 97.79 | .0388 | 0.1 | 2.115 |
| cart257d2 | 1.4 | 10.0 | 10 | 2.0 | 50 | 0.05 | 48.90 | 48.90 | .0776 | 0.1 | 2.115 |
| cart257d3 | 1.4 | 10.0 | 10 | 5.0 | 20 | 0.05 | 48.90 | 48.90 | .0776 | 0.1 | 3.783 |
| cart257e0 | 1.4 | 10.0 | 10 | 2.0 | 50 | 0.05 | 0.0 | 0.0 | — | 0.5 | 2.115 |
| cart257e1 | 1.4 | 10.0 | 10 | 2.0 | 50 | 0.05 | 9.78 | 9.78 | .388 | 0.5 | 2.115 |

$^{\dagger}$All density values are $\times 10^{-21}$

$^{\ddagger}$All values of $k$ are $\times 10^{-18}$

$^{\star}$All values of $\Delta x = \Delta y$ are $\times 10^{16}$

$^{+}$All values of $t_e$ are $\times 10^{13}$

moderate temperature models. Many of these models were run in the testing phase of the code, but little analysis was performed. The bulk of the science was accomplished with high and low temperature models. Because the scale height and Jeans length scale as $T^{1/2}$, hot models generally have high $s$ and low $J$ values. Cold models have smaller $s$ and larger $J$ values. The hot models come closer to approximating the incompressible, non-stratified conditions under which the theoretical growth rates hold. The cold models are more representative of the conditions in cold molecular clouds.

### 3.4.1 Moderate Temperature Models

The first set of models is of moderate temperature ($T_1 = 131\,K$) and uses the analytic $\gamma = 2$ solution for the initial equilibrium. All moderate temperature models have low $J$ values and a density ratio of 2. They primarily were used for testing the procedure for establishing the initial hydrostatic equilibrium. An example is model masg129d1, the evolution of which is shown in figure (3.7). As previously noted, model masg129d1 was perturbed using a sine function with amplitude $.01c_1$ ($c_1 = 104,294\,cm\,s^{-1}$). Asymmetries arise early in the simulation due to boundary effects. Because of the asymmetries, little analysis was done on the moderate temperature models. Even so, model masg129d1 clearly shows one large difference between the SGI and the RT instability. Whereas the RT instability is characterized by dense columns of material moving into and displacing the tenuous material, the SGI does the opposite. The SGI gives rise to tenuous columns moving into the denser material. This trait is common to all SGI models.

According to HWL, the SGI growth rate for incompressible fluids does not depend upon the perturbation wavelength. To test the validity of this claim, a series of simulations was performed in which only the value of $k_x$ was altered. A sample of the results is shown in figure (3.8). The value of $k_y$ was kept constant amongst

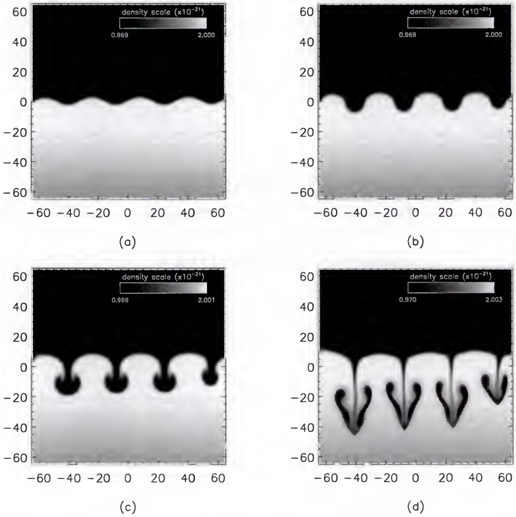

Figure 3.7: Evolution of the SGI for model masg129d1. Filled contours show the density distribution at a)$1t_e$; b)$2t_e$; c)$3t_e$; and d)$4t_e$. The e-folding time is $t_e = 8.458 \times 10^{13}\,s$. The cell size $\Delta x = \Delta y = 2.0 \times 10^{16} cm$.

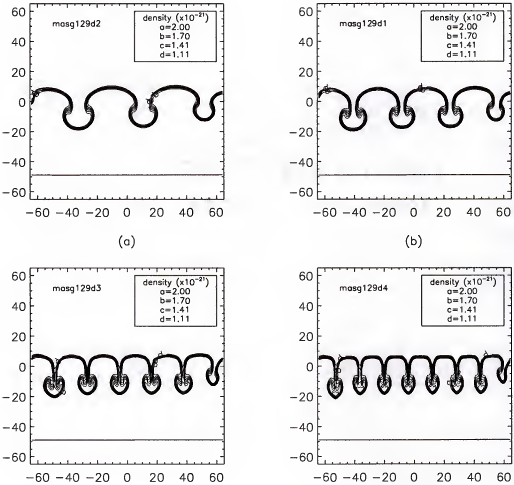

(a)

(b)

(c)

(d)

Figure 3.8: Comparison of moderate temperature models with varying $k_x$. The panels show the density contours at $t = 3t_e$ for models a)masg129d2; b)masg129d1; c)masg129d3; and d)masg129d4. The SGI grows at the same rate in all four simulations. All four models share the same e-folding time, $t_e = 8.458 \times 10^{13}\,s$, and cell size, $\Delta x = \Delta y = 2.0 \times 10^{16} cm$.

the models to keep the velocity perturbations as similar as possible. The prediction holds up very well.

### 3.4.2 High Temperature Models

High temperature models provide the best comparison between the computational and theoretical results due to their low $J$ values. These models are characterized by temperature $T_1 = 1000\,K$ and density $\rho_1 = 2\times10^{-21} g\,cm^{-3}$. The corresponding values of $T_2$ and $\rho_2$ depend upon the density contrast at the interface. Two cases are considered in detail, $\rho_1/\rho_2 = 2$ and $\rho_1/\rho_2 = 5$. The sound speed in the denser medium for models with $\gamma = 2$ is $c_1 = 288,340\,cm\,s^{-1}$.

For the $\rho_1/\rho_2 = 2$ case, comparison is made to the moderate temperature model masg129d1. Figure (3.9) shows the evolution of model hasg129d1. The only differences from model masg129d1 are the temperature, the perturbation amplitude, and the use of a cosine in the perturbation function. Once again, the analytic $\gamma = 2$ solution is used in the initialization. The new perturbation function does far better at preserving the symmetry across the grid. Otherwise, the SGI morphology and growth rate are very similar. The symmetry of model hasg129d1 helps to see that the initial perturbation wavelength is preserved well into the nonlinear regime, a trait the SGI shares with the RT instability.

When running any sort of computer simulation, it is necessary to explore the effects of the finite grid resolution. Model hasg129d1 was duplicated on a larger grid to produce model hasg257d1. The result is displayed in figure (3.10). The cell size for model hasg257d1 is one-half the cell size for model hasg129d1, so the physical spatial extent is about the same. The SGI grows at very nearly the same rate in both. However, the higher resolution model clearly shows fine structures not seen at lower resolution. This leads to the conclusion that although low resolution is sufficient for determining the growth rate to a good level of accuracy, a higher resolution is

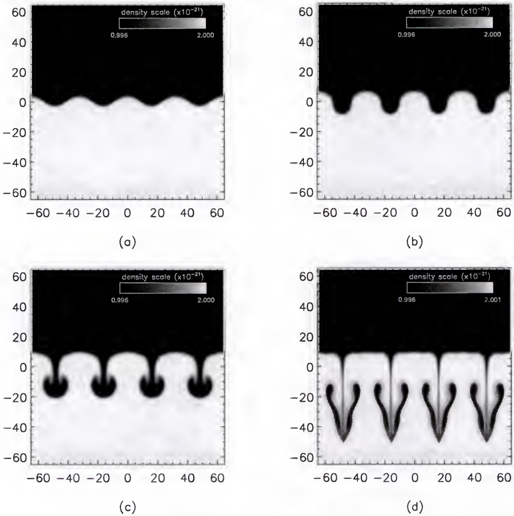

Figure 3.9: Evolution of the SGI for model hasg129d1. Filled contours show the density distribution at a)$1t_e$; b)$2t_e$; c)$3t_e$; and d)$4t_e$. The e-folding time is $t_e = 8.458 \times 10^{13}\,s$. The cell size $\Delta x = \Delta y = 2.0 \times 10^{16} cm$.

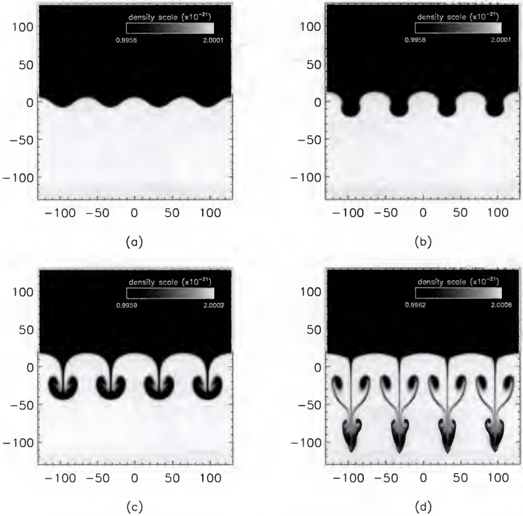

(a)
(b)
(c)
(d)

Figure 3.10: Evolution of the SGI for model hasg257d1. This model is a high resolution version of model hasg129d1. Filled contours show the density distribution at a)$1t_e$; b)$2t_e$; c)$3t_e$; and d)$4t_e$. The e-folding time is $t_e = 8.458 \times 10^{13}\, s$. The cell size $\Delta x = \Delta y = 1.0 \times 10^{16} cm$.

needed to examine the nonlinear morphology. I restrict the bulk of my analysis to the consideration of high resolution models.

In order to measure the experimental growth rate of the SGI, I trace the velocity growth inside one of the tenuous columns. For each model, I plot $ln[v(t)/v(t_0)]$ versus the time in units of the theoretical e-folding time. The slope of the best-fit line corresponds to the growth rate. The choice of $t_0$ is arbitrary since any change alters the line's intercept but not its slope. I typically use $t_0 = 1t_e$. Of more consequence is the choice of which data points to include in the least squares calculation that determines the best-fit line. For some models the data are such that the inclusion or exclusion of a few points can change the slope of the line by as much as ten percent. When possible, the same time range is used for determining the growth rates for models that are to be compared to one another. Figure (3.11) shows the result for model hasg257d1. Multiple modes are excited by the perturbation, initially causing the velocity to fall due to the presence of small amplitude sound waves. Once the excited SGI mode begins to dominate the motion, a linear relationship is clearly seen. An early stage of exponential growth is another trait shared between the SGI and the RT instability. An experimental result in perfect agreement with theory would produce a slope of unity. For model hasg257d1 the growth rate is $\omega = 1.028t_e^{-1}$, very close to the theoretical prediction.

Up to this point, all models have used the $\gamma = 2$ analytic formulae to create the initial static equilibrium. From here on, models with $\gamma = 1.4$ are considered. The numerical (Runge-Kutta) solver is used to establish the initial equilibrium. Model hnsg257d1 is a $\gamma = 1.4$ model which corresponds to model hasg257d1. The lower $\gamma$ results in a lower sound speed ($c_1 = 241,242\, cm\, s^{-1}$), which translates into a lower perturbation amplitude and a higher $J$ value. Otherwise, models hnsg257d1 and hasg257d1 are identical. As shown in figure (3.12), the SGI development is the same as that for model hasg257d1. Figure (3.13) shows model hnsg257d1 at a later time

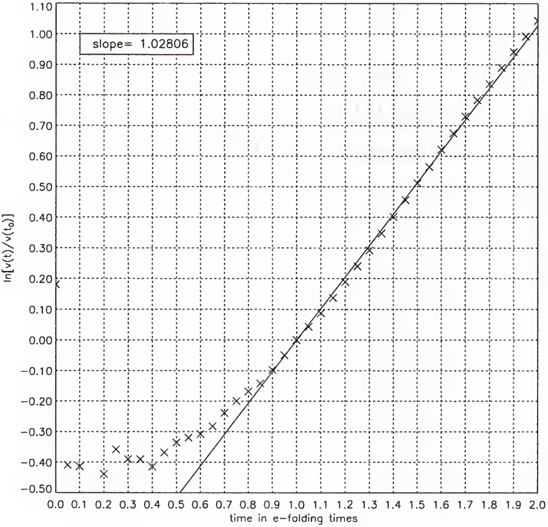

Figure 3.11: Velocity growth for model hasg257d1. Data points are normalized to the velocity value at $t_0 = 1.0t_e$. The best-fit line using data points from $0.80t_e$ to $1.80t_e$ yields a growth rate of $1.028t_e^{-1}$. The e-folding time is $t_e = 8.458 \times 10^{13}\, s$.

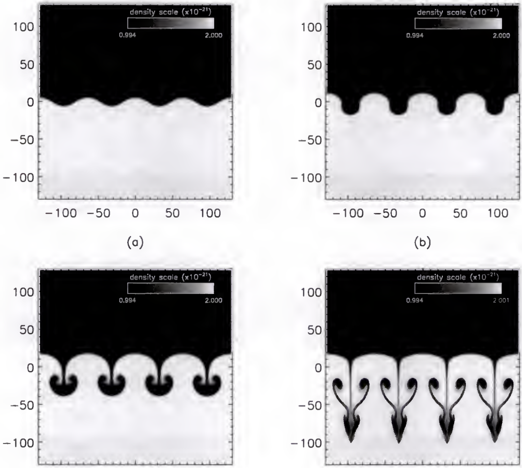

(a)

(b)

(c)

(d)

Figure 3.12: Evolution of the SGI for model hnsg257d1. Filled contours show the density distribution at a)$1t_e$; b)$2t_e$; c)$3t_e$; and d)$4t_e$. The e-folding time is $t_e = 8.458 \times 10^{13}\,s$. The cell size $\Delta x = \Delta y = 1.0 \times 10^{16} cm$.

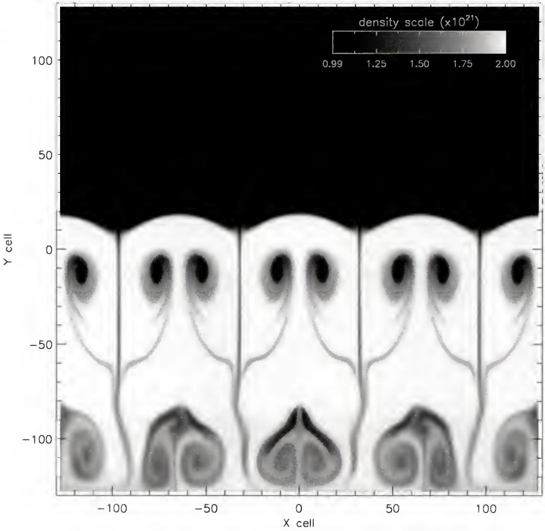

Figure 3.13: Model hnsg257d1 at $t = 5t_e$. The SGI has evolved to form islands of tenuous gas embedded in the denser gas.

of $t = 5t_e$. The structures seen near the bottom of the grid are due to the reflective boundary condition, and hence are unphysical. Closer to the interface, islands of tenuous gas are seen embedded in the denser material. The interface has moved very little into the tenuous fluid, but the wide dense bubbles displace a lot of tenuous fluid. As in the $\gamma = 2$ case, the experimental growth rate of a tenuous column in model hnsg257d1 agrees with the theoretical growth rate. Figure (3.14) shows the velocity growth for model hnsg257d1. The calculated slope gives a growth rate of $\omega = 1.031 t_e^{-1}$. Switching from $\gamma = 2$ to $\gamma = 1.4$ has a minimal effect on the growth of the SGI.

Since the SGI and the RT instability are both density interface instabilities, it is instructive to compare and contrast the two. Model hart257d1 is an RT model with the same interfacial densities and temperatures and the same grid parameters as model hnsg257d1. From equation (3.26), the value of $g$ which gives the same theoretical growth rate as that for model hnsg257d1 is $g = 4.288 \times 10^{-11} cm\, s^{-2}$. The morphology of model hart257d1 is shown in figure (3.15). In the early stage of development, the SGI and the RT instability appear quite similar. Both preserve the perturbation wavelength well into the nonlinear regime. However, at late times the SGI and the RT instability appear very different. As expected for the RT instability, widely spaced columns of dense gas stream into the more tenuous medium. (The characteristic mushroom cap structure arises due to a secondary Kelvin-Helmholtz instability.) In contrast, the SGI gives rise to very thin fingers of tenuous gas moving into the denser region. The separation between dense columns decreases as the SGI evolves. The growth rates for RT models are determined with the same ln-linear plotting method used for the SGI cases. However, for RT models an upward moving dense column is used. The growth rate for model hart257d1 (figure 3.16) is $\omega = 0.580 t_e^{-1}$. This result is surprisingly low considering how well the experimental growth rate matches the theoretical growth rate for the SGI models so far considered.

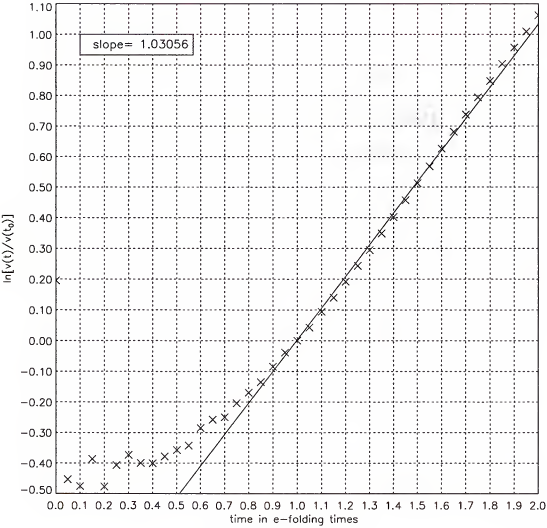

Figure 3.14: Velocity growth for model hnsg257d1. Data points are normalized to the velocity value at $t_0 = 1.0t_e$. The best-fit line using data points from $0.80t_e$ to $1.80t_e$ yields a growth rate of $1.031t_e^{-1}$. The e-folding time is $t_e = 8.458 \times 10^{13}\,s$.

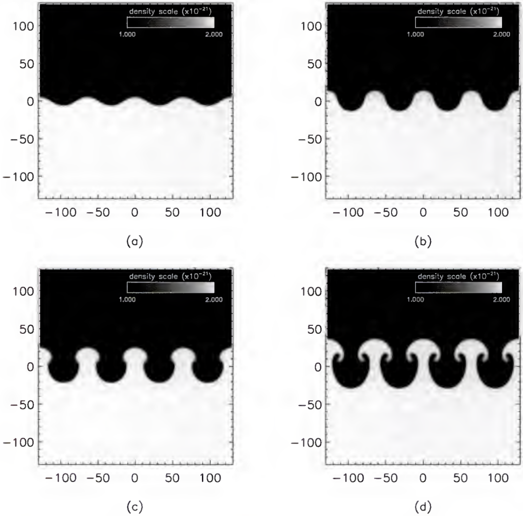

Figure 3.15: Evolution of the RT instability for model hart257d1. Filled contours show the density distribution at a)$1t_e$; b)$2t_e$; c)$3t_e$; and d)$4t_e$. The e-folding time is $t_e = 8.458 \times 10^{13}\,s$. The cell size $\Delta x = \Delta y = 1.0 \times 10^{16} cm$.

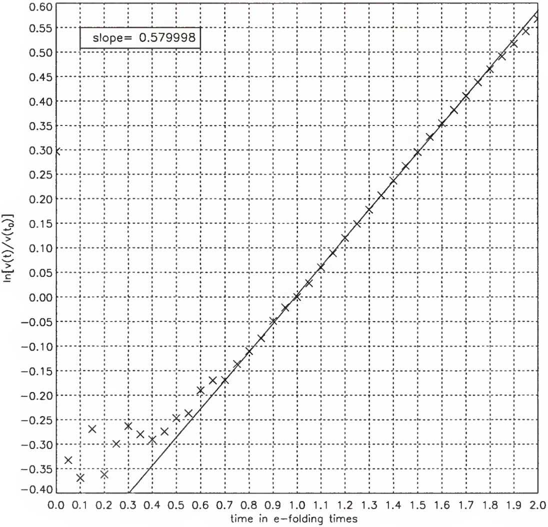

Figure 3.16: Velocity growth for RT model hart257d1. Data points are normalized to the velocity value at $t_0 = 1.0t_e$. The best-fit line using data points from $0.80t_e$ to $1.80t_e$ yields a growth rate of $0.580t_e^{-1}$. The e-folding time is $t_e = 8.458 \times 10^{13}\, s$.

Models for both types of instabilities deviate from the theoretical assumptions of incompressibility and non-stratification. The lower than expected RT growth rate may be attributable to the use of 2-D simulations to model a 3-D phenomenon. Calder et al. (2000) have demonstrated that RT simulations performed with 3-D perturbations produce significantly higher growth rates than those with 2-D perturbations. Three dimensional simulations of the SGI are needed to verify that the same is not true in the self-gravitating case.

According to equation (3.11), a higher density contrast at the interface results in a faster growth rate for both the SGI and the RT instability. Models hnsg257d2 and hart257d2 are high temperature models with $\rho_1/\rho_2 = 5$. Region 1 remains unchanged from models hnsg257d1 and hart257d1, but region 2 is assigned the interfacial values $\rho_2 = 4 \times 10^{-22} g\, cm^{-3}$ and $T_2 = 5000\, K$. The perturbation velocity and $J$ value are defined using values in region 1, and hence remain unchanged. The higher density contrast results in a shorter theoretical e-folding time, $t_e = 4.728 \times 10^{13} s$. Figures (3.17) and (3.18) show the growth of the instabilities for model hnsg257d2 and model hart257d2, respectively. Note that the panels show the density distribution at different times than in the previous figures. The larger density contrast at the interface results in a larger momentum difference, so penetration by the tenuous fingers into the denser medium is impeded early in the simulation. Compared to the $\rho_1/\rho_2 = 2$ models, both the SGI and the RT instability grow faster in terms of absolute time. In terms of the theoretical e-folding time, the SGI growth is slower. The growth rates for the SGI and RT models are far more similar than in the previous case. The velocity growth for model hnsg257d2 (figure 3.19) yields a growth rate of $\omega = 0.735 t_e^{-1}$. The velocity growth for model hart257d2 (figure 3.20) yields a growth rate of $\omega = 0.720 t_e^{-1}$. Both models have growth rates lower than the theoretical prediction.

The density ratio of 5 was chosen because it produces an e-folding time comparable to the free-fall time of the denser medium. A sphere with the density and

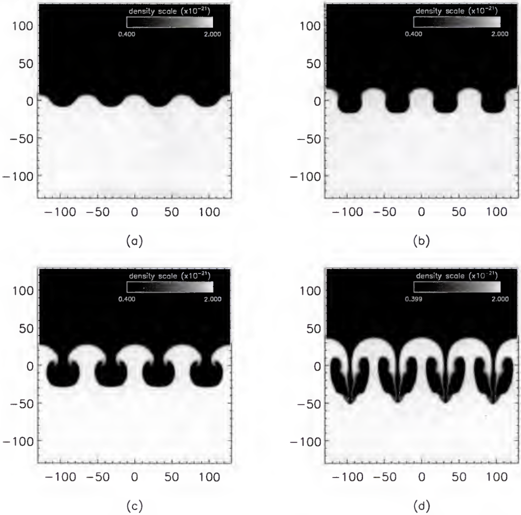

Figure 3.17: Evolution of the SGI for model hnsg257d2. Filled contours show the density distribution at a)$2t_e$; b)$3t_e$; c)$4t_e$; and d)$5t_e$. The e-folding time is $t_e = 4.728 \times 10^{13}\,s$. The cell size $\Delta x = \Delta y = 1.0 \times 10^{16} cm$.

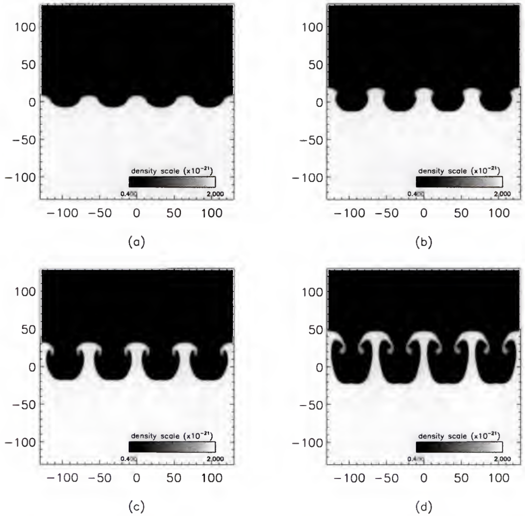

Figure 3.18: Evolution of the RT instability for model hart257d2. Filled contours show the density distribution at a)$2t_e$; b)$3t_e$; c)$4t_e$; and d)$5t_e$. The e-folding time is $t_e = 4.728 \times 10^{13}\,s$. The cell size $\Delta x = \Delta y = 1.0 \times 10^{16} cm$.

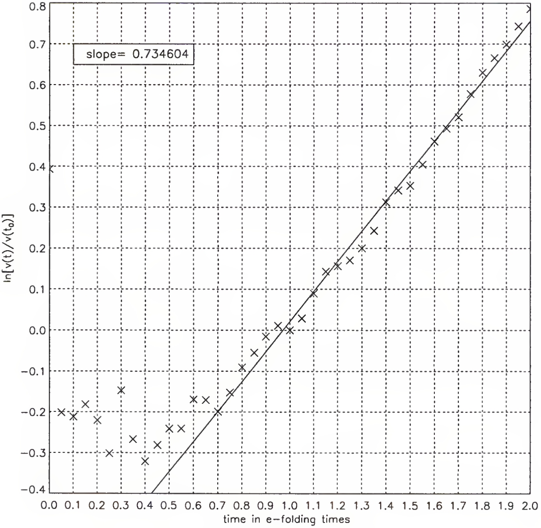

Figure 3.19: Velocity growth for SGI model hnsg257d2. Data points are normalized to the velocity value at $t_0 = 1.0t_e$. The best-fit line using data points from $0.70t_e$ to $2.00t_e$ yields a growth rate of $0.735t_e^{-1}$. The e-folding time is $t_e = 4.728 \times 10^{13}\, s$.

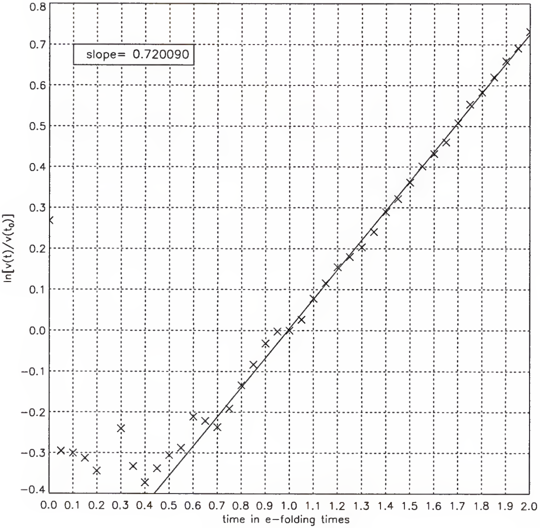

Figure 3.20: Velocity growth for RT model hart257d2. Data points are normalized to the velocity value at $t_0 = 1.0t_e$. The best-fit line using data points from $0.70t_e$ to $2.00t_e$ yields a growth rate of $0.720t_e^{-1}$. The e-folding time is $t_e = 4.728 \times 10^{13}\ s$.

temperature of region 1 in the high temperature models has a free-fall time (equation 2.41) of $t_{ff} = 4.697 \times 10^{13} s$. In the ISM, density contrasts at the boundaries of clouds and filaments are typically far greater than 5. In these regions, the SGI can grow on time-scales far shorter than the free-fall time.

### 3.4.3 Low Temperature Models

The low temperature models have density and temperature values appropriate for cold molecular clouds, $\rho_1 = 10^{-20} g\, cm^{-3}$ and $T_1 = 10\, K$. The higher density and lower temperature result in lower values for the scale height and Jeans length than in the hot models. Therefore, if given the same perturbation wavelength as the hot models, the cold models have higher $J$ values. Whereas the hot models have a $J$ value of 0.0174, some of the cold models have $J$ values as high as 0.388. As a result, the cold models begin with a more stratified density distribution and are more likely to undergo compression. The sound speed is lower for the cold models ($c_1 = 24,124\, cm\, s^{-1}$) so a larger fraction of the sound speed $v_0/c_1 = 0.05$ is used as the velocity perturbation amplitude. A greater departure from the incompressible, non-stratified theoretical growth rate is expected.

The first set of cold models has a density ratio of 5 and a high $J$ value. The models with the highest $J$ value ($J = 0.388$) are the SGI model cnsg257e1 and the RT model cart257e1. As the most stratified models, they begin with a larger departure from static equilibrium than any other model. Even so, the motions induced by the departure from equilibrium are not large enough to affect the instability growth at the interface. The theoretical e-folding time for these models is $t_e = 2.115 \times 10^{13} s$. The growth rate is higher than in previous cases due to the higher background density. The evolution of model cnsg257e1 is shown in figure (3.21). Only two full cosine waves are excited. As previously seen, the tenuous gas streams into the denser gas through narrow channels, leaving wide, dense columns behind. By $6t_e$ the tenuous columns have hit the bottom boundary of the grid. The RT model cart257e1 is

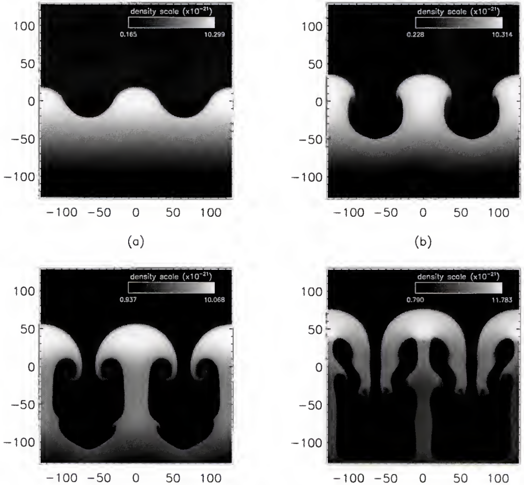

(a) (b) (c) (d)

Figure 3.21: Evolution of the SGI for model cnsg257e1. Filled contours show the density distribution at a)$3t_e$; b)$4t_e$; c)$5t_e$; and d)$6t_e$. Note the resemblance to the RT model cart257e1 at late times. The e-folding time is $t_e = 2.115 \times 10^{13}\,s$. The cell size $\Delta x = \Delta y = 0.5 \times 10^{16} cm$.

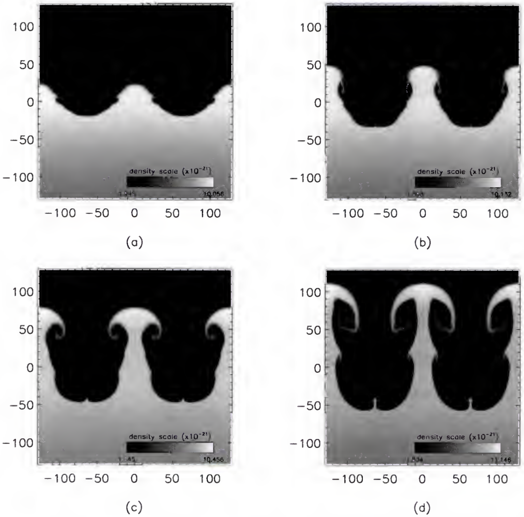

Figure 3.22: Evolution of the RT instability for model cart257e1. Filled contours show the density distribution at a)$3t_e$; b)$4t_e$; c)$5t_e$; and d)$6t_e$. Note the resemblance to the SGI model cnsg257e1 at late times. The e-folding time is $t_e = 2.115 \times 10^{13}\,s$. The cell size $\Delta x = \Delta y = 0.5 \times 10^{16} cm$.

shown in figure (3.22). As expected, more compression is seen in the cold SGI and RT models than in the hot models. As in other RT models, the dominant features in model cart257e1 are dense columns pushing up and displacing the tenuous fluid. Note the striking similarities between the morphologies of models cnsg257e1 and cart257e1. Although the dynamic processes are different and the instabilities grow in different ways, both give rise to dense columns of comparable size and width. In both cases, the height of the dense columns after $6t_e$ is roughly 170 cells or $8.5 \times 10^{17} cm = 0.275\, pc$. The largest difference is the size of the mushroom cap at the head of each dense column. Whichever fluid moves fastest, the tenuous for SGI and the dense for RT, forms narrower columns and smaller caps than the slower moving fluid. As in the high temperature models with $\rho_1/\rho_2 = 5$, the growth rates for models cnsg257e1 and cart257e1 are in close agreement. The velocity growth for model cnsg257e1 (figure 3.23) yields a growth rate of $\omega = 0.852 t_e^{-1}$. The velocity growth for model cart257e1 (figure 3.24) yields a growth rate of $\omega = 0.836 t_e^{-1}$. Unexpectedly, the experimental growth rate for this highly stratified RT model shows better agreement with the non-stratified theoretical prediction than the growth rates for the high temperature RT models.

The prediction that the SGI growth rate is independent from the perturbation wavelength was put through another test with low temperature models. Lower resolution models were excited with 2, 3, 4, and 5 waves. The wave numbers and $J$ values varied accordingly. The result is shown in figure (3.25). As in the moderate temperature version, $k_y$ remained constant amongst the models while $k_x$ changed. The models with the longer perturbation wavelengths have slightly higher growth rates, not a surprising result considering the range of $J$ values represented.

Additional simulations were performed using low temperature models with a density ratio of 5 to explore the effects of varying the $J$ value. The physical parameters are unaltered, but a smaller cell size is used. For example, model cnsg257d2 has

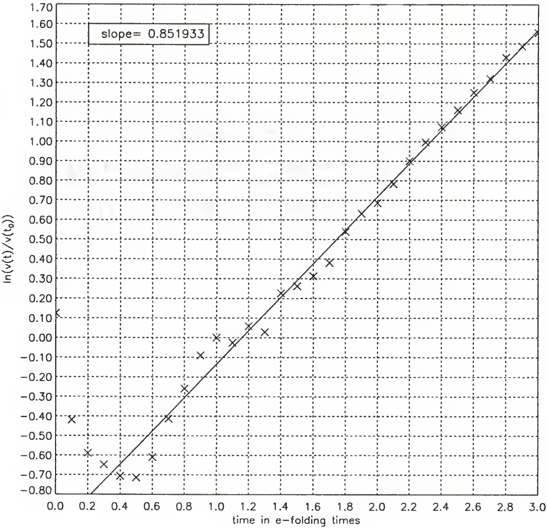

Figure 3.23: Velocity growth for SGI model cnsg257e1. Data points are normalized to the velocity value at $t_0 = 1.0t_e$. The best-fit line using data points from $1.0t_e$ to $3.0t_e$ yields a growth rate of $0.852t_e^{-1}$. The e-folding time is $t_e = 2.115 \times 10^{13}\,s$.

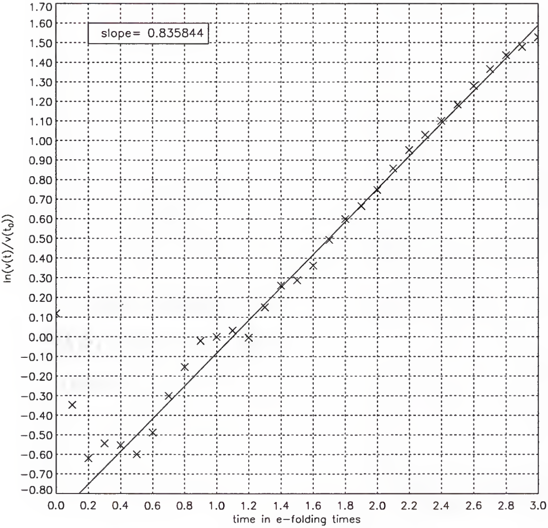

Figure 3.24: Velocity growth for RT model cart257e1. Data points are normalized to the velocity value at $t_0 = 1.0t_e$. The best-fit line using data points from $1.0t_e$ to $3.0t_e$ yields a growth rate of $0.836t_e^{-1}$. The e-folding time is $t_e = 2.115 \times 10^{13}\,s$.

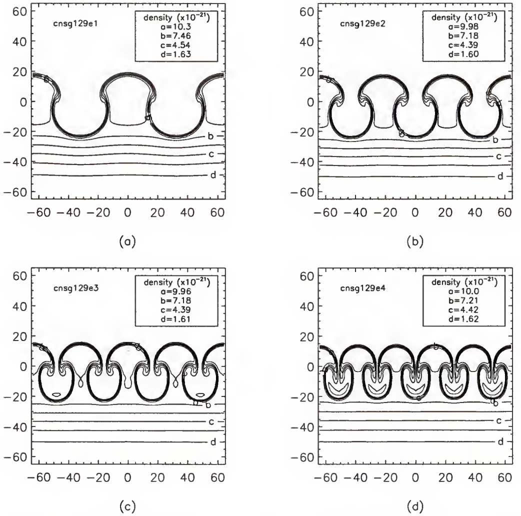

(a) (b) (c) (d)

Figure 3.25: Comparison of cold SGI models with varying $k_x$. The panels show the density contours at $t = 4t_e$ for models a)cnsg129e1; b)cnsg129e2; c)cnsg129e3; and d)cnsg129e4. Longer wavelength models show a slightly larger growth rate. The e-folding time is $t_e = 2.115 \times 10^{13}\, s$ for all four models. The cell size $\Delta x = \Delta y = 1.0 \times 10^{16} cm$.

a cell size one-fifth as large as the cell size in model cnsg257e1. The perturbation wavelength and $J$ value ($J = 0.0776$) are also one-fifth as large. The result is shown in figure (3.26). The same velocity perturbation is used for models cnsg257d2 and cnsg257e1. The fluid travels across the grid in less time due to the smaller cell size. After a time of $3.5t_e$, the dense columns are about 140 cells tall, which is a physical distance of only $1.4 \times 10^{17} cm = 0.0454 pc$. By $4.5t_e$ the tenuous fingers have rebounded from the bottom boundary of the grid. For the velocities used, the physical extent of the grid is not large enough to follow the SGI growth for very long. Considering this restriction, model cnsg257d2 does a fair job of reproducing the interfacial region of model cnsg257e1. The growth rate for model cnsg257d2 (figure 3.27) is $\omega = 0.787 t_e^{-1}$, a value close to that for model cnsg257e1. (The velocity growth in model cnsg257d2 does not result in a clearly defined best-fit line on the ln-linear growth plot. The experimental value of the growth rate is more uncertain than that of model cnsg257e1.) Despite the differences in cell size and $J$ value, models cnsg257e1 and cnsg257d2 produce comparable results. Contrary to expectations, a larger degree of stratification does not result in a greater deviation from the theoretical growth rate.

In the low temperature, high $J$ regime (models cnsg257e1 and cart257e1), the SGI and the RT instability resulted in very similar morphologies and growth rates. Such a similarity is not readily seen in the low temperature, low $J$ models. The low $J$ model cart257d2 is shown in figure (3.28). The dense columns in model cart257d2 are of comparable height to those in model cnsg257d2 throughout most of the simulation. However, there is a greater discrepancy in the size of the mushroom caps. The constant acceleration $g$ in model cart257d2 is one-fifth that in model cart257e1. The two cold RT models show very similar structures, but the growth rates are quite different. The velocity growth for model cart257d2 (figure 3.29) yields a growth rate $\omega = 0.465 t_e$, much lower than the growth rate for model cart257e1.

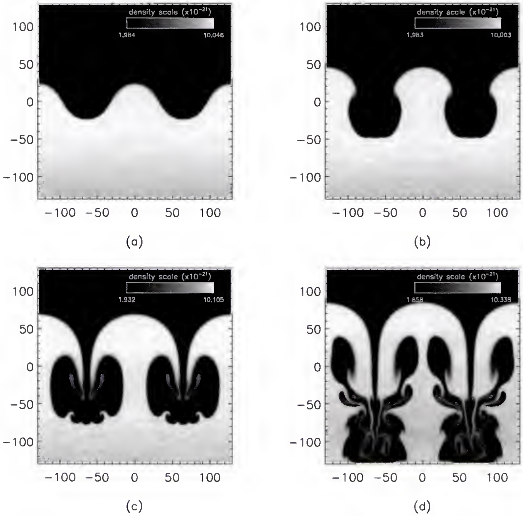

(a)

(b)

(c)

(d)

Figure 3.26: Evolution of the SGI for model cnsg257d2. Filled contours show the density distribution at a)$1.5t_e$; b)$2.5t_e$; c)$3.5t_e$; and d)$4.5t_e$. The e-folding time is $t_e = 2.115 \times 10^{13}\,s$. The cell size $\Delta x = \Delta y = 0.1 \times 10^{16} cm$.

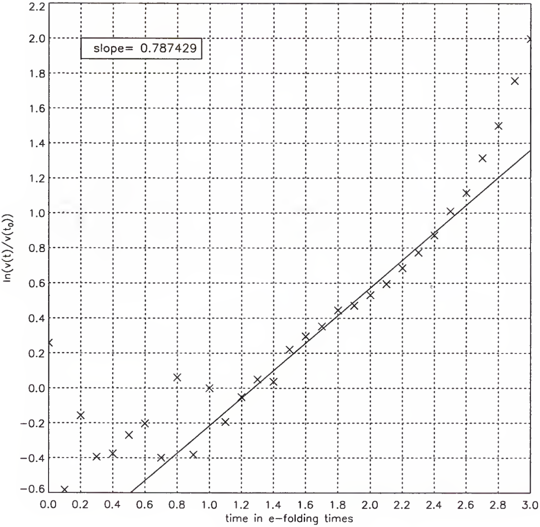

Figure 3.27: Velocity growth for SGI model cnsg257d2. Data points are normalized to the velocity value at $t_0 = 1.0t_e$. The best-fit line using data points from $1.2t_e$ to $2.6t_e$ yields a growth rate of $0.787t_e^{-1}$. The e-folding time is $t_e = 2.115 \times 10^{13}\,s$.

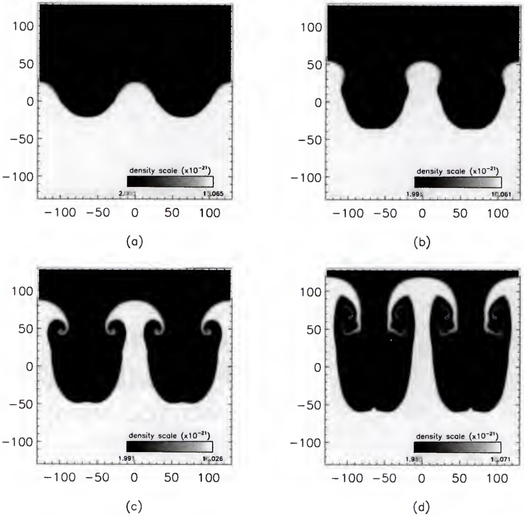

Figure 3.28: Evolution of the RT instability for model cart257d2. Filled contours show the density distribution at a)$1.5t_e$; b)$2.5t_e$; c)$3.5t_e$; and d)$4.5t_e$. The e-folding time is $t_e = 2.115 \times 10^{13}\,s$. The cell size $\Delta x = \Delta y = 0.1 \times 10^{16} cm$.

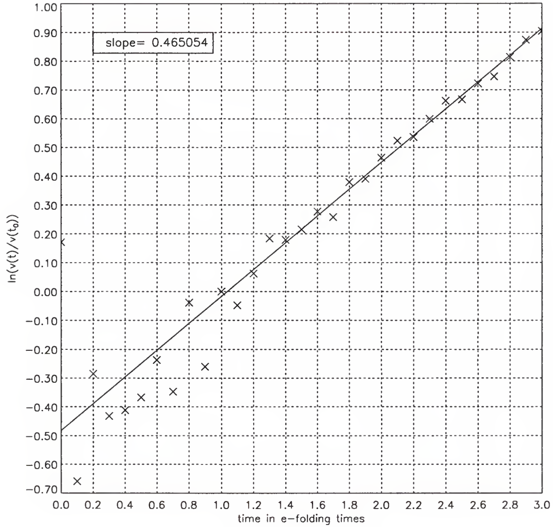

Figure 3.29: Velocity growth for RT model cart257d2. Data points are normalized to the velocity value at $t_0 = 1.0t_e$. The best-fit line using data points from $1.0t_e$ to $3.0t_e$ yields a growth rate of $0.465t_e^{-1}$. The e-folding time is $t_e = 2.115 \times 10^{13}\,s$.

Model cart257d2 resembles the high temperature $\rho_1/\rho_2=2$ models in that its growth rate is lower than the corresponding SGI model cnsg257d2.

The low temperature, low $J$ models were also performed with a perturbation that excited four full cosine waves. Comparison with the previous set of models provides some idea of how the spacing of the peaks on the grid affects the evolution of the instabilities. The SGI model cnsg257d1, shown in figure (3.30), is similar to model cnsg257d2, except that the values of $k_x$ and $k_y$ are twice as big. In addition to reducing $J$ by one-half, the increase in $k$ results in a steeper exponential falloff in velocity away from the interface, so the initial perturbation amplitude is less. This difference notwithstanding, the morphologies are not very different until late in the evolution. By $4t_e$, model cnsg257d1 shows signs of asymmetries in the tenuous columns. The fingers of gas have begun interacting. The cell size is too small to fit four non-interacting waves across the grid. When only two waves are perturbed, the columns are separated by a sufficient distance so that interaction between them is delayed. The growth rate for model cnsg257d1 (figure 3.31) is a bit problematic to calculate due to the interaction of the gas streams. Limiting the slope calculation to data points between $1t_e$ and $2t_e$ results in a growth rate of $\omega=0.620t_e$, a value lower than that for model cnsg257d2.

The RT model cart257d1 with four excited waves compares to model cart257d2 in very much the same way. Because the RT growth rate depends upon the perturbation wavelength, a smaller value of $g$ was used for model cart257d1. Figures (3.32) and (3.33) show the morphology and velocity growth, respectively, for model cart257d1. The morphologies of model cart257d1 and cart257d2 are similar, but the growth rate for model cart257d1 is slightly smaller than that for model cart257d2. Unlike the SGI model, no interaction between the growing dense columns is seen in model cart257d1. The reason is partly due to the smaller growth rate for model cart257d1, compared to that for model cnsg257d1, and partly due to the lack of self-gravity induced motion

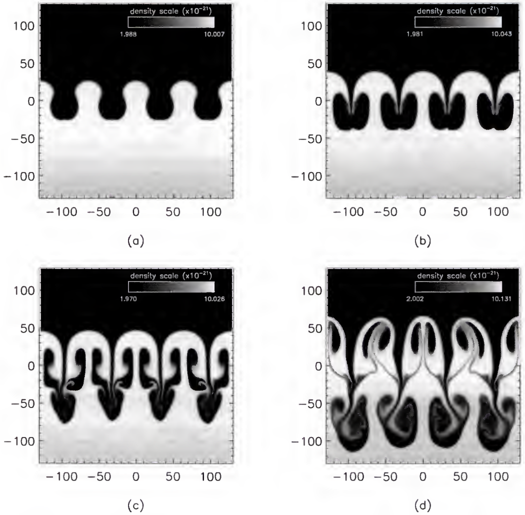

Figure 3.30: Evolution of the SGI for model cnsg257d1. Filled contours show the density distribution at a)$2t_e$; b)$3t_e$; c)$4t_e$; and d)$5t_e$. The e-folding time is $t_e = 2.115 \times 10^{13}\,s$. The cell size $\Delta x = \Delta y = 0.1 \times 10^{16} cm$.

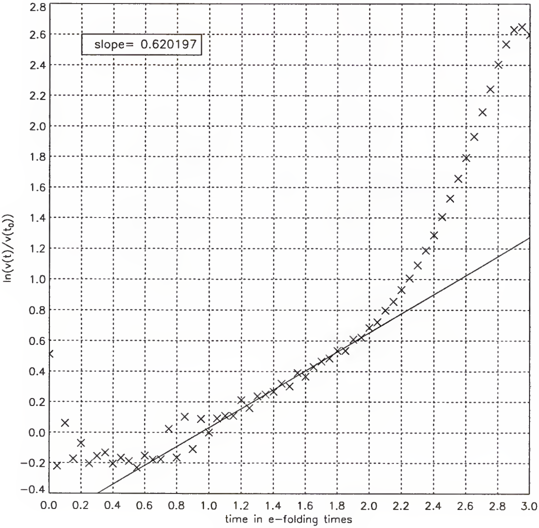

Figure 3.31: Velocity growth for SGI model cnsg257d1. Data points are normalized to the velocity value at $t_0 = 1.0t_e$. The best-fit line using data points from $1.0t_e$ to $2.0t_e$ yields a growth rate of $0.620t_e^{-1}$. The e-folding time is $t_e = 2.115 \times 10^{13}\,s$.

in the $x$ direction. For both the SGI and RT models considered, altering the number of perturbed waves across the grid has little effect, provided the spacing is large enough (and $v_x$ small enough) to prevent interaction between the columns. Having fewer waves on the grid means more cells make up the width of each column and cap, which allows more detailed structures to be seen.

All of the low temperature models so far mentioned have a density ratio of 5 at the interface. Model cnsg257d3 has a density ratio of 2 at the interface, resulting in a longer e-folding time. The growth of the SGI is shown in figure (3.34). The lower momentum contrast at the interface allows the SGI to grow sooner relative to the e-folding time than when $\rho_1/\rho_2 = 5$. The tenuous gas streams strike the bottom of the grid rather quickly. The structure seen in model cnsg257d3 resembles that in the high temperature models with $\rho_1/\rho_2 = 2$. The tenuous fingers become narrower as the simulation progresses. The structure at later times is very interesting. Figure (3.35) shows model cnsg257d3 at a time of $5t_e$. Secondary instabilities have formed both on the dense columns and between them. The growth rate for this model (figure 3.36) is $\omega = 0.882$, which is closer to the theoretical prediction than any other low temperature model. However, the growth rate for the corresponding RT model cart257d3 (not shown) is again unexpectedly low at $\omega = 0.306$. The hot and cold $\rho_1/\rho_2 = 2$ models agree with one another fairly well. The hot models were not run long enough to see any structures akin to figure (3.35), but this does not preclude the possibility such morphologies do arise at late times. The morphology of model cnsg257d3 at $t = 3.5t_e$ is not very different from the morphology of model hnsg257d1 at $t = 5.0t_e$ (figure 3.13). The largest difference between the hot and cold models is the time-scale on which they grow, but the difference in e-folding time is due to the change in density, not the change in temperature.

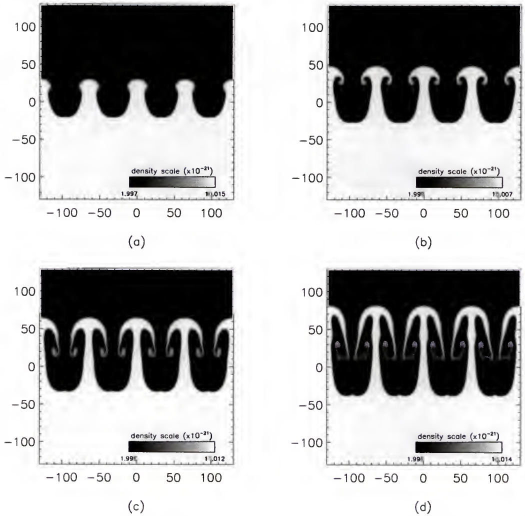

Figure 3.32: Evolution of the RT instability for model cart257d1. Filled contours show the density distribution at a)$2t_e$; b)$3t_e$; c)$4t_e$; and d)$5t_e$. The e-folding time is $t_e = 2.115 \times 10^{13}\,s$. The cell size $\Delta x = \Delta y = 0.1 \times 10^{16} cm$.

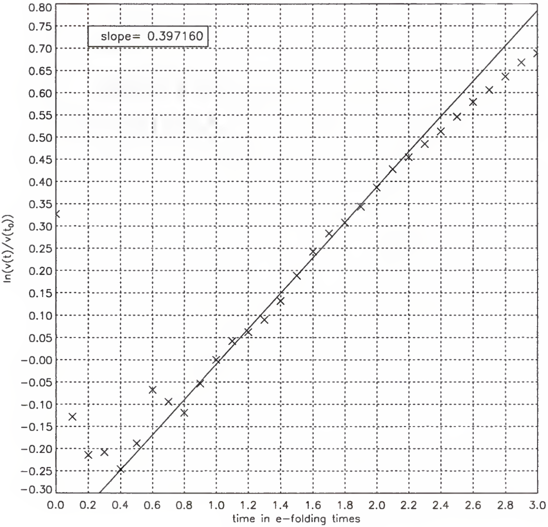

Figure 3.33: Velocity growth for RT model cart257d1. Data points are normalized to the velocity value at $t_0 = 1.0t_e$. The best-fit line using data points from $1.0t_e$ to $2.0t_e$ yields a growth rate of $0.397t_e^{-1}$. The e-folding time is $t_e = 2.115 \times 10^{13}\, s$.

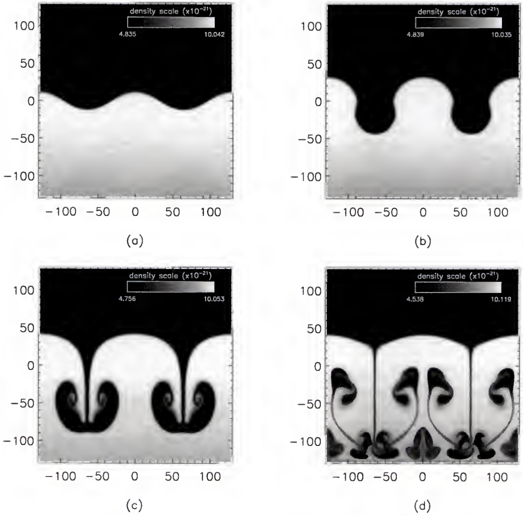

Figure 3.34: Evolution of the SGI for model cnsg257d3. Filled contours show the density distribution at a)$0.5t_e$; b)$1.5t_e$; c)$2.5t_e$; and d)$3.5t_e$. The e-folding time is $t_e = 3.783 \times 10^{13}\,s$. The cell size $\Delta x = \Delta y = 0.1 \times 10^{16} cm$.

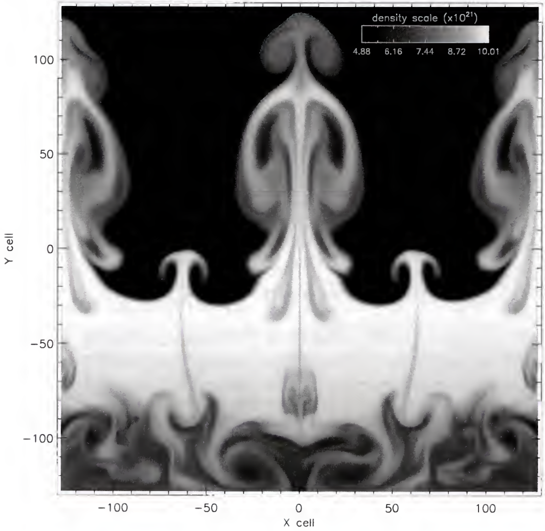

Figure 3.35: Model cnsg257d3 at $t = 5t_e$. The tenuous fingers have long since rebounded from the bottom boundary, but the dense gas is only beginning to impact the top boundary.

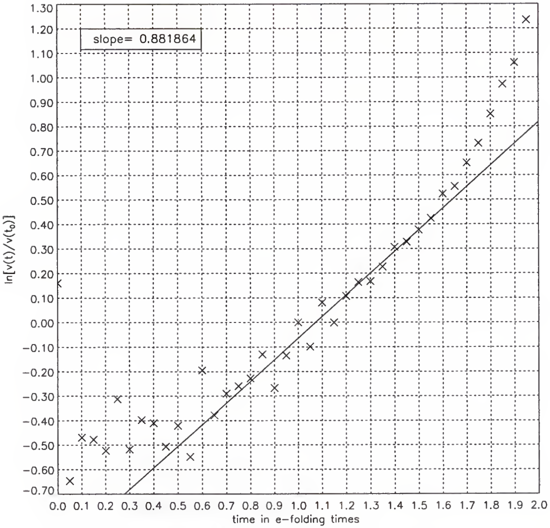

Figure 3.36: Velocity growth for SGI model cnsg257d3. Data points are normalized to the velocity value at $t_0 = 1.0 t_e$. The best-fit line using data points from $0.7 t_e$ to $1.6 t_e$ yields a growth rate of $0.882 t_e^{-1}$. The e-folding time is $t_e = 3.783 \times 10^{13}\, s$.

## 3.5 Discussion

The work presented in this chapter represents the first computational study of the SGI. Although the parameter space considered is not very large (in particular, models with higher density ratios are desirable) some general remarks can be made. The SGI is in some ways similar to the RT instability, but in other ways the two are very different. Both destabilize an interface of discontinuous density; the SGI in the presence of self-gravity, and the RT instability when a dense gas is accelerated into a tenuous gas. Both instabilities preserve the perturbation wavelength well into the nonlinear regime. However, the two instabilities grow in very different manners. The growth of the SGI is characterized by thin fingers of tenuous material streaming into the denser material. In the case of an interface with a low density ratio, the dense medium is displaced very little. The RT instability develops in the opposite manner; thin, dense columns stream into the tenuous medium. When the RT instability acts upon interfaces with different density ratios, the growth rate changes, but the resultant morphologies of the evolved gas remain very much the same. The SGI gives rise to very different morphologies when the density ratio is altered. This will be explored further in future work. A careful look at the velocity growth plots reveals another difference between the SGI and the RT instability. After an early interval of exponential growth, the RT growth rate decreases in the nonlinear stage (e.g. Youngs 1984). Conversely, the growth of the SGI accelerates in the nonlinear phase. (This conclusion must be tempered by the reminder that the boundary conditions used by the gravity solver become less appropriate as the instability develops.) For all of their differences, the SGI and the RT instability can produce structures with similar morphologies when the density ratio at the interface is large. This leads to the speculation that dense columns of gas can form in the ISM due to either the SGI or RT instability. The surrounding environment and the nature of the perturbation determine which instability is dominant.

Table 3.3: Experimental growth rates for SGI and RT models

| model | $\rho_1/\rho_2$ | $\omega$ | $t_e^\dagger$ |
|---|---|---|---|
| hasg257d1 | 2 | $1.028t_e^{-1}$ | 8.458 |
| hnsg257d1 | 2 | $1.031t_e^{-1}$ | 8.458 |
| hnsg257d2 | 5 | $0.735t_e^{-1}$ | 4.728 |
| hart257d1 | 2 | $0.580t_e^{-1}$ | 8.458 |
| hart257d2 | 5 | $0.720t_e^{-1}$ | 4.728 |
| cnsg257e1 | 5 | $0.852t_e^{-1}$ | 2.115 |
| cnsg257d1 | 5 | $0.620t_e^{-1}$ | 2.115 |
| cnsg257d2 | 5 | $0.787t_e^{-1}$ | 2.115 |
| cnsg257d3 | 2 | $0.882t_e^{-1}$ | 3.783 |
| cart257e1 | 5 | $0.836t_e^{-1}$ | 2.115 |
| cart257d1 | 5 | $0.397t_e^{-1}$ | 2.115 |
| cart257d2 | 5 | $0.465t_e^{-1}$ | 2.115 |
| cart257d3 | 2 | $0.306t_e^{-1}$ | 3.783 |

$^\dagger t_e$ is given in units of $10^{13}s$

The theory of HWL does a very good job of predicting growth rates for the SGI. Even though the growth rates given by equation (3.11) were derived in the incompressible, non-stratified limit, the experimental growth rates agree fairly well. The experimental growth rates are summarized in Table (3.3). For the SGI models, the experimental growth rates vary from $0.620t_e$ to $1.031t_e$. The SGI models with an interfacial density ratio of 2 consistently come closer to matching the theoretical growth rate than models with a density ratio of 5. The experimental growth rates for the low temperature SGI models do not show a strong dependence on the $J$ value, although more examples are needed to confirm this. The same cannot be said of the RT models. The experimental RT growth rates are all lower than the theoretical prediction. Contrary to expectations, the closest agreement between theoretical and experimental values is seen for the RT model with the largest degree of stratification. In all cases, the RT growth rate is lower than the corresponding SGI growth rate, perhaps indicating that the SGI growth is impacted less by the use of 2-D simulations.

Very little difference is seen between the $\gamma = 2$ and the $\gamma = 1.4$ models. This independence from $\gamma$ may not hold up as $\gamma$ approaches unity or the velocity amplitude approaches the sound speed. The grid resolution has little effect upon the growth rates of the instabilities, but a higher resolution allows more detailed structures to be seen. The best cell size for problems of this sort is one that strikes a balance between the need for adequate spatial resolution and the desire to minimize boundary effects.

Far more work is needed to understand the SGI and its importance in the ISM. Many variations of hydrostatic models are possible. Different values of density, density ratio, temperature, $\gamma$, $J$, and velocity perturbation amplitude remain to be explored. This study is limited to planar symmetry in Cartesian coordinates. Given the plethora of filamentary structures seen in the ISM, the development of the SGI in cylindrical geometry bears investigation. The SGI behaves differently in cylindrical geometry (Hunter et al. 1998). A cylindrical interface at a radial distance $r_0$ with interior density $\rho_1$ and exterior density $\rho_2$ is stable to kink modes (azimuthal perturbations) but unstable to sausage modes (radial perturbations). Unlike the planar case, growth rates for the sausage modes depend upon the wave number of the perturbation. There exists a maximum wave number, or minimum perturbation wavelength, beyond which a cylindrical interface is stable to the SGI. The condition for instability is $kr_0 < 1.17(1 - \rho_2/\rho_1)$. Future work will include the modeling of the SGI along cylindrical interfaces.

As stated earlier in this chapter, assuming an initial state of hydrostatic equilibrium is not appropriate for the ISM. A thorough study of the ISM must include magnetic fields, turbulence, velocity streams, shocks, heating, and cooling along with gravitational forces. Each process alters the morphology and evolution of the ISM, often in different ways and on different time-scales. As the understanding of the SGI improves, additional physics will be added to the models in order to form a more accurate picture of the ISM. The relative importance of the SGI, when coupled with other instabilities, remains to be determined.

# CHAPTER 4
# COLLIDING GAS FLOWS IN CARTESIAN GEOMETRY

The ISM is a dynamic medium permeated by supersonic flows, which give rise to shocks. Since shocks are always compressive, density enhancements result. This has long fueled speculation that converging velocity fields can trigger protostellar collapse in regions that do not initially contain a Jeans mass of material (e.g. Hunter 1979, Hunter and Fleck 1982, Tohline et al. 1987). In addition to their possible role in facilitating the star formation process, interstellar shocks are worth investigating for their effects on cloud morphology. Shocks are prone to various instabilities (Draine and McKee 1993) which dramatically alter the shape of the ISM. In this chapter and the next, I consider the instability of a dense slab bounded by accretion shocks, a problem previously studied by Hunter, Sandford, Whitaker, and Klein (1986, hereafter HSWK). At issue is whether the head-on collision of supersonic flows can lead to structures which fragment into self-gravitating clumps. Simulations of colliding flows were performed in two dimensions using both Cartesian and cylindrical grids. Each has its advantages and disadvantages. A cylindrical grid is better suited for modeling filamentary structures or systems in which gas flows converge at oblique angles. Self-gravity pulls matter towards the symmetry axis, forming structures which approximate three dimensional spheres. Thus, the most interesting structures (self-gravitating clumps) form along the grid boundary representing the symmetry axis. The boundary conditions must be carefully controlled. Models in Cartesian geometry have no preferred direction. However, a Cartesian grid cannot truly represent any 3-D structure since the third dimension is infinite. Self-gravitating clumps are akin to infinitely extended, radially collapsing cylinders.

Cylindrical models are presented in the next chapter. In this chapter, Cartesian models are considered. First, I summarize the studies of colliding flows and clouds previously done by others. Then, the Cartesian models are described and results presented. The chapter ends with a discussion of how the current results compare to previous studies.

## 4.1 Background

Astronomers have long known that any accurate model of the ISM must account for its dynamical nature (e.g. von Weizsäcker 1951, Chandrasekhar and Münch 1952). As numerical methods have improved over time, many attempts have been made to model dynamical processes in the ISM. A variety of studies have considered the collision of two supersonic gas streams, the collision of two clouds, or the interaction between a stream and a cloud. In all cases, collisions give rise to dense slabs or disks bounded by accretion shocks. At question is whether the interactions of streams or clouds tends to enhance or inhibit star formation. In an early computational study of colliding clouds, Stone (1970a, 1970b) found that although the collision resulted in a large compression, the clouds ultimately re-expanded before gravitational collapse could occur. Hunter and Fleck (1982) reached a different conclusion. They used a virial approach to show that interacting flows enhanced star formation. Regions that start off with an insufficient mass for collapse can be compressed by convergent flows with efficient cooling. The higher density leads to a smaller Jeans mass, allowing collapse to commence. HSWK followed up on this idea with computational models of colliding supersonic gas streams. The models, performed in cylindrical geometry, included self-gravity and molecular cooling. The colliding flows gave rise to a dense disk bounded by accretion shocks. The disk was found to be unstable due to the combined effects of efficient cooling and the continuous ram pressure provided by the accreting shocks. The instability caused the disk to fragment into dense clumps. In the absence of self-gravity, the clumps were short lived objects. When gravity was included in the simulation, fragments along the symmetry axis continued to accrete gas until surpassing the local Jeans mass. These results support the hypothesis that colliding streams enhance the star formation process.

The instability discovered by HSWK was subsequently observed in simulations of colliding wind binaries by Stevens, Blondin, and Pollack (1992, hereafter SBP), who described it as a thin shell instability. Although they considered much hotter gas and higher flow speeds than HSWK, SBP found the morphology of the thin shell instability to be very similar to the earlier models. They also reiterated the need for a cooling mechanism in the post-shock slab. The computational results prompted Vishniac (1994) to perform an analytic study of the instability. He found that when isothermal flows collide, the slab is stable to linear order, but unstable to nonlinear effects once the displacement is comparable to the thickness of the slab. He termed the instability the "nonlinear thin shell instability" (NTSI). The physical basis for the NTSI is the transfer of momentum such that perturbations are enhanced. Suppose that a dense slab is displaced by a bending mode perturbation. Gas which strikes the bottom of the slab will be transported transversely into the regions which are displaced upward. Likewise, the gas striking the top of the perturbed slab will transfer some of its momentum to the downward moving peaks. The cumulative effect causes the displacement to grow. The momentum transfer fueling the growth of the instability must compete against the stabilizing effects of enhanced ram pressure on the peaks moving into the accreting flows and the tendency of the post-shock flow to fill in the ripples. Linear instability is suppressed, so only the nonlinear instability (finite initial amplitude) can grow. Vishniac (1994) derived an approximate growth rate for the NTSI

$$\omega \sim c_s k (kL)^{\frac{1}{2}}, \tag{4.1}$$

where $c_s$ is the sound speed in the slab, $k$ the perturbation wavenumber, and $L$ the slab displacement. Vishniac (1994) confined his analysis to isothermal flows, and was therefore unable to comment on the consequences of altering cooling rates. He did however indicate that a high compression is needed for the development of the NTSI. An efficient cooling mechanism gives rise to higher compressions than the isothermal case, and could therefore enhance the NTSI. More compression will also result from more highly supersonic flows.

The most comprehensive computational study of the NTSI was performed by Klein and Woods (1998, hereafter KW). They used adaptive mesh refinement to model 2-D cloud collisions with high resolution. Self-gravity was not included, but a range of thermodynamic processes was. The NTSI arose when the clouds were seeded with surface perturbations prior to collision. Models without surface perturbations did not show the NTSI, which lends support to the notion that the instability is strictly nonlinear. When radiative cooling was included in their models, KW produced results similar to the previous computational models. They also considered isothermal models in order to compare the results with Vishniac's (1994) analytical theory. They found that a higher grid resolution was needed to see the NTSI in the isothermal case. The isothermal NTSI showed a similar morphology to the NTSI in models with cooling, but the global quantities of the post-collision clouds varied between the two cases. For example, the isothermal case overestimated the compression in the collision mid-plane. This indicates that the cooling mechanism used by KW was rather weak. A strongly cooling shock leads to a higher compression than an isothermal shock. Also, KW used a magnetic pressure term to limit the compression in their radiative models, but not in their isothermal models. The experimental growth rate found by KW for their isothermal models agreed with the prediction by Vishniac (1994). KW also considered adiabatic cloud collisions. They found that a minimum compression of 10 was needed to drive the NTSI. An adiabatic compression of 10 in the limit of very high Mach number (velocity divided by sound speed) corresponds to a value of $\gamma = 1.22$. This result for adiabatic cloud collisions is contrary to the earlier studies which emphasized the need for a strong cooling mechanism to drive the NTSI.

Miniati et al. (1997) considered cloud collisions and explored the difference in behavior between isothermal clouds and clouds with radiative cooling. They found that symmetric cloud collisions in the isothermal limit behaved in a manner similar to adiabatic collisions and lead to the disruption of merged clouds. When radiative cooling was applied, symmetric clouds coalesced into a single cloud.

The behavior of a shock bounded slab and the development of the NTSI has been studied in some detail in a variety of physical regimes. Here, I revisit the methodology of HSWK with CFDLIB and in light of the studies which have come after. I examine the stability of a cold, dense slab formed by the collision of identical supersonic gas streams. I consider in detail the effects of varying the cooling rates on the growth of the NTSI and the fragmentation of the slab. At issue is whether the collision of gas streams and the subsequent instabilities give rise to collapsing clumps.

## 4.2 Models

The physical parameters chosen for these models are characteristic of cold molecular cloud cores. The gas is treated as molecular hydrogen with a molecular weight $\mu = 2$ and a ratio of specific heats $\gamma = 1.4$. Low resolution (129×129 cells) models are assigned a cell size of $dx = dy = 5 \times 10^{15}\, cm$. The total spatial extent of the grid is therefore $6.45 \times 10^{17}\, cm$, or about $0.21\, pc$. Observations of cloud cores with sizes of the order of $0.1\, pc$ reveal typical kinetic temperatures of $\sim 10\, K$ and number densities $\sim 10^4\, cm^{-3}$ (e.g. Lada et al. 1993 and references therein). Accordingly, an initial density of $\rho_i = 10^{-21}\, g\, cm^{-3}$ is used, which corresponds to a number density of $n(\mathrm{H}_2) \sim 300$. The initial temperature is $T_i = 100K$, but efficient cooling mechanisms (see section 2.3) drive the temperature lower in both the pre-shock and post-shock regions. The pre-shock velocities of the streams are opposite in direction and of the same magnitude, $v_i = \pm 5\,km\,s^{-1}$. The streams are supersonic. The Mach number varies with the temperature, which in turn depends upon the cooling rate. In the absence of cooling, the Mach number for flows with temperatures of $100\,K$ is $M = 6.6$. But if the gas cools to $40\,K$ before the reaching the shock, a lower sound speed results in a higher Mach number, $M = 10.4$. The changing dynamical behavior of the gas as the amount of cooling is varied is a central theme of this study. The amount of cooling is described by the parameter $q$, defined as the fraction of the full cooling rate used in a simulation. A model with $q = 1$ applies the full cooling rate; whereas, a model with $q = 0.3$ applies a cooling rate that is reduced to 30% of its full value.

Each simulation begins with the gas in the lower half of the grid streaming upward and the gas in the upper half of the grid streaming downward, with a static zone in the center. The width of the static zone varies, but typical values are three or five cells. The bottom and top of the grid (the horizontal boundaries) have inflow boundary conditions. Throughout the simulation, material enters the grid with the same density, temperature, and velocity as the initial flows. Along the left and right sides (the vertical boundaries), the gas is allowed to flow into and out of the grid freely. At each computational step, the total mass on the grid increases by an amount equal to the inflowing mass at the horizontal boundaries, plus the inflowing mass from the vertical boundaries, minus the amount of mass which escapes the grid at the vertical boundaries. The inflow and outflow along the vertical boundaries can result in the generation of vortices, but typically do not alter greatly the evolution of the slab.

When the post-shock material is allowed to cool, the colliding flows give rise to a cold, dense slab which continues to accrete matter. The slab remains stable for a long time (about $1.6 \times 10^{13}\,s$) before numerical noise at the boundaries gives rise to an instability which propagates into the slab. Perturbations are induced in the slab well before this time to minimize the effects of the noise. The perturbation is applied to the $y$ component of the velocity and has the form

$$v_y = v_y + 0.01 v_i \cos{(kx)} e^{-k|y-y_s|}, \tag{4.2}$$

where $k$ is the wavenumber of the perturbation, and $y_s$ the position of the slab center. The slab is allowed to reach a high density through accretion prior to being perturbed.

For models requiring self-gravity, the potential is found using MUDPACK in a manner very similar to the method used for the SGI models in Chapter 3. However, the process is a bit more complicated due to the mass inflow. Periodic boundary conditions are applied along the vertical boundaries, but are not suitable at the horizontal boundaries. The horizontal boundaries require conditions that change as the mass on the grid increases. For these models, the boundary values for the gradient of the potential are approximated by considering the potential of an infinitely extended plane. During each computational cycle, an average slab density $\rho_s$ is determined such that the amount of mass in a uniform slab of density $\rho_s$ matches the mass of the perturbed (or unperturbed) slab. The contribution to the potential from the pre-shock flows is ignored due to the low density in the flows relative to the cold slab. The potential gradient for an infinite plane of density $\rho_s$ and thickness $\Delta y$ is a constant in space, $d\Phi/dy = 2\pi G \rho_s \Delta y$. For an unperturbed dense slab, this approximation works well. As instabilities grow and the slab begins to fragment, the approximation fails. Any results from self-gravitating Cartesian models must be viewed with this limitation in mind. Self-gravity is not applied from the beginning of the simulation, but after the dense slab is formed. A sufficient amount of mass must accumulate before gravitational forces can compete with the dynamic forces.

## 4.3 Results

The dynamic instability of a slab and the role played by the thermodynamics of the gas are examined using models without self-gravity. Figure (4.1) shows the growth of an accretion bounded slab formed by the collision of adiabatic gas streams.

The post-shock temperature is much higher than the pre-shock temperature. Internal thermal pressure supports the slab against the ram pressure of the accreting flows. The hot, dense slab quickly grows in width. The compression of a shock formed by adiabatic streams with Mach number $M$ is (Harlow and Amsden 1971)

$$\frac{\rho_s}{\rho_i} = \frac{\gamma + 1}{\gamma - 1 + (2/M^2)}, \tag{4.3}$$

where $\rho_s$ is the post-shock slab density and $\rho_i$ the pre-shock density. For flows of very high Mach number, the compression approaches an upper limit of $(\gamma+1)/(\gamma-1)$. For a molecular gas with $\gamma = 1.4$, the maximum compression is 6. The contours in figure (4.1) show that compression at the center of the slab is greater than 6. This is better seen in the line cuts shown in figure (4.2). The density, temperature, pressure, and $y$-velocity are plotted along a constant value of $x$ at $t = 0.8 \times 10^{12} s$. The grid resolution is insufficient to resolve the initial shock. As a result, the density profile has a central peak, and the temperature profile has a central dip. The two cancel each other out in determining the pressure, which remains flat inside the slab. Such behavior at shocks is common among grid codes which attempt to take numerical derivatives across a discontinuity. The density spike can be reduced by applying additional temperature and momentum diffusion to smear the shock more. However, doing so results in a slab more prone to fragmentation when cooling is applied. Over time, the central density peak decreases in the adiabatic case. For models with molecular cooling, the temperature inside the slab falls far below the dip seen for the adiabatic case. The central density spike at the point of collision serves only to enhance the overall cooling by a small amount. Its presence has no bearing on the evolution of cooling models.

When radiative cooling is added to the simulations, the slab grows to a far greater density than is possible for an adiabatic shock. The maximum slab density attainable is constrained in each model by the amount of time that passes before instabilities arise in the unperturbed slab. Examples are shown in figures (4.3) and

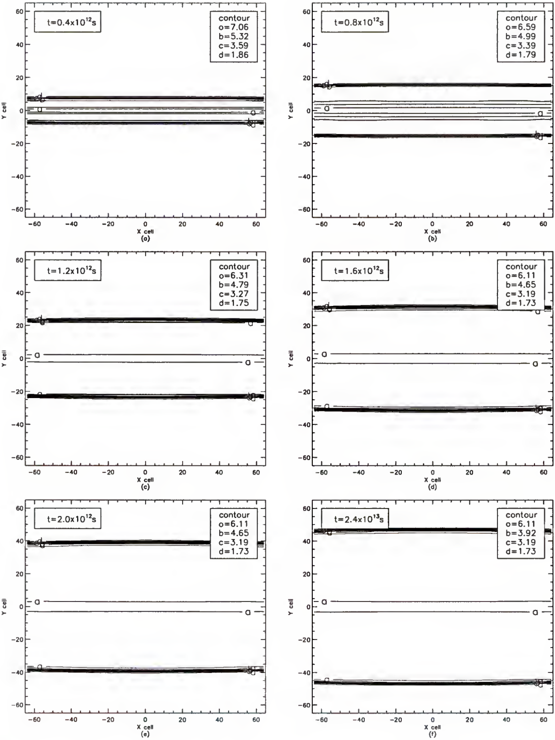

Figure 4.1: Propagation of an adiabatic $\gamma = 1.4$ accretion shock. Density contours are labeled in units of the initial density ($\rho_i = 10^{-21} g\, cm^{-3}$) and shown at times of a)$0.4 \times 10^{12} s$; b)$0.8 \times 10^{12} s$; c)$1.2 \times 10^{12} s$; d)$1.6 \times 10^{12} s$; e)$2.0 \times 10^{12} s$; and f)$2.4 \times 10^{12} s$.

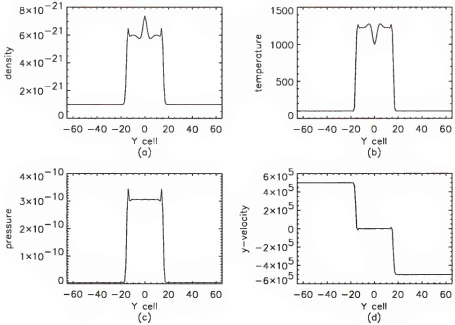

Figure 4.2: Adiabatic accretion shock line cuts at $t = 0.8 \times 10^{12}s$. Cuts along a constant value of $x$ show the a)density; b)temperature; c)pressure; and d)$y$-velocity.

(4.4) for models with $q = 1$ (full cooling) and $q = 0.3$, respectively. The $q = 1$ model maintains slab stability a short while longer, but otherwise the two results are very similar. In both cases, the slab remains flat and stable until $t \sim 1.6 \times 10^{13}s$, beyond which wiggles are seen near the vertical boundaries. In order to insure that boundary effects do not modify the growth of instabilities in the slab, an induced perturbation is applied long before the slab would otherwise go unstable. Perturbation times of $5 \times 10^{12}s$ and $10^{13}s$ are considered. Inflows into the slab along the vertical boundaries result in slightly higher densities at the edges than is found throughout the rest of the slab. The maximum slab density before instability takes hold is about $3000\rho_i$. This is a much higher compression than that seen by HSWK, who noted a maximum compression of about $700\rho_i$ for inflows of $5\,km\,s^{-1}$. They attributed their low compression to the high numerical diffusion inherent to their code. KW included a magnetic pressure term in their models which limited the compression to a factor of 50. In contrast, the cloud collision models of Miniati et al. (1997), which included

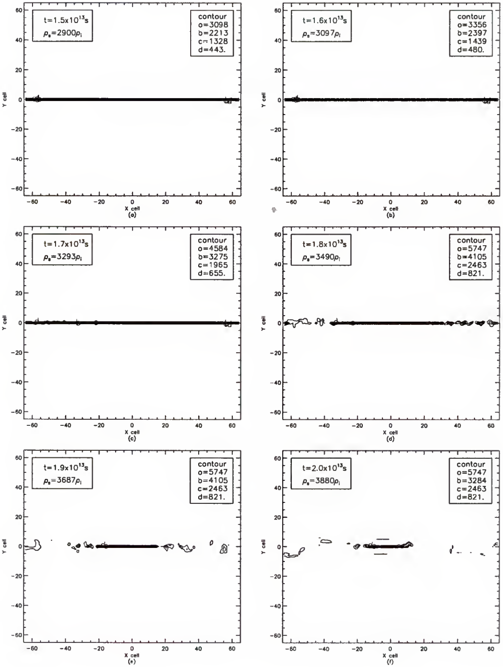

Figure 4.3: Instability development for an unperturbed slab with $q = 1$. Density contours are labeled in units of the initial density ($\rho_i = 10^{-21} g\,cm^{-3}$) and shown at times a)$1.5 \times 10^{13}s$; b)$1.6 \times 10^{13}s$; c)$1.7 \times 10^{13}s$; d)$1.8 \times 10^{13}s$; e)$1.9 \times 10^{13}s$; and f)$2.0 \times 10^{13}s$. The maximum compression in the center of the slab is labeled $\rho_s$. Note how instabilities form at the edges of the grid before propagating towards the center.

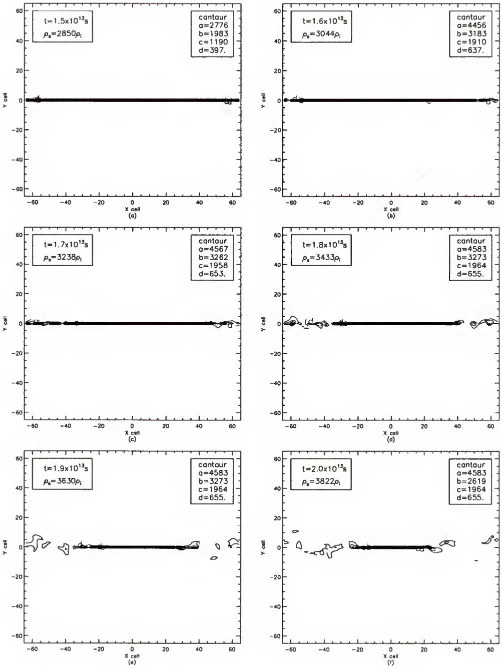

Figure 4.4: Instability development for an unperturbed slab with $q = 0.3$. Density contours are labeled in units of the initial density ($\rho_i = 10^{-21} g\,cm^{-3}$) and shown at times a)$1.5 \times 10^{13} s$; b)$1.6 \times 10^{13} s$; c)$1.7 \times 10^{13} s$; d)$1.8 \times 10^{13} s$; e)$1.9 \times 10^{13} s$; and f)$2.0 \times 10^{13} s$. The maximum compression in the center of the slab is labeled $\rho_s$. Instabilities form at the edges and propagate towards the center.

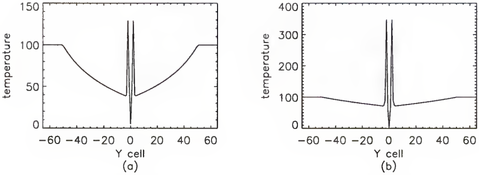

Figure 4.5: Temperature profiles for unperturbed models at $1.5 \times 10^{13}s$. Each plot shows a line cut along constant $x$ for a cooling model with a)$q = 1$; and b)$q = 0.3$.

radiative cooling, reached a compression of about $10^4$. The NTSI shows similar behavior in all of these studies, which indicates that the strength of compression is not critical provided it exceeds some minimum value. Indeed, results presented below demonstrate that the instability and fragmentation of the slab proceed in a nearly identical fashion whether the slab density at the time of perturbation is $\sim 1000\rho_i$ or $\sim 2000\rho_i$.

The initial temperature of the inflowing gas is $100\,K$. The flows begin to cool once they are within 50 cells ($2.5 \times 10^{17}cm$) of the slab. The temperature of the gas as it strikes an accretion shock depends upon the value of $q$. Figure (4.5) shows the temperature profiles at $1.5 \times 10^{13}s$ for the models shown in figures (4.3) and (4.4). When full cooling is applied ($q = 1$), the gas cools to $40\,K$ before reaching the accretion shock. The temperature of the shocked gas rises to $129\,K$ before the high slab density drives the gas to cool to the minimum of $5\,K$. In a model with a lower cooling rate ($q = 0.3$), the gas cools to $72\,K$ before reaching the shock, spikes to a temperature of $348\,K$, and then quickly cools to $5\,K$. Despite the difference in temperature jump at the shock between the two models, the cooling is sufficiently strong in both to lower the temperature to the lowest value allowed. As a result, the central slab densities in the models are very similar. Only when perturbations are imposed upon the slab are significant structural differences seen among models with varying degrees of cooling.

### 4.3.1 Earlier Perturbation Time

When a velocity perturbation (equation 4.2) is imposed upon the slab, models with different cooling rates produce very different results. The perturbation is applied at $t = 5 \times 10^{12} s$ when the density in the center of the slab is $\rho_s = 945\rho_i$. For the models shown here, three full waves are placed across the grid, resulting in a wavenumber of $k = 2\pi/\lambda = 2.92 \times 10^{-17} cm^{-1}$. Figures (4.6–4.12) show the instability growth for perturbed slabs in models utilizing different cooling rates. The base 10 logarithm of the density is plotted to highlight the morphology of the evolved slabs. The results demonstrate that the thermodynamic properties of the ISM have a profound affect upon the evolution of a perturbed slab. When the full cooling rate is used (figure 4.6) the perturbation develops into well defined extrema. Velocity streaming inside the slab drives the formation of Kelvin-Helmholtz instabilities which give rise to secondary peaks. Secondary peaks between the extrema quickly grow, so that the initial signature of the perturbation is largely erased. In contrast, models with much lower cooling rates, figures (4.10–4.11), develop extrema more slowly and preserve the shape of the perturbation for longer times. Kelvin-Helmholtz instabilities develop more slowly or not at all. There is a lower limit to this trend. The $q = 0.1$ model shown in figure (4.12) develops slowly in a way quite unlike all other models. This indicates that there exists a lower limit to the amount of cooling required to drive the NTSI. All of the models share the characteristic that the density range changes very little once the instability has grown to an appreciable size. The inflowing gas acts to further displace and enlarge the slab rather than compress it. As the perturbation grows, the pre-shock gas cools by different amounts before reaching the shock, resulting in a temperature gradient on the shock surface. In most cases (the $q = 0.2$ case being clearest exception) the instability growth is suppressed along the vertical

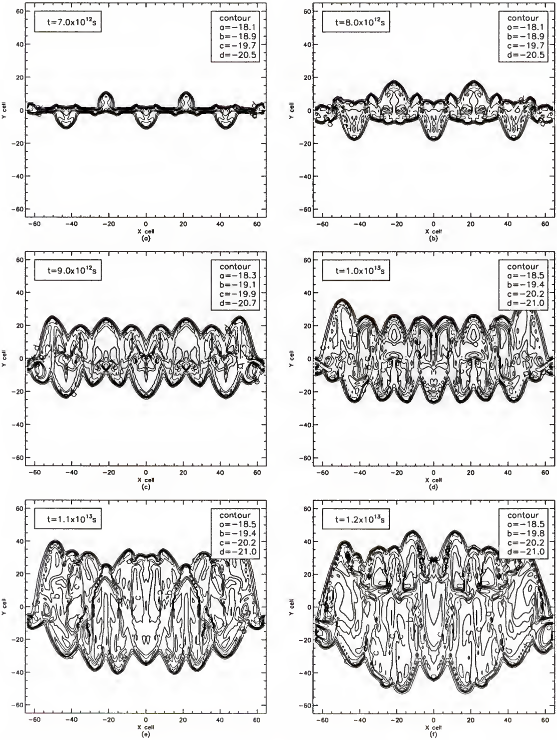

Figure 4.6: Instability development for a perturbed slab with $q = 1$. $\text{Log}_{10}$ density contours are shown at times a)$7.0 \times 10^{12}s$; b)$8.0 \times 10^{12}s$; c)$9.0 \times 10^{12}s$; d)$1.0 \times 10^{13}s$; e)$1.1 \times 10^{13}s$; and f)$1.2 \times 10^{13}s$. The time of perturbation is $5.0 \times 10^{12}s$.

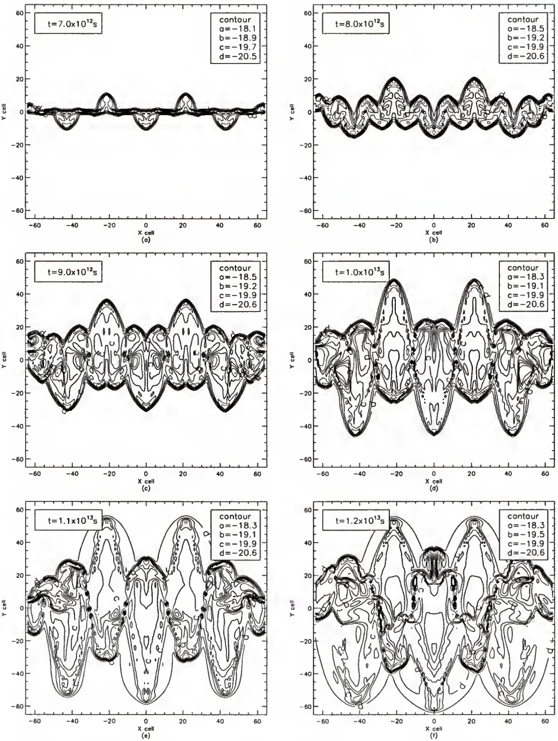

Figure 4.7: Instability development for a perturbed slab with $q = 0.8$.

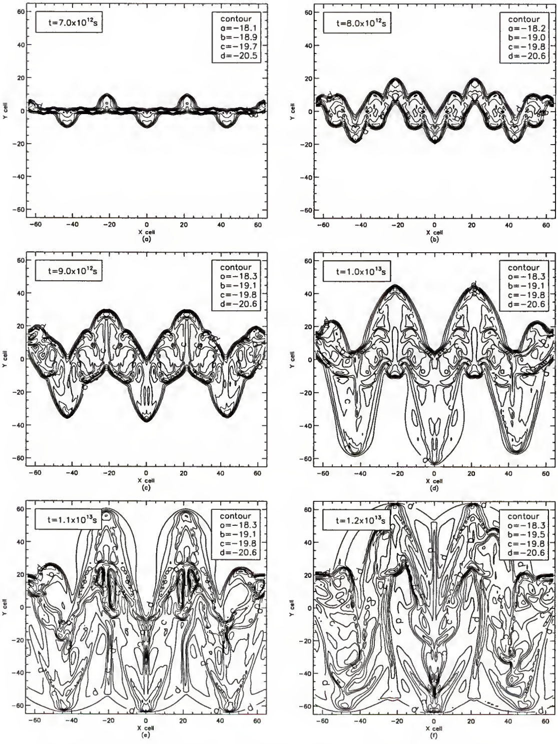

Figure 4.8: Instability development for a perturbed slab with $q = 0.6$.

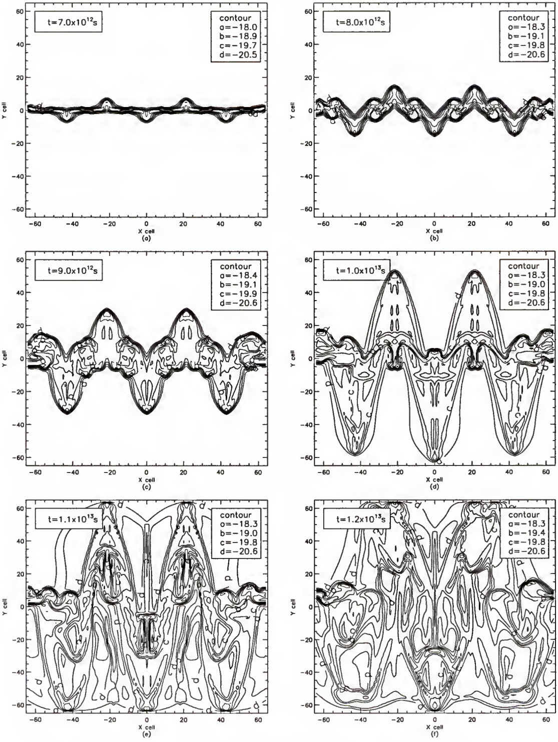

Figure 4.9: Instability development for a perturbed slab with $q = 0.4$.

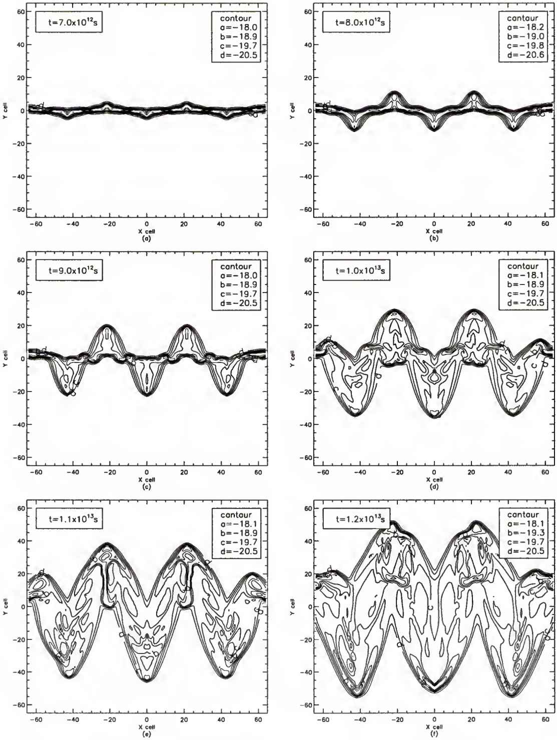

Figure 4.10: Instability development for a perturbed slab with $q = 0.3$.

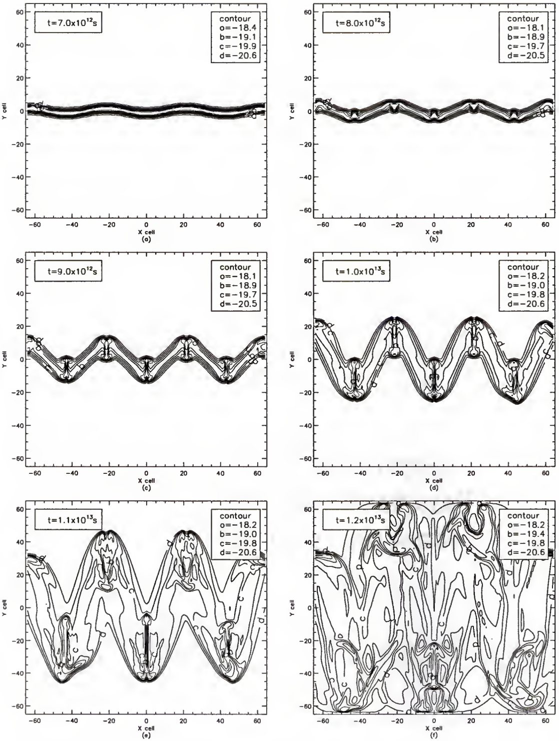

Figure 4.11: Instability development for a perturbed slab with $q = 0.2$.

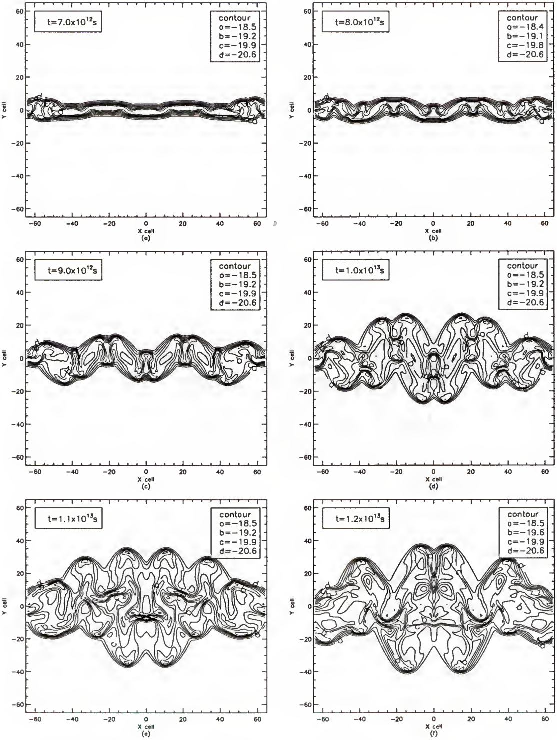

Figure 4.12: Instability development for a perturbed slab with $q = 0.1$.

boundaries where inflows and outflows are allowed. The $q = 0.2$ and $q = 0.3$ models resemble the low resolution results of KW. The models with an intermediate $q$ value appear to correspond to the results of HSWK, but a direct comparison is difficult since their models did not include induced perturbations.

For a more detailed analysis, I concentrate on two models which highlight the differences between a fast cooling rate (the full cooling $q = 1$ model) and a slow cooling rate (the $q = 0.3$ model). First, I consider the model with full cooling. In figure (4.13), the density distribution at $t = 1.1 \times 10^{13} s$ is recreated as a grayscale image with velocity vectors superimposed. (Note that the density scale is opposite to that used in chapter 3. Here the darkest regions are the densest.) The largest density of $\rho = 1300\rho_i$ is found along the left boundary. Excluding the boundaries, the maximum density in the slab is $505\rho_i$, which is roughly one half the slab density at the time of perturbation. The lowest density inside the slab is $0.46\rho_i$. Despite the continuing inflow, the internal density falls as the slab grows in size and spreads its mass over a larger volume. For an unperturbed slab, the density after $1.1 \times 10^{13} s$ is $2120\rho_i$. The instability results in a much lower density than that found in a stable accreting slab. The velocity vectors show that the impacting flows form channels which penetrate through most of the slab before encountering material streaming from the other side. Dense filaments pervade the slab and surround evacuated regions. In the most tenuous regions inside the slab, the gas is nearly static. Evidence of vortices is seen, but the bulk of the flow maintains a straight path through the slab.

The $q = 0.3$ model evolves very differently, yet retains many of the same characteristics. Figure (4.14) shows the density distribution and velocity vectors at $t = 1.1 \times 10^{13} s$. Once again, the largest density, $\rho = 1070\rho_i$, appears at an edge. The densest region away from the boundaries has a density of $473\rho_i$. Nowhere inside the slab does the density fall below the inflow density. As in the $q = 1$ model, the accreting flows strike a peak in the displacement and are channeled along the surface

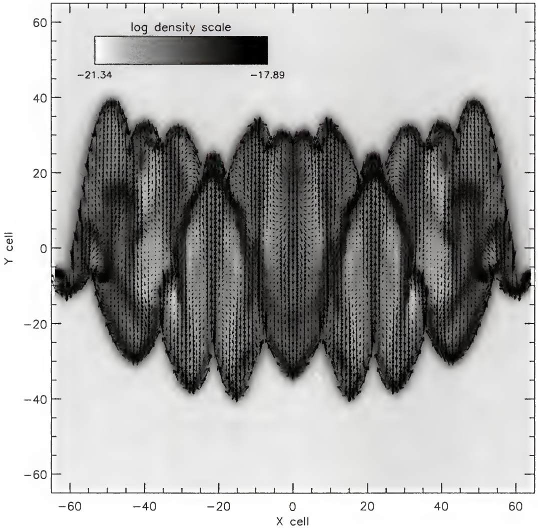

Figure 4.13: Perturbed slab morphology for a $q = 1$ model at $t = 1.1 \times 10^{13} s$. Velocity vectors are superimposed upon a grayscale image of $\log_{10}(\rho)$. Only vectors with a magnitude below $2 \times 10^5 cm\, s^{-1}$ are plotted. Regions not represented with vectors have flows of higher magnitude.

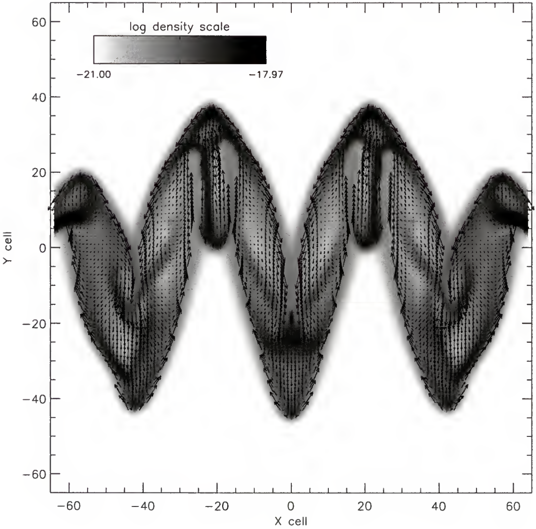

Figure 4.14: Perturbed slab morphology for a $q = 0.3$ model at $t = 1.1 \times 10^{13} s$. Only velocity vectors with a magnitude below $2 \times 10^5 cm\, s^{-1}$ are plotted.

and into the slab. The channels for the $q = 0.3$ model are more widely spaced due to the lack of secondary peaks. Internal filaments and regions of vorticity are clearly seen inside the slab. When the $q = 0.3$ model is perturbed using a sine function rather than a cosine function, the results are similar. Figure (4.15) shows the density and velocity vectors at $t = 1.1 \times 10^{13} s$. Only velocity magnitudes below $10^5\, cm\, s^{-1}$ are plotted in order to bring out the low velocity vortices in the slab interior. Note the well defined dense and tenuous regions inside the slab. The velocity vectors show regions of vorticity adjacent to the dense filaments, as well as oppositely directed streams bordering the tenuous regions. Oppositely directed streams may give rise to Kelvin-Helmholtz instabilities within the slab. The lobes along the vertical boundaries are large regions of circulation.

The addition of self-gravity to the simulations does not greatly affect the results, although slab morphologies are altered. For both the $q = 1$ and $q = 0.3$ models, self-gravity was turned on at the same time the slab was perturbed. The slab density at $t = 5 \times 10^{12} s$ is about $945 \rho_1$, which corresponds to a Jeans length (equation 2.38) of $1.20 \times 10^{17} cm$ for a $5\, K$ gas. This is smaller than the $2.15 \times 10^{17} cm$ perturbation wavelength. However, since most of the mass on the grid is contained inside the slab, a better criterion for stability is the minimum wavelength for the instability of a uniform sheet. For a sheet with a surface density $\Sigma$, the critical wavelength for gravitational collapse is (Binney and Tremaine 1987)

$$\lambda_c = \frac{\gamma RT}{\mu \Sigma G}. \tag{4.4}$$

Using $\Sigma = \rho_s \Delta x$, the result for a $5\, K$ gas is $\lambda_c = 9.23 \times 10^{17} cm$. This exceeds the total spatial extent of the grid and is more than four times the perturbation wavelength. The slab is not unstable to global collapse. For the $q = 1$ model very little difference is seen between gravitating and non-gravitating models. Figure (4.16) shows the density distribution and velocity vectors at $t = 1.1 \times 10^{13} s$ for the $q = 1$ case. The peaks are somewhat sharper and gravity has suppressed the number of

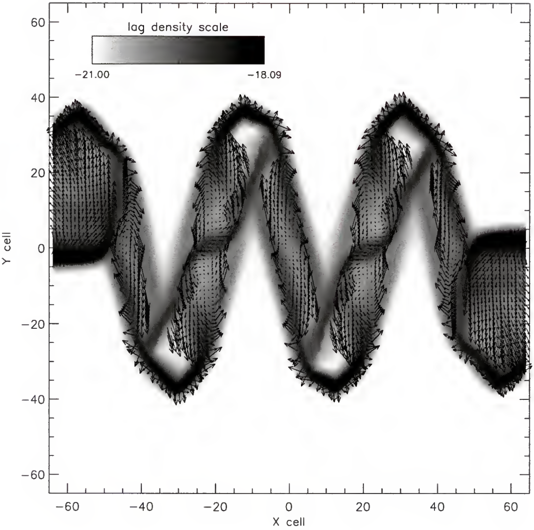

Figure 4.15: Morphology for a $q = 0.3$ model perturbed with a sine function. Only velocity vectors with a magnitude below $1 \times 10^5 cm\, s^{-1}$ are plotted.

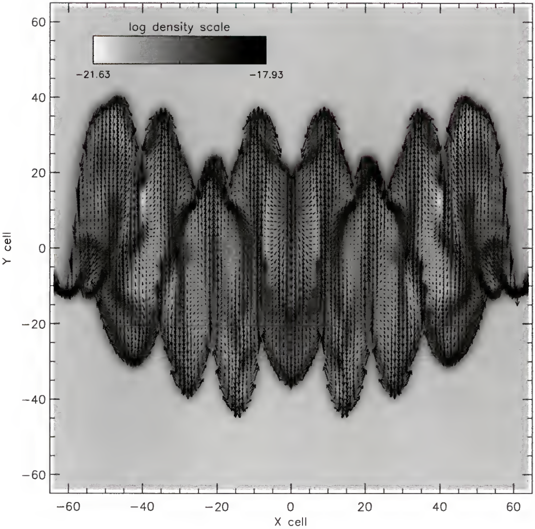

Figure 4.16: Morphology of a self-gravitating, perturbed slab with $q = 1$ at $t = 1.1 \times 10^{13} s$. Only velocity vectors with a magnitude below $2 \times 10^5 cm\, s^{-1}$ are plotted.

secondary peaks along the upper surface of the slab. The largest density of $1190\rho_1$ is lower than the maximum observed for the non-gravitating model and is found along the right edge of the grid. The largest density away from the boundaries is $600\rho_i$, a value larger than that for the non-gravitating case. The $q = 0.3$ case shows a greater difference between the gravitating and non-gravitating cases. Figure (4.17) shows the density distribution and velocity vectors at $t = 1.1 \times 10^{13}s$ for the $q = 0.3$ case. The shape of the perturbation is once again preserved, but additional ripples have formed along the slab surface. The flow pattern inside the slab has been altered as well. The maximum density along the left edge is $1740\rho_i$. Away from the edges the maximum density is $653\rho_i$. The $q = 0.3$ model produces regions of higher density than the $q = 1$ model when self-gravity is included. However, in neither case are any clumps seen of sufficient density to undergo collapse. The slab instability always results in lower densities than those in unperturbed slabs allowed to continuously accrete material.

### 4.3.2 Later Perturbation Time

The same experiments were repeated for the $q = 1$ and $q = 0.3$ models using a later perturbation time. The form and amplitude of the perturbation are the same. The new time of perturbation is $t = 10^{13}s$, so the slab is allowed to accrete material for twice as long as in the previous models. The slab density at the time of perturbation is $\rho_s = 1920\rho_i$. (As previously noted, along the vertical boundaries the density of the unperturbed slab is higher.) The slab evolution for the $q = 1$ model (figure 4.18) is quite different than when perturbed earlier. Internal flows are harder to initiate inside the denser slab, so Kelvin-Helmholtz instabilities develop more slowly. Fewer secondary peaks arise, and at late times the initial form of the perturbation can still be distinguished. The density distribution is shown in more detail along with the velocity vectors in figure (4.19) for $t = 1.6 \times 10^{13}s$. The highest density within the slab (but away from the boundaries) is $1030\rho_i$, which is again about one-half the density at the time of perturbation. The minimum density within the slab is $0.70\rho_i$.

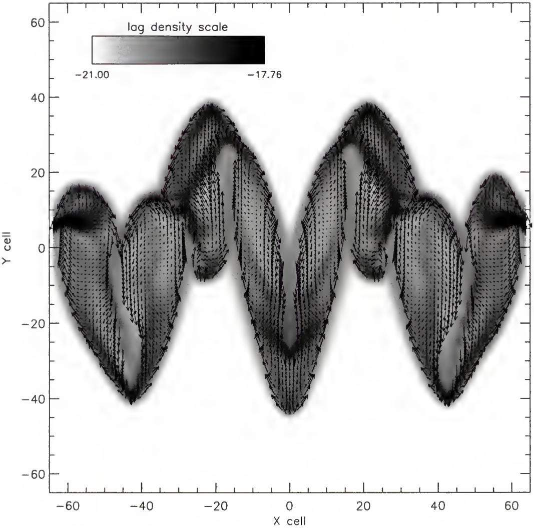

Figure 4.17: Morphology of a self-gravitating, perturbed slab with $q = 0.3$ at $t = 1.1 \times 10^{13} s$. Only vectors with a magnitude below $2 \times 10^5 cm\, s^{-1}$ are plotted.

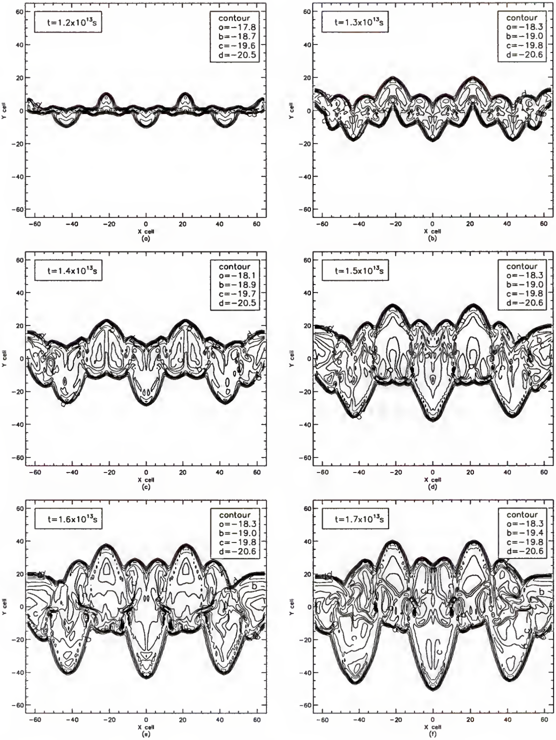

Figure 4.18: Evolution of a $q = 1$ model perturbed at $1.0 \times 10^{13}s$. Log$_{10}$ density contours are shown at times a)$1.2 \times 10^{13}s$; b)$1.3 \times 10^{13}s$; c)$1.4 \times 10^{13}s$; d)$1.5 \times 10^{13}s$; e)$1.6 \times 10^{13}s$; and f)$1.7 \times 10^{13}s$.

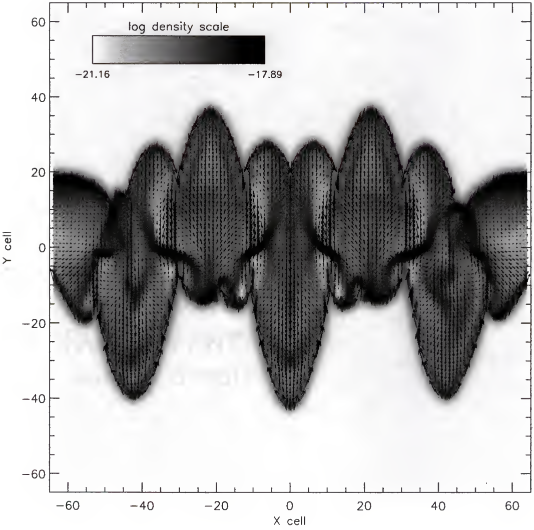

Figure 4.19: Perturbed slab morphology for a $q = 1$ model at $t = 1.6 \times 10^{13} s$. Only velocity vectors with a magnitude below $2 \times 10^{5} cm\, s^{-1}$ are plotted.

Inside the slab, the densest patches of gas are filaments formed by the collision of oppositely directed channels. This is in contrast to the earlier perturbation model in which the densest filaments are formed by a single upward or downward directed stream.

The evolution of the slab perturbed at $t = 10^{13}s$ for the $q = 0.3$ case is shown in figure (4.20). This model shows less variation with the change in perturbation time than the $q = 1$ model. Overall, the morphology of the evolved slab remains largely unchanged. One difference is that less structure is seen throughout the slab interior as the instability grows than in the earlier perturbation model (figure 4.10). Figure (4.21) shows the density distribution and velocity vectors at $t = 1.6 \times 10^{13}s$. Large vortices appear in the slab interior. The maximum density along the boundaries is $1330\rho_i$, and the densest region away from the boundaries is not much lower at $1170\rho_i$. This density is located on the right-most peak at (45,-35). It is interesting to note that if the cells along the boundaries are excluded, the $q = 1$ model produces higher densities than the $q = 0.3$ model when the slab is perturbed at $t = 5 \times 10^{12}s$, but the opposite occurs when the slab is perturbed at $10^{13}s$.

The addition of self-gravity to the simulations is expected to have a larger significance when the slab is perturbed at a later time. As before, self-gravity is turned on at $t = 5 \times 10^{12}s$. At $t = 10^{13}s$, the density in the unperturbed slab is $\rho_s = 1920\rho_i$. From equation (4.4), the maximum stable wavelength is $4.54 \times 10^{17}cm$, which is still larger than the perturbation wavelength. The slab is stable to global collapse. Despite the denser slab, the self-gravitating models are not very different from the non-gravitating models. Figure (4.22) shows the gravitating $q = 1$ case at $t = 1.6 \times 10^{13}s$. Other than a change in the location of some filaments and some alterations to the peaks, the morphology matches that of the non-gravitating case (figure 4.19). However, the densest filament in the gravitating case (located at (50,0)) has a density of $1540\rho_i$. This is much denser than any filament in the

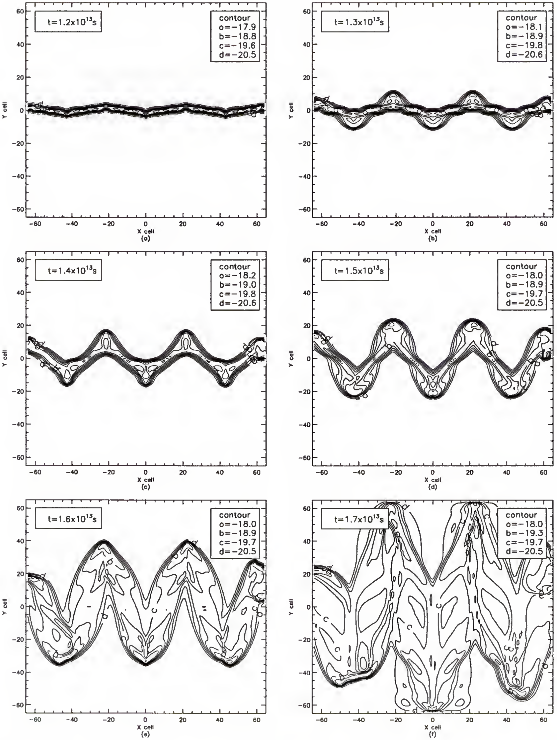

Figure 4.20: Evolution of a $q = 0.3$ model perturbed at $1.0 \times 10^{13}s$. $\text{Log}_{10}$ density contours are shown at times a)$1.2 \times 10^{13}s$; b)$1.3 \times 10^{13}s$; c)$1.4 \times 10^{13}s$; d)$1.5 \times 10^{13}s$; e)$1.6 \times 10^{13}s$; and f)$1.7 \times 10^{13}s$.

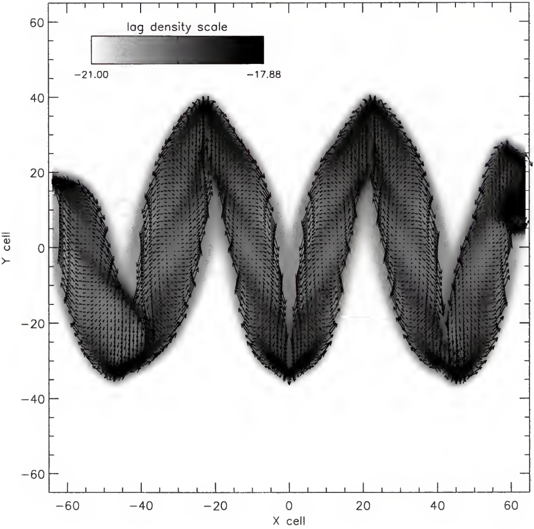

Figure 4.21: Perturbed slab morphology for a $q = 0.3$ model at $t = 1.6 \times 10^{13} s$. Only velocity vectors with a magnitude below $2 \times 10^5 cm\, s^{-1}$ are plotted.

non-gravitating case, but still well below the density needed to initiate collapse. A comparison between gravitating (figure 4.23) and non-gravitating (figure 4.21) simulations for the $q = 0.3$ model reveals very similar morphologies. The only major differences between the two results are the locations and magnitudes of the densest regions. In the gravitating case, the highest density of $1720\rho_i$ is found along the left boundary. The maximum density inside the slab is $916\rho_i$, a value lower than that for the non-gravitating case. Contrary to expectations, for the $q = 0.3$ case self-gravity has a weaker effect upon the growth of the instability when the slab is perturbed at a later time. This may be an indication of the inaccuracy of the gravity algorithm when applied to inflow models in Cartesian geometry.

In order to examine the behavior of perturbed adiabatic slabs, a series of non-cooling models was run with varying values of $\gamma$. In addition to $\gamma = 1.4$, values of 1.1, 1.2, and 1.3 were considered. In each case, the center of the hot slab was perturbed before the thickness of the slab was large. According to the results of KW, the NTSI appears in adiabatic shocks provided the compression is greater than ten. By this criterion, the $\gamma = 1.1$ and $\gamma = 1.2$ models should be unstable to the NTSI, while the other two are stable. My results do not support this idea. No instability was seen in any of the adiabatic models. The material inside the adiabatic slab is nearly static, so an induced perturbation does lead to the displacement of material. However, the displacement does not grow over time. The same phenomenon is seen in all adiabatic models, regardless of $\gamma$. Either the resolution is too low in these models to reproduce the findings of KW, or the differences between the physical processes (colliding flows versus colliding clouds) lead to different behavior. Continuous inflow in the colliding flow models causes an adiabatic slab to rapidly grow in thickness. The collision of clouds of finite extent is different in that the amount of accreting material (and hence the growth of an adiabatic slab) is finite. It is possible that a continuous inflow of matter wipes out the NTSI in adiabatic models.

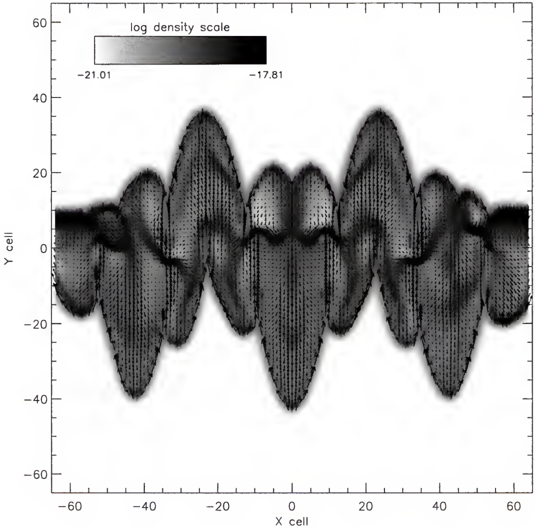

Figure 4.22: Morphology of a self-gravitating, perturbed slab with $q = 1$ at $t = 1.6 \times 10^{13} s$. Only velocity vectors with a magnitude below $2 \times 10^5 cm\, s^{-1}$ are plotted.

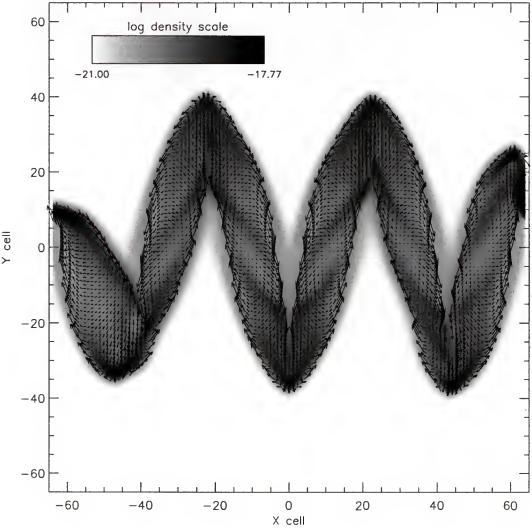

Figure 4.23: Morphology of a self-gravitating, perturbed slab with $q = 0.3$ at $t = 1.6 \times 10^{13} s$. Only velocity vectors with a magnitude below $2 \times 10^5 cm\, s^{-1}$ are plotted.

## 4.4 Discussion

The main conclusion to be reached from the Cartesian models is that the cooling rate plays a controlling role in determining the evolution of a perturbed cold slab. In models with strong cooling, a perturbed slab is prone to the development of short wavelength modes which override the initial perturbation. Weakly cooling models tend to preserve the perturbation wavelength for long times. In all cases, the slab density decreases as the gas is spread over a larger volume. Streaming motions within the slab give rise to filaments and vortices. The slab ultimately fragments into a few dense islands of material, but no collapsing clumps are observed. Altering the cooling rate leads to a larger change than adding self-gravity to the simulations. This may not hold true for models which have either a higher density inflow or a longer perturbation wavelength which enhances self-gravity. Additional models with different initial density values would be informative. In their cylindrical models, HSWK found that very massive slabs evolved in a manner similar to less massive slabs. The current results support this claim and can be further tested and verified for different cooling rates. A study of models with different inflow velocities would also be constructive. With one exception, the Cartesian models presented in this chapter use the same perturbation function. Simulations in which a sine function replaced the cosine function in the perturbation equation showed the same qualitative behavior, but no in-depth analysis was performed. Models with strong cooling lose the signature of the perturbation as the instability grows, so altering the perturbation function should have little effect, provided the wave number remains unchanged. Two dimensional models must ultimately give way to three dimensional models in order to accurately represent the systems under consideration. As work proceeds, additional physics must be added as well, including magnetic fields, heating processes, and obliquely colliding flows.

The strong dependence of the slab instability on the cooling rate casts doubt upon the utility of Vishniac's (1994) analytic description of the NTSI in an isothermal gas. However, it should be noted that despite the many differences among models with varying cooling rates, the growth rate for the slab displacement is similar in most cases. Attempts to find evidence for a linear growth phase to the NTSI have failed, upholding that aspect of Vishniac's theory. Furthermore, a higher wave number leads to a faster growth rate, as expected from theory. Many authors have noted that the isothermal limit is not a good representation of interstellar gas (e.g. HSWK, Vázquez-Semadeni et al. 1996). For a gas that can be described as polytropic, such that $P \propto \rho^{\gamma_e}$, the effective value of $\gamma$ for strongly cooling flows is less than unity, $\gamma_e < 1$. New theories are needed which take into account the high compressions afforded by realistic cooling rates in the ISM. The nonlinear nature of the instability makes the development of any such theory very difficult. Furthermore, because different phases of the ISM exhibit different heating and cooling processes, the behavior of the NTSI is expected to vary in different regions of the ISM.

The Cartesian simulations presented in this chapter show many similarities to previous simulations performed in cylindrical geometry. Models with low cooling rates exhibit morphologies very similar to the models of MK, even though the compression in the slab is much higher. I find no evidence of the NTSI in perturbed adiabatic slabs. This may be due to a lack of sufficient resolution or the result of having continuously accreting shocks. Further comparisons with previous work are reserved for the next chapter in which colliding flows in cylindrical geometry are considered.

# CHAPTER 5
# COLLIDING FLOWS IN CYLINDRICAL GEOMETRY

For studies of self-gravitating systems using two dimensional modeling, cylindrical geometry is preferable to Cartesian geometry. Azimuthal symmetry imparts a three dimensional nature to the simulations; clumps which form along the symmetry axis approximate spheres. Previous computational simulations of the NTSI and slab fragmentation (e.g. HWSK, SBP, KW) focussed on cylindrical geometry. In order to better compare new results with the previous studies, cylindrical models are performed with and without self-gravity. The formation of gravitationally collapsing clumps is investigated. Five groups of models are considered: models with free outer boundaries and full cooling, models with reflective outer boundaries and full cooling, models with free outer boundaries and reduced cooling, models with varying minimum temperatures, and models with a higher inflow velocity.

## 5.1 Models

In order to differentiate the cylindrical models from the Cartesian models, I use "disk" rather than "slab" to describe the shock-bounded object. The formation and subsequent instability of disks and slabs are very similar. Colliding gas flows give rise to a dense disk bounded by accretion shocks. If allowed to cool, the disk becomes very dense prior to the onset of instability. The physical characteristics for the cylindrical models are similar to those for the Cartesian models. Unless otherwise noted, the inflowing gas has the values $\rho_i = 10^{-21} g\, cm^{-3}$, $T_i = 100\, K$ (prior to the onset of cooling), and $v_i = \pm 5\, km\, s^{-1}$. The cell size is the same as that for the Cartesian models, $\Delta r = \Delta z = 5 \times 10^{15} cm$. The mass inside a cylinder with a radius of 97 cells and a height of 129 cells is $4.77 \times 10^{32}\,g = 0.24\,M_{\odot}$. Once the simulation begins, mass enters the grid through the horizontal boundaries at a rate of $7.39 \times 10^{20}\,g\,s^{-1}$. The symmetry axis is represented by a reflecting boundary on the left edge of the grid. The right edge of the grid has a free boundary allowing inflows and outflows.

The application of self-gravity in cylindrical coordinates is accomplished using the method described in chapter 2. Because of the geometry, gravity pulls material towards the symmetry axis. Along the symmetry axis, the radial component of the potential gradient is zero. The boundary values of the potential away from the symmetry axis are determined for each time step by explicitly summing the contributions from the annulus described by each cell. This procedure is more accurate than the method used for self-gravitating Cartesian models, but also requires far more computing time. The grid size for most models is kept rather small (97×129 cells) in order to keep the run times reasonable. Still, the grid has far higher resolution than the 25×50 grid used by HSWK.

Results are presented for models with two different cooling rates, $q = 1$ and $q = 0.3$. Also, a number of additional parameter variations are considered for the $q = 1$ models. More emphasis is placed on the $q = 1$ models since they implement the best cooling model available for simulating molecular cloud cores. As in the Cartesian models, the cooling is confined to within 50 cells of the disk. Simulations were performed for a wide range of perturbations, but only a few are chosen for detailed presentation. In order to examine the differences between a Cartesian and a cylindrical mesh, simulations which have the same perturbation function as the one used in chapter 4 (equation 4.2) are used. Other models considered in this chapter have a perturbation of the form

$$v_z = v_z + 0.01 v_i \sin(kr) \sin(\pi r/r_d) e^{-k|z-z_d|}, \tag{5.1}$$

where $r_d$ is the total radius of the disk (the spatial extent of the grid in the radial direction). The second sine term superimposes one-half of a sine wave ($0 < r/r_d < 1$) upon the perturbation in order to localize the perturbation to the center of the grid and minimize the initial growth along the boundaries. Since periodic boundary conditions are not used in the gravity solver, the perturbation function need not be strictly periodic. A half integer number of waves is excited across the grid so that both sine functions have their maxima at the grid center.

## 5.2 Results

When gas streams collide and are allowed to cool, a cold, dense disk forms that remains stable for a long time if left unperturbed. Figures (5.1) and (5.2) show the results of simulations performed on a 97×129 grid for the $q = 1$ and $q = 0.3$ cases, respectively, for simulations performed on a 97×129 grid. (In all plots of cylindrical models, the $r$ axis is shifted by one cell so that the symmetry axis does not lie along the plot axis.) The disks remain stable until $t \sim 1.4 \times 10^{13} s$. They do not last as long as the Cartesian models presented in the previous chapter. The disks are densest near the outer radial boundary due to the inflow of material, but they first go unstable along the reflective symmetry axis. Overall, the disk in the $q = 1$ model is denser than the disk in the $q = 0.3$ model. A stronger cooling mechanism inside the disk results in a lower thermal pressure, allowing a greater compression. A close look at figures (5.1) and (5.2) reveals that the onset of instability is signaled by the presence of high frequency ripples in the disks. For the $q = 1$ case, the ripples are largest near the symmetry axis and tend to diminish with increasing $r$. The ripples in the $q = 0.3$ case are more uniform in size throughout the disk. Ripples at large $r$ grow quickly enough to drive the disk unstable before the instability from the symmetry axis propagates outward.

The switch from Cartesian to cylindrical geometry causes the disk to evolve differently, even if all else is kept the same. The $q = 1$ and $q = 0.3$ models from

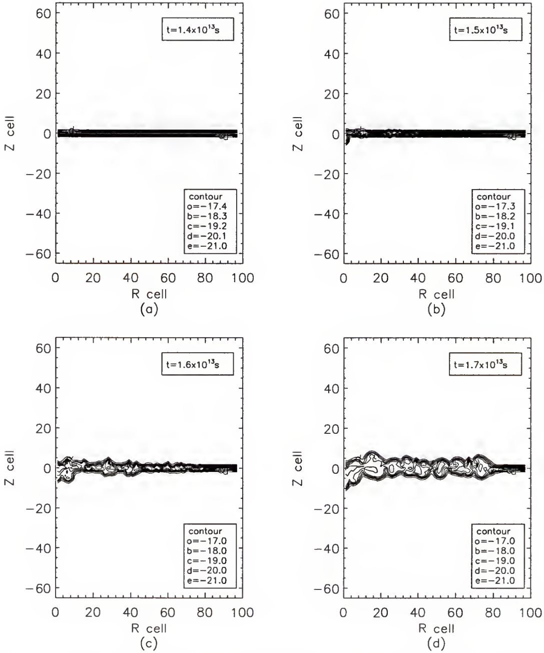

Figure 5.1: Onset of instability in an unperturbed $q = 1$ disk. Log$_{10}$ density contours are shown at times a)$1.4 \times 10^{13}s$; b)$1.5 \times 10^{13}s$; c)$1.6 \times 10^{13}s$; and d)$1.7 \times 10^{13}s$. An instability initially appears along the symmetry axis and then propagates outward.

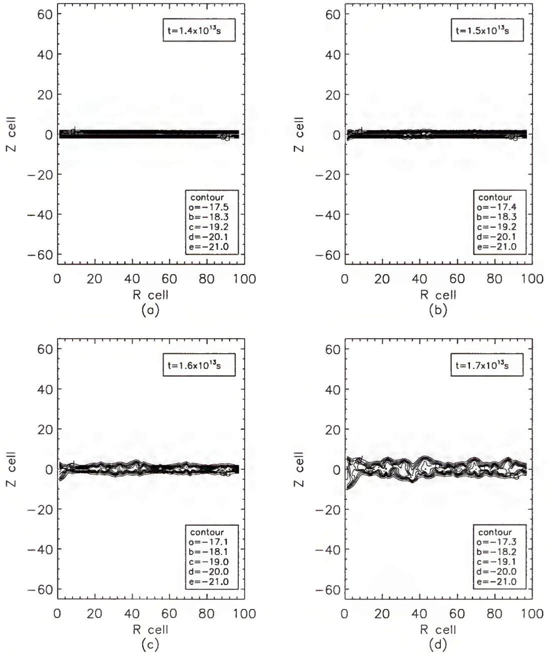

Figure 5.2: Onset of instability in an unperturbed $q = 0.3$ disk. Log$_{10}$ density contours are shown at times a)$1.4\times10^{13}s$; b)$1.5\times10^{13}s$; c)$1.6\times10^{13}s$; and d)$1.7\times10^{13}s$. The disk first goes unstable along the symmetry axis.

the previous chapter are reproduced on 129×129 cylindrical grids to demonstrate the changes. Figure (5.3) shows the development of the disk instability for a $q = 1$ disk perturbed at $5.0 \times 10^{12} s$. The perturbation function follows the cosine form (equation 4.2) used for the $q = 1$ Cartesian model (figure 4.6). The cylindrical and Cartesian models are similar in that both show the growth of secondary peaks throughout the disk. In the cylindrical version, the reflective symmetry axis behaves far differently than the outer boundary. The fastest growing peak is along the symmetry axis. A comparison of the density values once the disk is well evolved reveals additional differences. The density distribution at $t = 1.1 \times 10^{13} s$ is reproduced as a grayscale plot with overlaying velocity vectors in figure (5.4). Additional line contours are added to highlight the densest regions. The evolved disk has dense filaments throughout its interior. Also evident are several regions within the disk in which the density is lower than the initial density. The most striking difference between the cylindrical and Cartesian models is the appearance of a dense filament along the symmetry axis. The highest density in the filament (which is also the highest density anywhere on the grid) is $2270\rho_i$. This is the first evidence of a density higher than the density of an unperturbed disk at the same time. The density of an unperturbed slab at $1.1 \times 10^{13} s$ is $2120\rho_i$. In the Cartesian model (figure 4.13), the largest observed density at the same time is $1300\rho_i$. Clearly, a cylindrical grid leads to the geometric focusing of material towards the symmetry axis. Self-gravity is expected to further enhance the density growth along the axis.

A similar comparison is made between cylindrical and Cartesian models for the $q = 0.3$ case. The results for the cylindrical model are shown in figure (5.5). The cylindrical and Cartesian (figure 4.10) models evolve in similar manners. The perturbation wavelength is well preserved to late times. As in the cylindrical $q = 1$ case, the instability grows fastest along the symmetry axis in the cylindrical $q = 0.3$ model. However, the maximum density ($\rho = 1950\rho_i$) is found along the outer radial

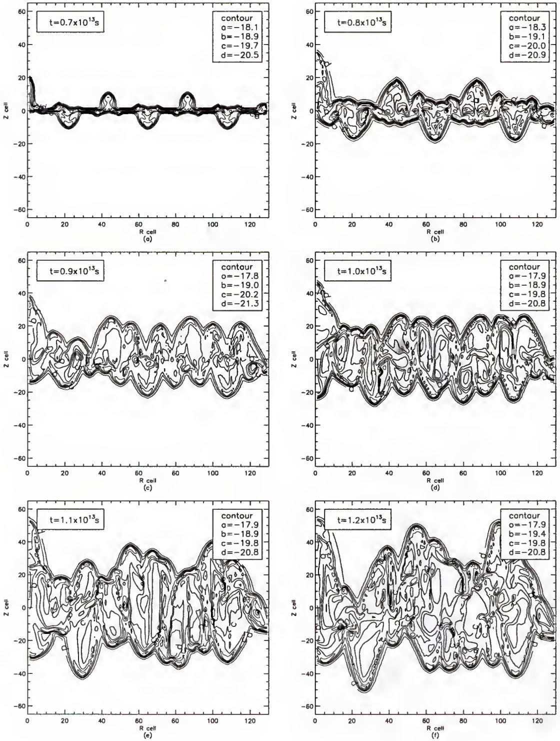

Figure 5.3: Instability growth for a $q = 1$ disk on a 129×129 grid. $\text{Log}_{10}$ density contours are shown at times a)$7.0 \times 10^{12}s$; b)$8.0 \times 10^{12}s$; c)$9.0 \times 10^{12}s$; d)$1.0 \times 10^{13}s$; e)$1.1 \times 10^{13}s$; and f)$1.2 \times 10^{13}s$. The time of perturbation is $5.0 \times 10^{12}s$.

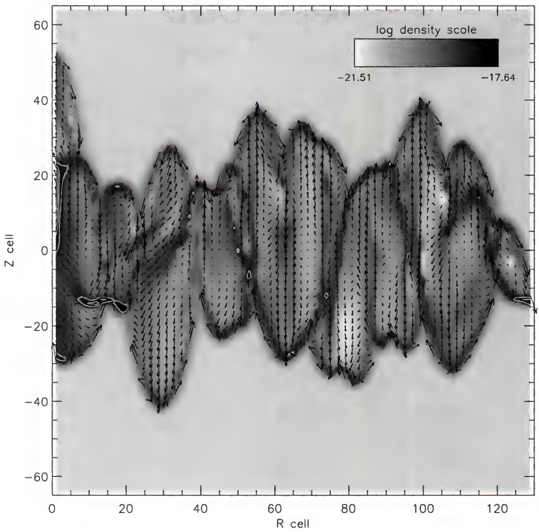

Figure 5.4: Perturbed disk morphology for a $q = 1$ model at $t = 1.1 \times 10^{13} s$. Velocity vectors are superimposed upon a grayscale image of $\log_{10}(\rho)$. Only vectors with a magnitude below $2 \times 10^5 cm\, s^{-1}$ are plotted. Regions not represented with vectors have flows of higher magnitude. Line contours highlight the densest regions.

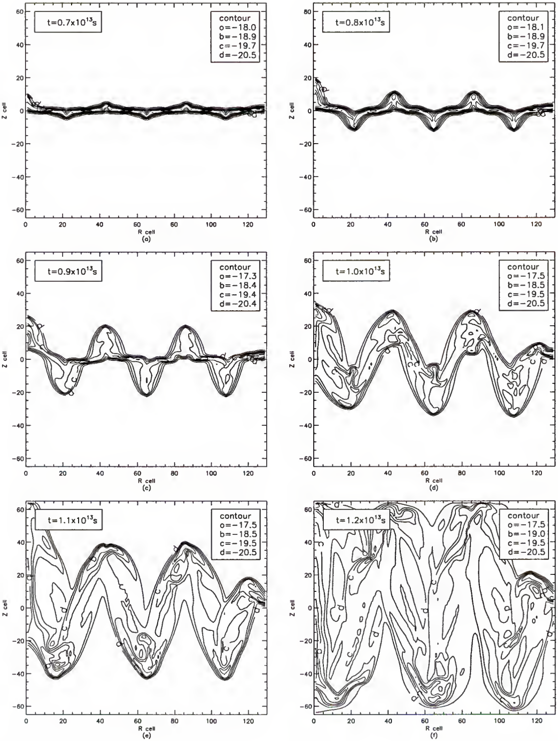

Figure 5.5: Instability growth for a $q = 0.3$ disk on a 129×129 grid. $\text{Log}_{10}$ density contours are shown at times a)$7.0 \times 10^{12}s$; b)$8.0 \times 10^{12}s$; c)$9.0 \times 10^{12}s$; d)$1.0 \times 10^{13}s$; e)$1.1 \times 10^{13}s$; and f)$1.2 \times 10^{13}s$. The time of perturbation is $5.0 \times 10^{12}s$.

boundary rather than in the filament which forms along the symmetry axis. Figure (5.6) shows the density distribution and velocity vectors at $t = 1.1 \times 10^{13} s$. The long filament along the symmetry axis has a maximum density of $594\rho_i$, far lower than that seen in the $q = 1$ model at the same time. The maximum density is located in the same place as seen in the Cartesian model, but the value is much higher. The tendency for material to move towards the symmetry axis may be preventing some material from flowing out of the grid, resulting in a larger density concentration. As in the Cartesian case, vortices are clearly seen within the interior of the disk.

### 5.2.1 Free Outer Boundaries and Full Cooling

Due to the long run times needed for the gravity solver, the bulk of the cylindrical simulations were performed on a smaller 97×129 grid. The perturbation function contains two sine terms as described by equation (5.1). The first set of models has a perturbation time of $5 \times 10^{12} s$. At the time of perturbation, the density along the symmetry axis is $945\rho_i$, but increases at large $r$ (figure 5.7) due to inflows along the outer boundary. The temperature distribution follows the opposite trend, since a higher density results in more cooling and hence lower temperatures. (The additional inflows arise very early when free boundaries allow outflows and inflows, regardless of the total extent of the grid. In the next subsection, I describe a series of models with reflective outer boundaries. The overall results are very similar.) The perturbation wavelength is $1.39 \times 10^{17} cm$; 3.5 full waves fit on the grid. The results for a non-gravitating $q = 1$ model are shown in figure (5.8). At early times, the largest growth is seen at the center of the grid where the maximum perturbation is applied. Secondary peaks develop early, but they do not mask the perturbation signature. Inflowing material is transferred along the peaks and into the interior, giving rise to dense filaments within the perturbed disk. Some of the material strikes a peak and moves towards the vertical boundaries, leading to outflows along the outer boundary. Figure (5.9) shows the density distribution and velocity flow within the disk

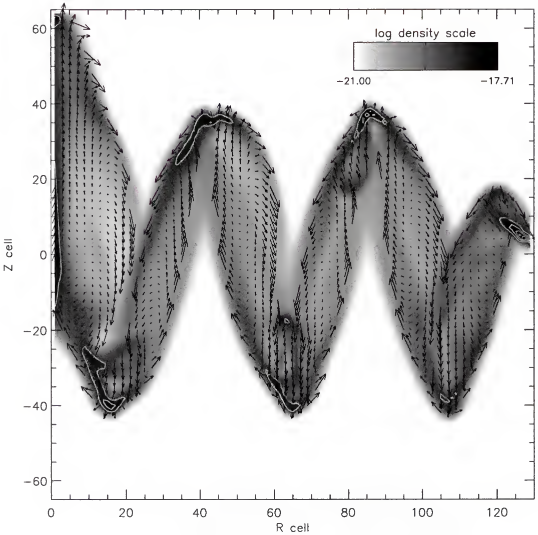

Figure 5.6: Perturbed disk morphology for a $q = 0.3$ model at $t = 1.1 \times 10^{13} s$. Only velocity vectors with a magnitude below $2 \times 10^5 cm\, s^{-1}$ are plotted. Line contours highlight the densest regions.

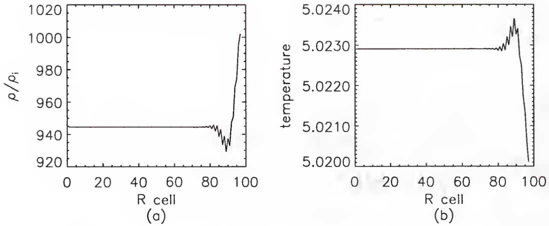

Figure 5.7: Radial density and temperature distributions for an unperturbed $q = 1$ disk at $5 \times 10^{12}s$.

at $t = 1.1 \times 10^{13}s$. The highest density ($\rho = 2930\rho_i$) is found in a filament along the symmetry axis. As seen in previous $q = 1$ models, the lowest density regions are found inside the disk. The internal flows are largely uni-directional, but some vorticity is present.

The perturbation wavelength ($\lambda = 1.39 \times 10^{17}cm$) is well below the critical wavelength for the collapse of a uniform sheet. From equation (4.4), the critical wavelength at the time of perturbation is $\lambda_c = 9.23 \times 10^{17}cm$ for $\rho = 945\rho_i$ and $T = 5\,K$. A few additional critical values are worth mentioning. The total diameter of the disk (accounting for symmetry) is $194 \times 5 \times 10^{15}cm = 9.7 \times 10^{17}cm$. The minimum density needed to drive the entire disk towards collapse if the perturbation wavelength were equal to the disk diameter is $\rho_c = 899\rho_i$. Clumps which form along the symmetry axis can be approximated as spheres. From the spherical Jeans equation (equation 2.38), the minimum density needed for catastrophic collapse within a single cell is $\rho_c = 5.48 \times 10^5\rho_i$. Collapse is assured should the density reach this value in any cell along the symmetry axis. (This is a conservatively high threshold for collapse.

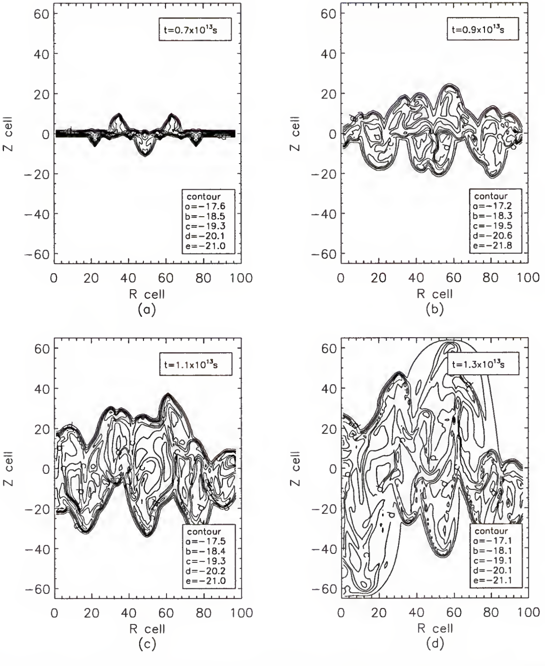

Figure 5.8: Instability growth for a $q = 1$ disk perturbed at $5 \times 10^{12} s$. Log$_{10}$ density contours are shown at times a)$7.0\times10^{12}s$; b)$9.0\times10^{12}s$; c)$1.1\times10^{13}s$; and d)$1.3\times10^{13}s$.

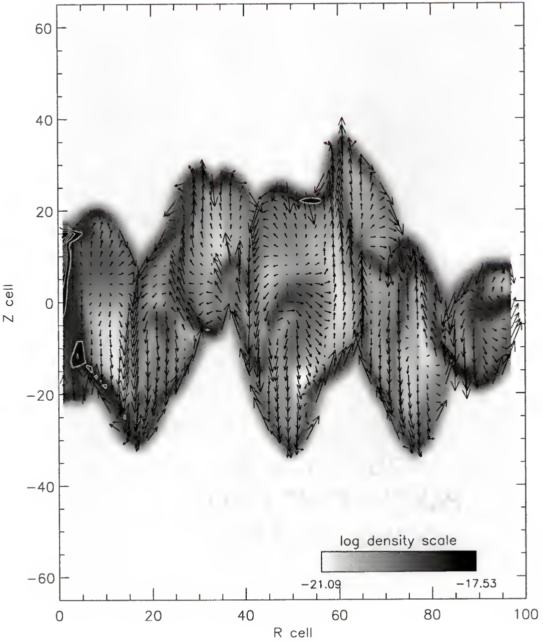

Figure 5.9: Morphology of a $q = 1$ disk at $1.1 \times 10^{13} s$. Only velocity vectors with a magnitude below $2 \times 10^{5} cm\, s^{-1}$ are plotted. Line contours highlight the densest regions.

Lower densities distributed across multiple cells can also lead to collapse.) For simulations which include self-gravity, the gravity solver is activated at the time of the perturbation. The density of the disk at that time is low enough that gravity does not have a substantial effect upon the instability right away. However, the inclusion of the gravity solver into the code introduces an additional source of numerical noise. The result is an additional disturbance which begins at the outer boundary and propagates towards the symmetry axis. Figure (5.10) shows the evolution of this disturbance. As the gravity induced disturbance propagates towards the axis, it gives rise to a density spike on either side of the expanded region (as shown for $t = 1.1 \times 10^{13} s$ in figure 5.11). The disturbance does not reach the symmetry axis prior to the onset of instability along the axis observed in the non-gravitating models. The growth of clumps along the axis is not greatly affected. The same phenomena are observed for the $q = 0.3$ gravitating models.

The disturbance which propagates inward in the gravitating models is overwhelmed when a perturbation is induced throughout. The instability growth for a self-gravitating $q = 1$ disk is shown in figure (5.12). The morphology is rather similar to that of the non-gravitating model at early times, but higher densities are soon observed along the symmetry axis. The disturbance seen in the unperturbed model (figure 5.10) is still present, but far denser clumps and filaments form along the axis. Figure (5.13) shows the density distribution and velocity flow within the disk at $t = 1.1 \times 10^{13} s$. At this time, the density along the symmetry axis has reached a maximum of $1.43 \times 10^4 \rho_i$. Little vorticity is seen within the disk.

Unlike in the Cartesian models, the addition of self-gravity to the cylindrical models has a profound effect. Without gravity, the perturbed disk grows in volume, and geometric focusing results in the formation of dense filaments along the symmetry axis. The densities within these filaments fluctuate as clumps contract and re-expand

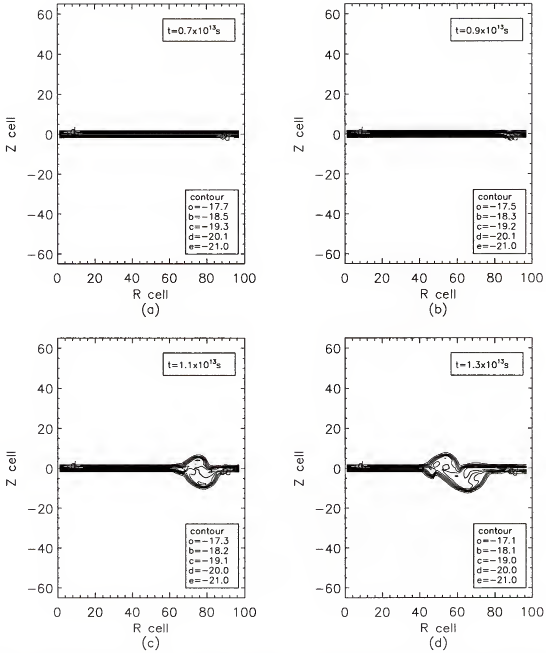

Figure 5.10: Evolution of an unperturbed $q = 1$ disk when gravity is activated at $5 \times 10^{12}s$. Log$_{10}$ density contours are shown at times a)$7.0 \times 10^{12}s$; b)$9.0 \times 10^{12}s$; c)$1.1 \times 10^{13}s$; and d)$1.3 \times 10^{13}s$.

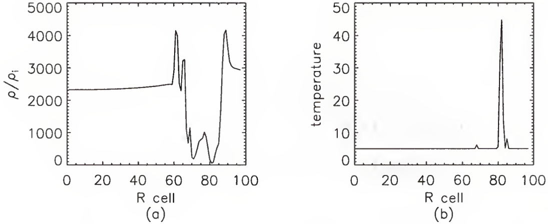

Figure 5.11: Radial density and temperature distributions for an unperturbed, self-gravitating $q = 1$ disk at $1.1 \times 10^{13}s$.

in response to the dynamic forces and their own internal pressure. Models with self-gravity are different in that long-lived, high density concentrations eventually form along the symmetry axis. Figure (5.14) contains plots of the maximum density along the symmetry axis versus time for the $q = 1$ models. The models represented in the figure are the unperturbed, non-gravitating case (solid line), the unperturbed, self-gravitating case (dotted line), the perturbed, non-gravitating case (dashed line), and the perturbed, self-gravitating case (dashed-dotted line). The quantity $\log_{10}(\rho/\rho_i)$ is plotted in order to show the non-gravitating and gravitating cases on the same graph. A value of $\log_{10}(\rho/\rho_i) = 5.74$ is needed to reach the critical density for the collapse of a single cell. The unperturbed, non-gravitating model accretes material at a nearly constant rate until the boundary induced instability starts to grow at $t \sim 1.4 \times 10^{13}s$. The maximum density in the perturbed, non-gravitating model oscillates on a short time scale, but never deviates from the unperturbed case by more than an order of magnitude. No collapsing clumps are observed. The gravitating models do produce collapsing clumps along the symmetry axis, but only after the disturbance induced by the gravity solver reaches the axis. This happens earlier in the model lacking an

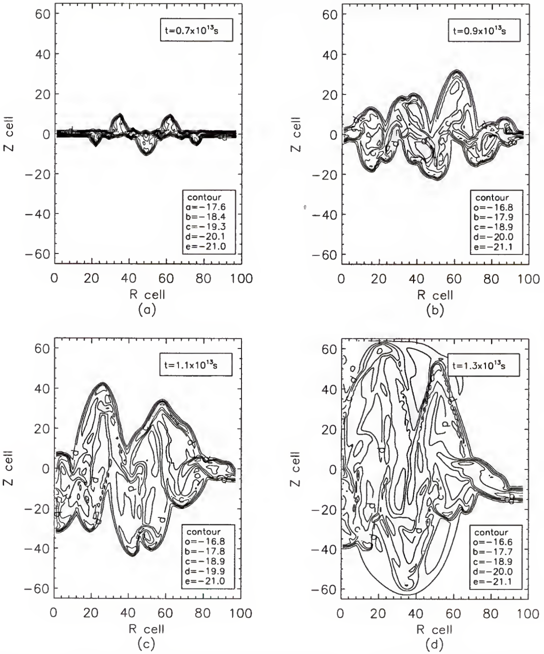

Figure 5.12: Instability growth for a self-gravitating $q = 1$ disk perturbed at $5 \times 10^{12} s$. $\mathrm{Log}_{10}$ density contours are shown at times a)$7.0 \times 10^{12} s$; b)$9.0 \times 10^{12} s$; c)$1.1 \times 10^{13} s$; and d)$1.3 \times 10^{13} s$. The gravity solver is switched on at the time of the perturbation.

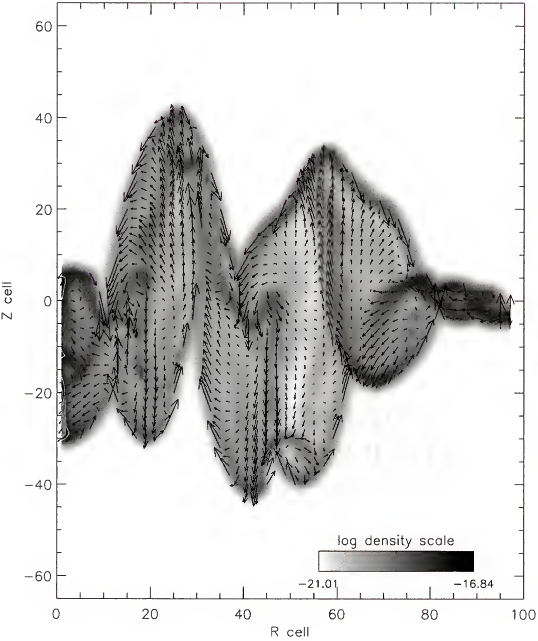

Figure 5.13: Morphology of a self-gravitating $q = 1$ disk at $1.1 \times 10^{13} s$. Only velocity vectors with a magnitude below $2 \times 10^5 cm\, s^{-1}$ are plotted. Line contours highlight the densest regions.

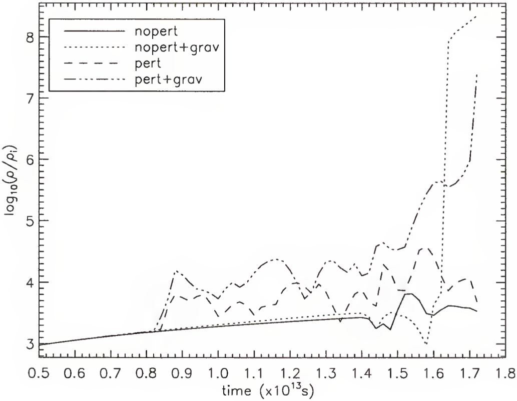

Figure 5.14: Maximum density along the symmetry axis versus time for models with a free outer boundary. Represented are the unperturbed, non-gravitating case (solid line), the unperturbed, self-gravitating case (dotted line), the perturbed, non-gravitating case (dashed line), and the perturbed, self-gravitating case (dashed-dotted line).

induced perturbation, as seen by the sudden density rise at $t \sim 1.6 \times 10^{13} s$. The perturbed, gravitating case shows oscillations similar to those in the perturbed, non-gravitating case before reaching the point of collapse. An upward trend in density is observed starting at $t \sim 1.4 \times 10^{13} s$, which would likely produce regions of local collapse even without the disturbance propagating inward from the outer boundary.

The use of cylindrical geometry permits a clear definition for the total mass in the simulation. For this purpose, the computational region is taken to be a cylinder with a radius of 97 cells ($R = 4.85 \times 10^{17}\, cm$) and a height of 129 cells ($Z = 6.45 \times 10^{17}\, cm$). As matter enters the grid through the top and bottom boundaries, the total mass increases at a constant rate given by

$$m(t) = \pi R^2 Z \rho_i \left(1 + \frac{2 v_i t}{Z}\right). \tag{5.2}$$

The total mass will also vary due to flows across the outer radial boundary. To determine the total mass at a given time, each cell is treated as an annulus, in a manner similar to that used in the gravity solver. The masses of all annuli are summed to arrive at the total. Figure (5.15a) shows the result for the non-gravitating $q = 1$ models. The change due to inflow from the horizontal boundaries is represented by the solid line. The total mass in the unperturbed model is always higher than the constant inflow value, indicating the presence of additional inflows along the outer boundary. When a perturbation is applied, some of the incoming flows are deflected towards the outer boundary, resulting in a net outflow. The total masses for the gravitating models as a function of time are plotted in figure (5.15b). As expected, gravity acts strongly to pull additional matter onto the grid.

### 5.2.2 Reflective Outer Boundaries and Full Cooling

When material is allowed to flow across the outer boundary, an additional inflow is established early in the simulation. This additional inflow is responsible for the rise in density at large $r$ shown in figure (5.7), as well as the higher than expected

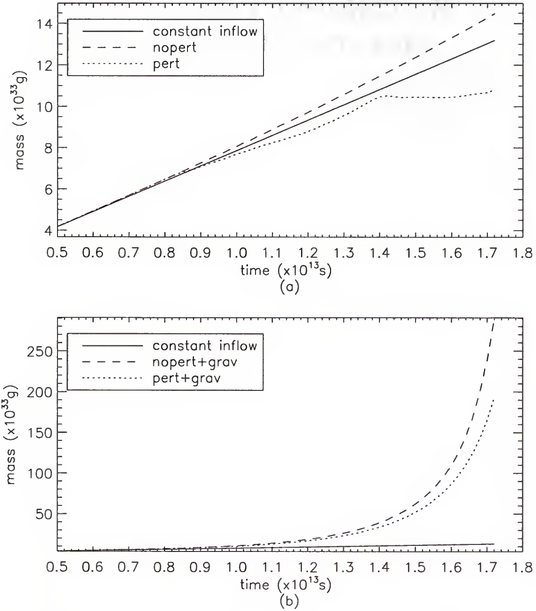

Figure 5.15: Total mass versus time for models with $v_i = 5\,km\,s^{-1}$. The total mass is compared to the mass due to the constant inflow from the horizontal boundaries for a)non-gravitating models; and b)gravitating models.

mass evident in an unperturbed disk. The disturbance seen in the gravitating models may be the same phenomenon amplified by the effects of self-gravity. In order to examine the effects of the flows along the outer boundary, the simulations were repeated with a reflective boundary condition along the outer boundary. This creates a more artificial situation in which no material is allowed to flow across the outer boundary. When left unperturbed, the disk remains stable for a long time. As in the outflow case, the disk first goes unstable along the symmetry axis at $t \sim 1.4 \times 10^{13} s$ (figure 5.16). The lack of inflows along the outer boundary allows instabilities to develop there sooner. At the time of perturbation ($t = 5 \times 10^{12} s$), the density and temperature are constant throughout the entire disk (figure 5.17).

Results for a perturbed disk are shown in figure (5.18). The instability growth proceeds in a very similar manner as that in the free boundary model. Even along the outer boundary the two models show very few differences. Away from the outer boundary, the models are nearly identical. The density distribution and velocity flow within the disk are shown for $t = 1.1 \times 10^{13} s$ in figure (5.19). The densest region ($\rho = 2940\rho_i$) is found along the symmetry axis. Switching from a free boundary to a reflective boundary has very little effect upon non-gravitating models.

Gravitating models with a reflective outer boundary deviate from the gravitating, free boundary models. The large mass increase shown in figure (5.15) for the gravitating outflow models is prevented by the reflective outer boundary. All models with a reflective outer boundary have total masses which increase at a constant rate due to the inflows from the horizontal boundaries. The total mass never decreases. As shown in figure (5.20), an unperturbed disk goes unstable sooner when gravity is activated. Instabilities first develop along both the symmetry axis and the outer boundary. Gravity pulls material towards the symmetry axis, resulting in a growing tenuous region near the outer boundary.

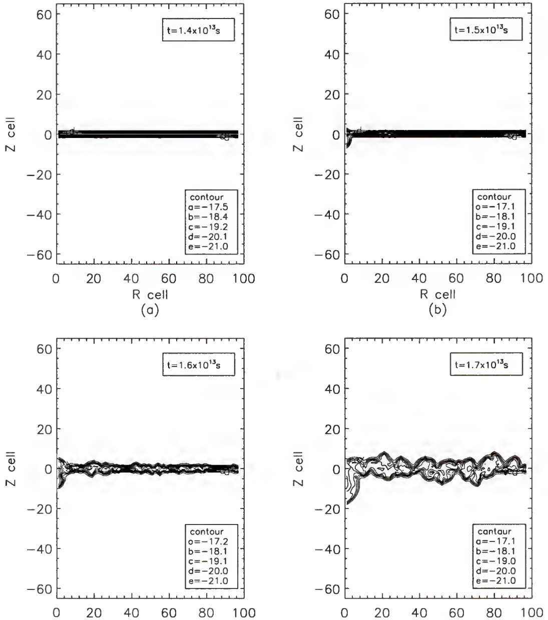

(a) (b) (c) (d)

Figure 5.16: Onset of instability in an unperturbed $q = 1$ disk with reflective outer boundary. $\text{Log}_{10}$ density contours are shown at times a)$1.4 \times 10^{13}s$; b)$1.5 \times 10^{13}s$; c)$1.6 \times 10^{13}s$; and d)$1.7 \times 10^{13}s$. The disk first goes unstable along the symmetry axis.

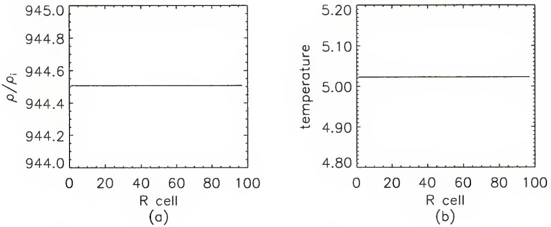

Figure 5.17: Radial density and temperature distributions for an unperturbed $q = 1$ disk with a reflective outer boundary at $5 \times 10^{12}s$.

Results for a perturbed, gravitating model are shown in figure (5.21). The reflective boundary model closely resembles the free boundary model during the early stages of the instability growth. However, the two models diverge at later times when the mass difference between them becomes considerable. By $t = 1.1 \times 10^{13}s$, the disk morphology for the reflective boundary model (figure 5.22) is substantially different from that in the free boundary model. The largest density observed for the reflective boundary model ($\rho = 3510\rho_i$) is considerably less than the largest density observed for the free boundary model ($\rho = 14,300\rho_i$). However, the formation of collapsing clumps does occur in the perturbed, gravitating model with a reflective outer boundary. As shown in figure (5.23), the reflecting boundary model reaches the critical density earlier than the free boundary model. The outflows induced in the perturbed free boundary model are prohibited in the reflective boundary model, so an earlier collapse is possible.

### 5.2.3 Free Outer Boundaries and Reduced Cooling

Simulations were performed for $q = 0.3$ models with a free outer boundary. Perturbed models again have a perturbation time of $5 \times 10^{12}s$, which is the same time

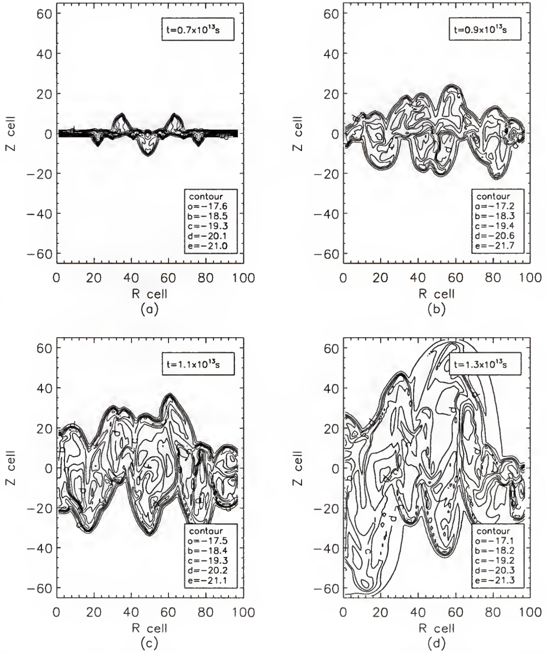

(a)

(b)

(c)

(d)

Figure 5.18: Instability growth for a $q = 1$ disk with a reflective outer boundary perturbed at $5 \times 10^{12} s$. Log$_{10}$ density contours are shown at times a)$7.0 \times 10^{12} s$; b)$9.0 \times 10^{12} s$; c)$1.1 \times 10^{13} s$; and d)$1.3 \times 10^{13} s$.

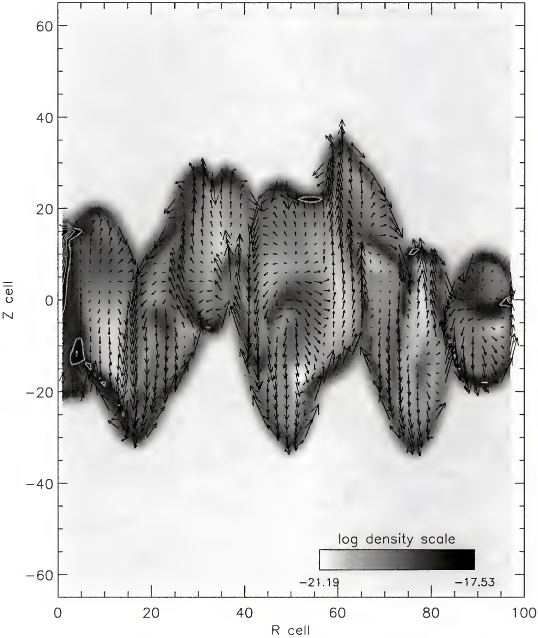

Figure 5.19: Morphology of a $q = 1$ disk with a reflective outer boundary at $1.1 \times 10^{13} s$. Only velocity vectors with a magnitude below $2 \times 10^5 cm\, s^{-1}$ are plotted. Line contours highlight the densest regions.

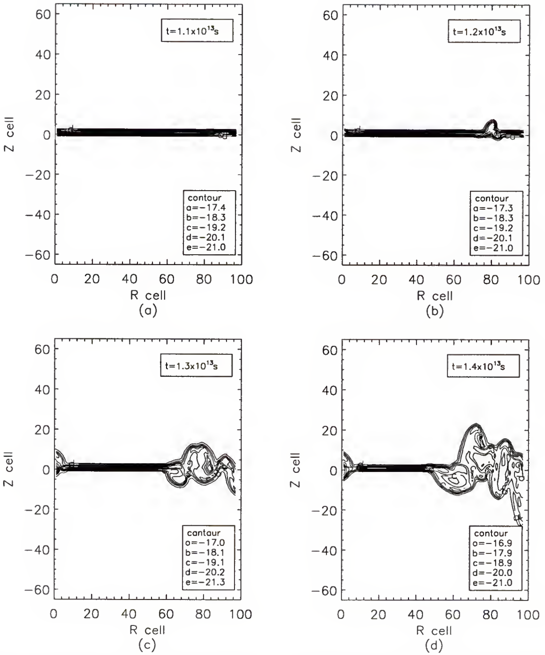

Figure 5.20: Evolution of an unperturbed $q = 1$ disk with a reflective outer boundary when gravity is activated at $5 \times 10^{12}s$. Log$_{10}$ density contours are shown at times a)$1.1 \times 10^{12}s$; b)$1.2 \times 10^{12}s$; c)$1.3 \times 10^{13}s$; and d)$1.4 \times 10^{13}s$.

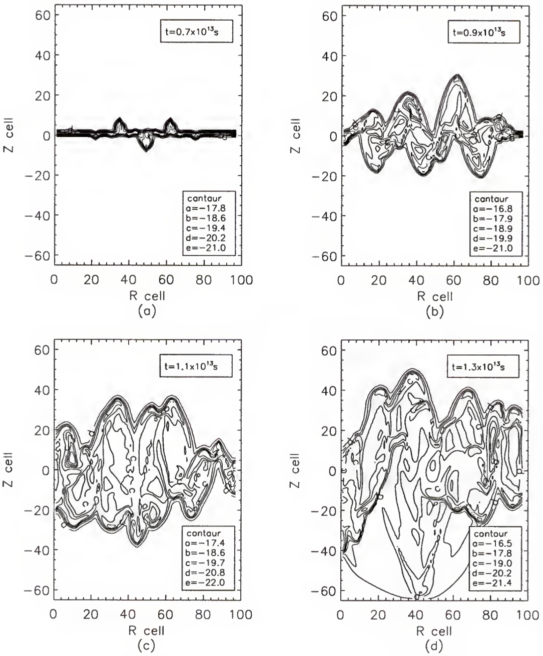

Figure 5.21: Instability growth for a self-gravitating $q = 1$ disk with a reflective outer boundary perturbed at $5 \times 10^{12}s$. Log$_{10}$ density contours are shown at times a)$7.0 \times 10^{12}s$; b)$9.0 \times 10^{12}s$; c)$1.1 \times 10^{13}s$; and d)$1.3 \times 10^{13}s$. The gravity solver is switched on at the time of the perturbation.

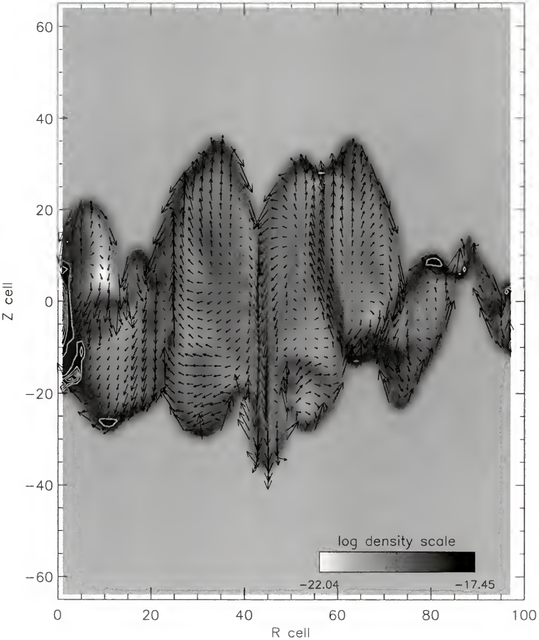

Figure 5.22: Morphology of a self-gravitating $q = 1$ disk with a reflective outer boundary at $1.1 \times 10^{13} s$. Only velocity vectors with a magnitude below $2 \times 10^5 cm\, s^{-1}$ are plotted. Line contours highlight the densest regions.

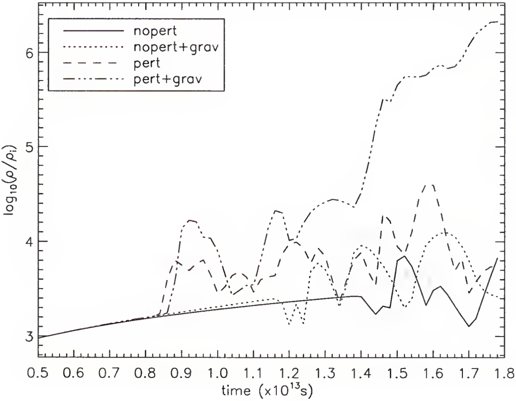

Figure 5.23: Maximum density along the symmetry axis for models with a reflective outer boundary. Represented are the unperturbed, non-gravitating case (solid line), the unperturbed, self-gravitating case (dotted line), the perturbed, non-gravitating case (dashed line), and the perturbed, self-gravitating case (dashed-dotted line).

that gravity is activated. Figure (5.24) shows the instability growth for a perturbed, non-gravitating $q = 0.3$ model. At early times, the disk morphology resembles the Cartesian $q = 0.3$ model and the low resolution models of KW. The disk thickness increases at a quicker pace than that in the $q = 1$ model. The extended disk fills up the entire grid in a relatively short time, making further analysis difficult. The morphology is shown at $t = 1.1 \times 10^{13}s$ in figure (5.25). A single massive ($\rho = 1.32 \times 10^4 \rho_i$) clump has formed along the symmetry axis. The velocity vectors inside the disk show that much of the material flow is concentrated towards that dense clump. However, no evidence for the formation of collapsing clumps is seen.

The self-gravitating, $q = 0.3$ model results in a dense clump being formed. The instability growth is shown in figure (5.26). Little difference from the non-gravitating model is seen, even at late times. Definitive statements for either case are difficult to make due to the interaction of the perturbed disk with the boundaries. The density distribution for the self-gravitating $q = 0.3$ model at $t = 1.1 \times 10^{13}s$ is shown in greater detail in figure (5.27). The similarity to the non-gravitating case is striking. Little vorticity is seen, and the highest density ($\rho = 1.50 \times 10^4 \rho_i$) is found in a clump along the symmetry axis. No clear evidence of a collapsing clump along the symmetry axis is seen until the gravity induced disturbance reaches the axis.

In all models considered, dense filaments arise along the symmetry axis. The densest regions are clumps within these filaments. The maximum clump densities at $t = 1.1 \times 10^{13}s$ are listed in Table (5.1). Gravity results in denser clumps in the $q = 1$ models, but not in the $q = 0.3$ case. The high density achieved in the non-gravitating $q = 0.3$ model is an oddity. The density appears to increase very quickly once the perturbed disk has expanded enough to reach the top and bottom boundaries of the grid. When a shock lies very close to one of the inflow boundaries, the inflowing gas has little or no time to cool. The result is a lower Mach number for the gas as it hits the shock. The incoming gas is thus more likely to deflect off of the disk than

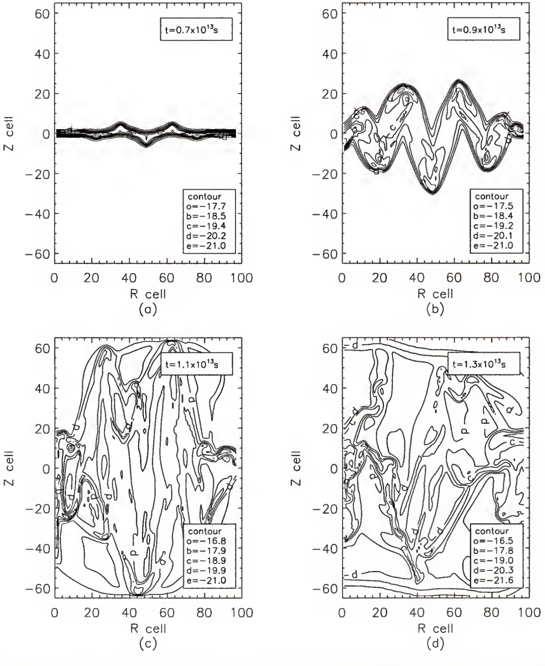

Figure 5.24: Instability growth for a $q = 0.3$ disk perturbed at $5 \times 10^{12}s$. $\mathrm{Log}_{10}$ density contours are shown at times a)$7.0 \times 10^{12}s$; b)$9.0 \times 10^{12}s$; c)$1.1 \times 10^{13}s$; and d)$1.3 \times 10^{13}s$.

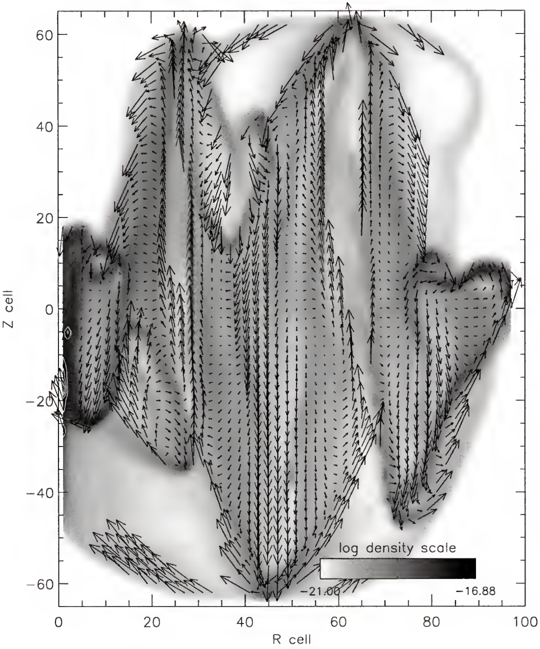

Figure 5.25: Morphology of a $q = 0.3$ disk at $1.1 \times 10^{13} s$. Only velocity vectors with a magnitude below $2.5 \times 10^5 cm\, s^{-1}$ are plotted. Line contours highlight the densest regions.

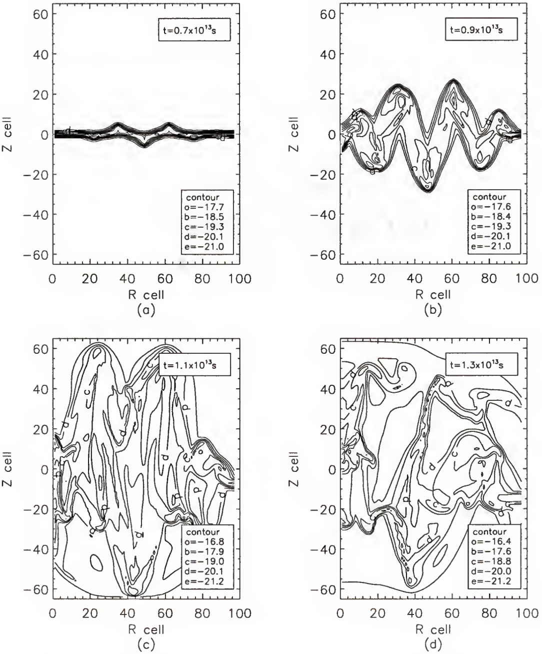

Figure 5.26: Instability growth for a self-gravitating $q = 0.3$ disk perturbed at $5 \times 10^{12}s$. Log$_{10}$ density contours are shown at times a)$7.0 \times 10^{12}s$; b)$9.0 \times 10^{12}s$; c)$1.1 \times 10^{13}s$; and d)$1.3 \times 10^{13}s$. The gravity solver is switched on at the time of the perturbation.

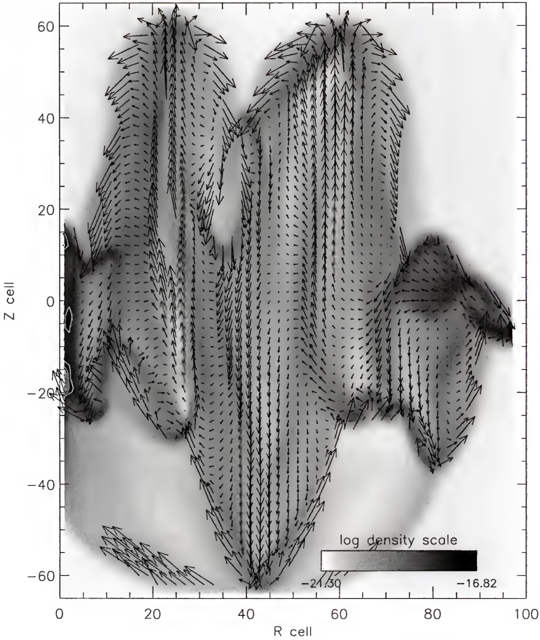

Figure 5.27: Morphology of a self-gravitating $q = 0.3$ disk at $1.1 \times 10^{13} s$. Only velocity vectors with a magnitude below $2.5 \times 10^5 cm\, s^{-1}$ are plotted. Line contours highlight the densest regions.

Table 5.1: Maximum densities at $t = 1.1 \times 10^{13} s$

| $q$ | gravity | outer boundary | $\max(\rho/\rho_i)$ | position $(r, z)$ |
|---|---|---|---|---|
| 1.0 | off | free | $2.93 \times 10^3$ | (0,15) |
| 1.0 | on | free | $1.43 \times 10^4$ | (0,-28) |
| 1.0 | off | reflective | $2.94 \times 10^3$ | (0,15) |
| 1.0 | on | reflective | $3.51 \times 10^3$ | (0,-3) |
| 0.3 | off | free | $1.32 \times 10^4$ | (0,-17) |
| 0.3 | on | free | $1.50 \times 10^4$ | (0,-19) |

compress or penetrate it. Larger grids are needed in order to remove the uncertainty created by the interaction of material with the grid boundaries.

### 5.2.4 Different Minimum Temperatures

The differences seen between the $q = 1$ and $q = 0.3$ models demonstrate the importance of the cooling rate in determining how the disks evolve. For a given cooling rate, the thermodynamic behavior of the gas can be altered by changing the minimum allowed temperature. All of the models presented earlier allow a minimum temperature of $T_{min} = 5\,K$. The $q = 1$, non-gravitating model with a free outer boundary was repeated with $T_{min} = 3\,K$ and $T_{min} = 10\,K$. The results for $T_{min} = 3\,K$ are shown in figure (5.28). The lower temperature threshold results in the faster growth of the NTSI and the earlier fragmentation of the disk. Throughout most of the lifetime of the disk, clumps along the symmetry axis have higher densities than those in the $T_{min} = 5\,K$ case. Figure (5.29) shows the density distribution and velocity vectors at $t = 1.1 \times 10^{13} s$. At that time, the maximum density is $7648\rho_i$, more than twice that in the $T_{min} = 5\,K$ case at that time.

Results for the $T_{min} = 10\,K$ model (figure 5.30) bear a greater resemblance to the $T_{min} = 5\,K$ case. The growth rate of the instability is similar for both models. However, the structures within the perturbed disks are different. Figure (5.31) shows the density distribution and velocity vectors at $t = 1.1 \times 10^{13} s$ for the $T_{min} = 10\,K$ model. The disk interior has far fewer dense filaments than in the $T_{min} = 5\,K$ case. Less vorticity is apparent as well. In fact, the structure within the $T_{min} = 10\,K$ disk

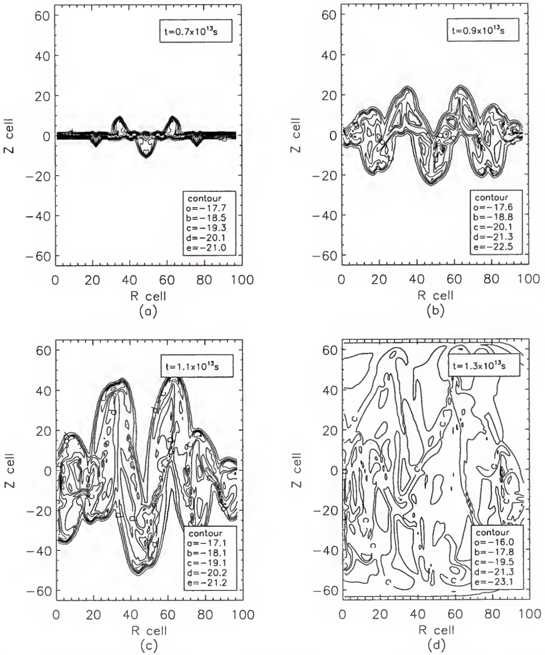

Figure 5.28: Instability growth for a model with $T_{min} = 3\,K$. Log$_{10}$ density contours are shown at times a)$7.0 \times 10^{12} s$; b)$9.0 \times 10^{12} s$; c)$1.1 \times 10^{13} s$; and d)$1.3 \times 10^{13} s$. The time of perturbation is $5.0 \times 10^{12} s$.

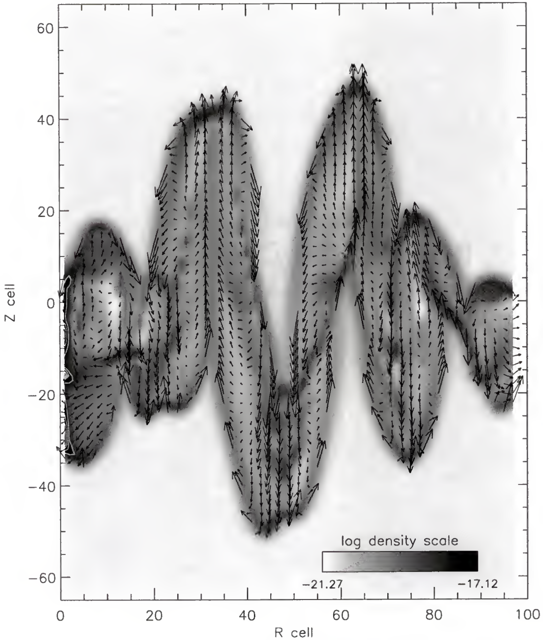

Figure 5.29: Morphology of a perturbed disk with $T_{min} = 3\,K$ at $1.1 \times 10^{13} s$. Only velocity vectors with a magnitude below $2 \times 10^{5} cm\,s^{-1}$ are plotted. Line contours highlight the densest regions.

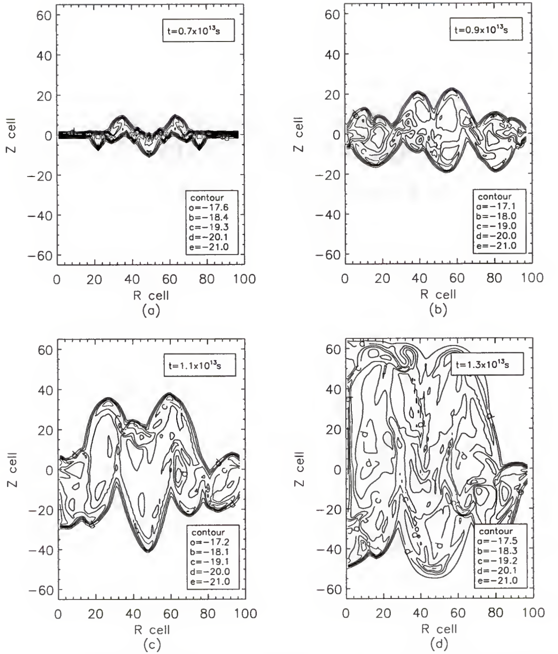

(a) (b) (c) (d)

Figure 5.30: Instability growth for a model with $T_{min} = 10\,K$. Log$_{10}$ density contours are shown at times a)$7.0 \times 10^{12}s$; b)$9.0 \times 10^{12}s$; c)$1.1 \times 10^{13}s$; and d)$1.3 \times 10^{13}s$. The time of perturbation is $5.0 \times 10^{12}s$.

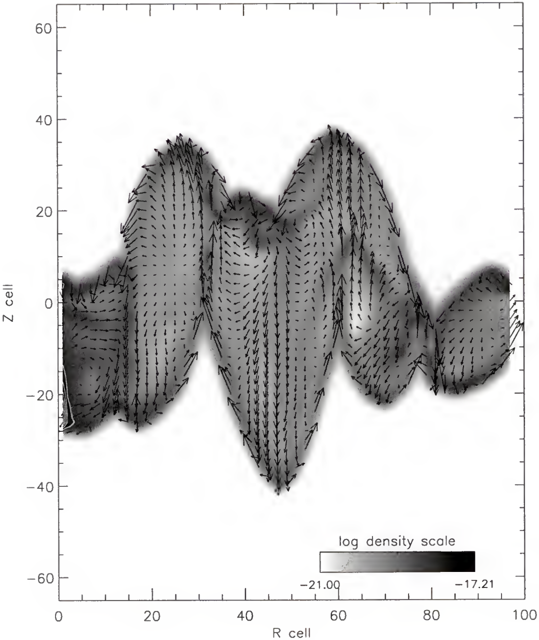

Figure 5.31: Morphology of a perturbed disk with $T_{min} = 10\,K$ at $1.1 \times 10^{13} s$. Only velocity vectors with a magnitude below $2 \times 10^5 cm\,s^{-1}$ are plotted. Line contours highlight the densest regions.

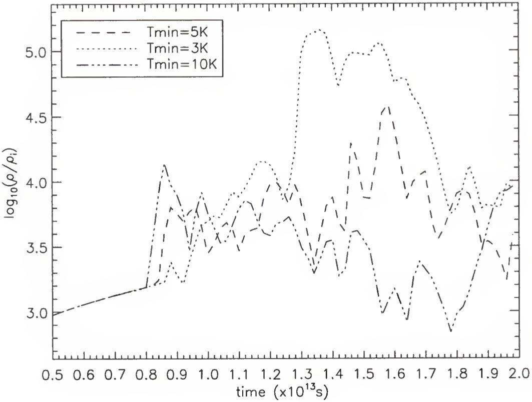

Figure 5.32: Maximum density along the symmetry axis versus time for perturbed models with varying $T_{min}$. Represented are models with $T_{min} = 5\,K$ (dashed line), $T_{min} = 3\,K$ (dotted line), and $T_{min} = 10\,K$ (dashed-dotted) line.

matches that seen in the $q = 0.3$ disk fairly well. The maximum density ($\rho = 6183\rho_i$) is greater than that seen in the $T_{min} = 5\,K$ model. However, as shown in figure (5.32), at most times the maximum density along the symmetry axis is lower when $T_{min} = 10\,K$ than when $T_{min} = 5\,K$. As expected, the lowest minimum temperature leads to the highest density at most times. The three models represented in figure (5.32) were perturbed at the same time. The model with the highest minimum temperature was the first to develop dense clumps along the symmetry axis, but these clumps were short lived and the maximum density ultimately fell. The model with the lowest minimum temperature was the last to form a dense clump along the axis, but the clump achieved a higher density and persisted for a longer time.

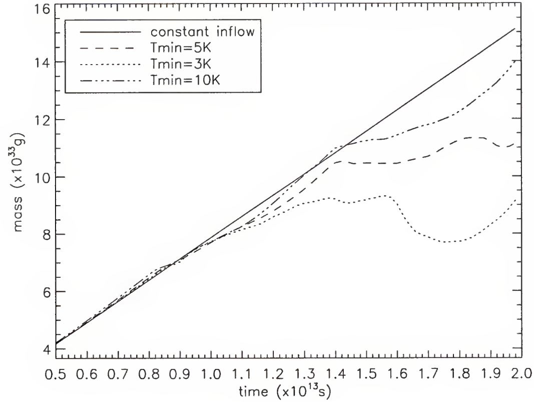

Figure 5.33: Total mass versus time for perturbed models with varying $T_{min}$. The total mass is compared to the mass due to the constant inflow from the horizontal boundaries for models with $T_{min} = 5\,K$, $T_{min} = 3\,K$, and $T_{min} = 10\,K$.

Changing the minimum temperature also has an effect upon the total mass within the grid. Figure (5.33) shows how the total mass changes over time for the three models. All three models result in net outflows of material across the outer boundary, with the $T_{min} = 3\,K$ model showing the largest loss of mass.

### 5.2.5 Higher Initial Velocities

One of the most important parameters in any of these models is the Mach number of the incoming flows. Very fast flows lead to shocks with a higher compression, perhaps assisting in the formation of clumps exceeding the critical density. However, fast flows are also more likely to disrupt and disperse dense clumps and thus stop the formation of collapsing clumps. As noted in the previous chapter, a higher cooling rate results in a higher Mach number for the flows as they impact the disk. This may account for some of the differences observed between the $q = 1$ and $q = 0.3$ models. I leave a detailed comparison of colliding flows of varying speed for future work. Here, I provide an introduction by considering a sequence of models for which $v_i = 7.5\,km\,s^{-1}$. The NTSI is driven in part by energy transfer from the supersonic flows to the disk. Since the energy of the flows increases with the square of the velocity, even a modest increase in velocity should lead to a much faster growth of the NTSI.

Aside from the initial velocity, the models are initialized in the same way as the $q = 1$, $T_{min} = 5\,K$ models with free outer boundaries. Because of the higher velocity, the flows reach the disk in less time. Thus, they have less time to cool prior to the shock. The temperature of the flows when they reach the unperturbed disk is $51\,K$. The sound speed is $0.545\,km\,s^{-1}$, resulting in a Mach number of 13.8. (The Mach number for the $q = 1$ models with $v_i = 5\,km\,s^{-1}$ is 10.4.) Instabilities within the disk develop rapidly in an unperturbed disk when the inflow velocity is high (figure 5.34). The disk first goes unstable along the symmetry axis, and by $8 \times 10^{12}s$ instabilities have developed everywhere. An early perturbation time of $3 \times 10^{12}s$ is used. The density within the disk at that time is $848\rho_i$, just a bit less than that for the slower inflow models. The evolution of the perturbed disk is shown in figure (5.35). The NTSI grows quickly, so Kelvin-Helmholtz instabilities within the disk have little time to develop. Few secondary peaks are evident, and the perturbation signature is preserved. A closer look at the density and velocity distributions within the disk at $t = 7.0 \times 10^{12}s$ is provided in figure (5.36). A dense clump ($\rho = 13,600\rho_i$) is found along the symmetry axis at a position far above the initial location of the disk.

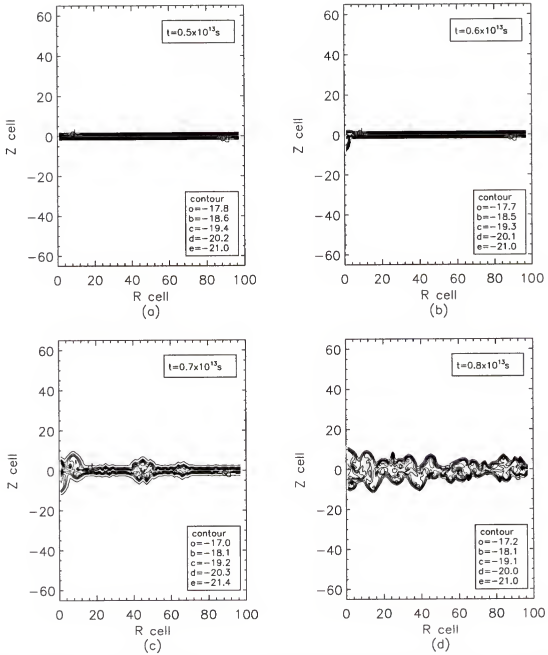

Figure 5.34: Onset of instability in an unperturbed disk with $v_i = 7.5\,km\,s^{-1}$. Log$_{10}$ density contours are shown at times a)$5.0 \times 10^{12}s$; b)$6.0 \times 10^{12}s$; c)$7.0 \times 10^{12}s$; and d)$8.0 \times 10^{12}s$.

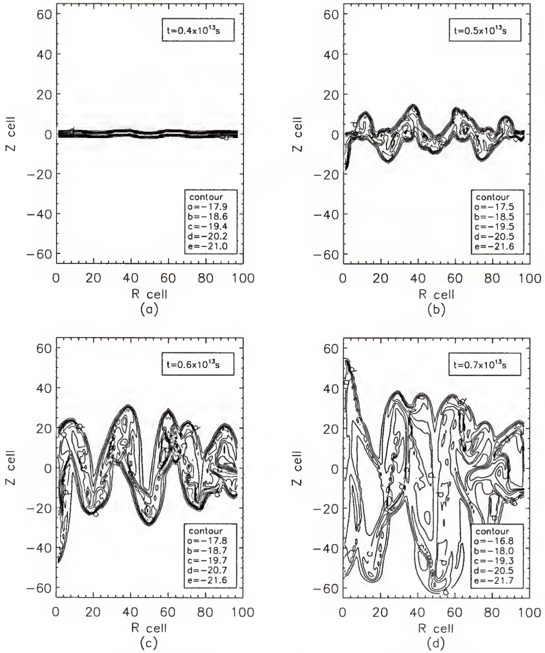

Figure 5.35: Evolution of a disk with $v_i = 7.5\,km\,s^{-1}$ perturbed at $3 \times 10^{12}s$. Log$_{10}$ density contours are shown at times a)$4.0 \times 10^{12}s$; b)$5.0 \times 10^{12}s$; c)$6.0 \times 10^{12}s$; and d)$7.0 \times 10^{12}s$.

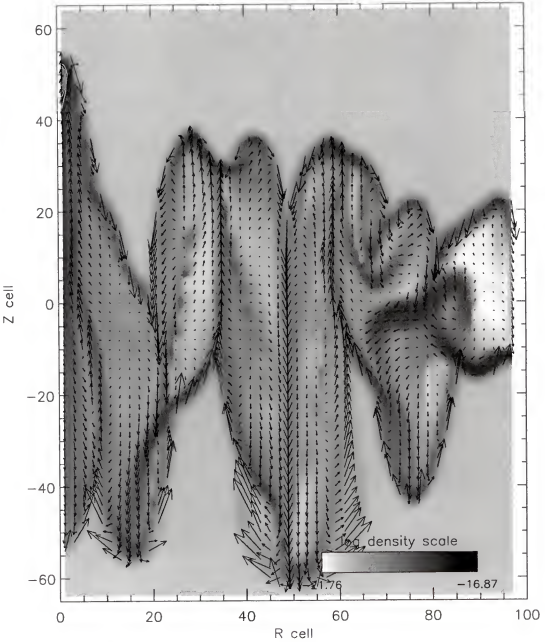

Figure 5.36: Morphology of a perturbed disk with $v_i = 7.5\,km\,s^{-1}$ at $7.0 \times 10^{12} s$. Only velocity vectors with a magnitude below $5 \times 10^5 cm\,s^{-1}$ are plotted. Line contours highlight the densest regions.

When the gravity solver is activated at $3 \times 10^{12} s$, an unperturbed disk again develops an instability along the symmetry axis before the rest of the disk (figure 5.37). The gravity enhanced disturbance evident in the previous models appears again, but not until after the instability along the axis. The fact that perturbations grow very rapidly without gravity limits the effect of gravity upon the growth of the NTSI. The evolution of a self-gravitating, perturbed disk is shown in figure (5.38). Little difference from the non-gravitating model is seen, although the NTSI has a slightly lower growth rate for the gravitating disk. The density and velocity distributions at $t = 7.0 \times 10^{12} s$ for the gravitating disk are shown in figure (5.39). As in the non-gravitating model, the densest clump ($\rho = 18,100 \rho_i$) is displaced from the original collision midplane. Adding self-gravity to the simulation does not lead to large density enhancements along the symmetry axis in the time allowed by the simulations. As shown in figure (5.40), the growth of clumps along the axis in both the unperturbed and perturbed models are not greatly altered by the addition of gravity. However, the total mass on the grid is greatly affected by gravity (figure 5.41). Unlike the models with $v_i = 5\, km\, s^{-1}$, the non-gravitating, perturbed model results in a net mass inflow along the outer boundary. This inflow is actually diminished when gravity is added. The results from the $v_i = 7.5\, km\, s^{-1}$ models demonstrate that different time resolutions are needed to study effectively models with different flow speeds.

## 5.3 Discussion

The main conclusion of the previous chapter, that cooling plays a controlling role in driving the evolution of the NTSI, also pertains to models performed with cylindrical geometry. Models with strong cooling tend to develop secondary peaks not seen in models with diminished cooling rates. The models with lower cooling rates again resembled the low resolution models of KW. However, since KW did not include self-gravity in their calculations, they were unable to speculate as to the

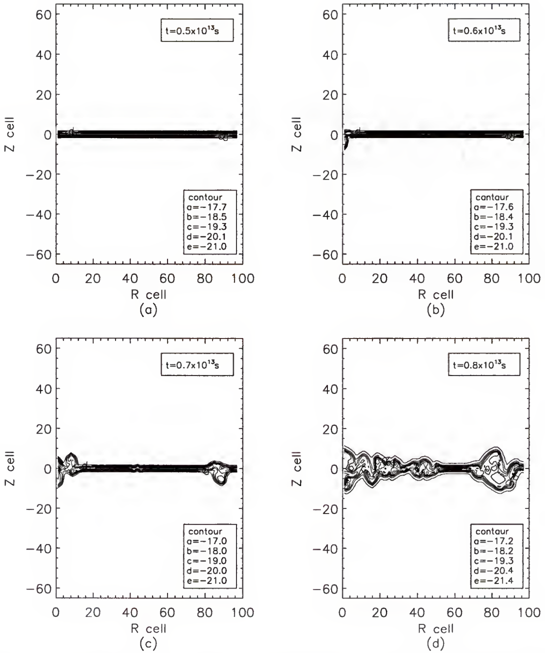

Figure 5.37: Evolution of an unperturbed disk with $v_i = 7.5\,km\,s^{-1}$ when gravity is activated at $3 \times 10^{12}s$. $\mathrm{Log}_{10}$ density contours are shown at times a)$5.0 \times 10^{12}s$; b)$6.0 \times 10^{12}s$; c)$7.0 \times 10^{12}s$; and d)$8.0 \times 10^{12}s$.

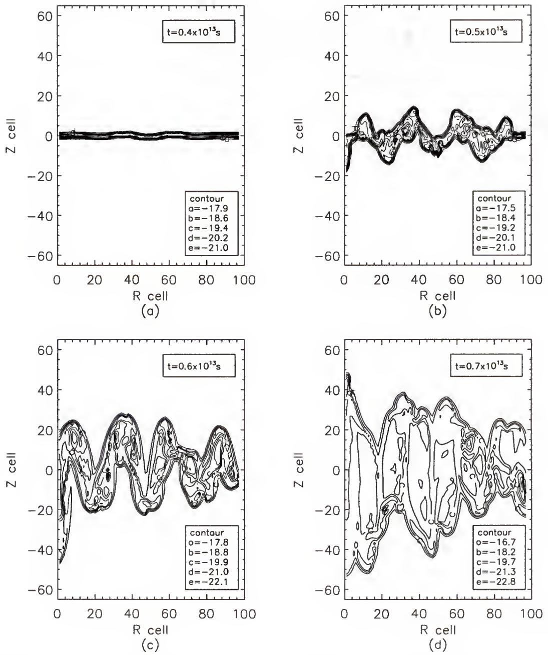

(a) (b) (c) (d)

Figure 5.38: Evolution of a self-gravitating disk with $v_i = 7.5\,km\,s^{-1}$ perturbed at $3 \times 10^{12}s$. $\mathrm{Log}_{10}$ density contours are shown at times a)$4.0 \times 10^{12}s$; b)$5.0 \times 10^{12}s$; c)$6.0 \times 10^{12}s$; and d)$7.0 \times 10^{12}s$. The gravity solver is activated at the time of the perturbation.

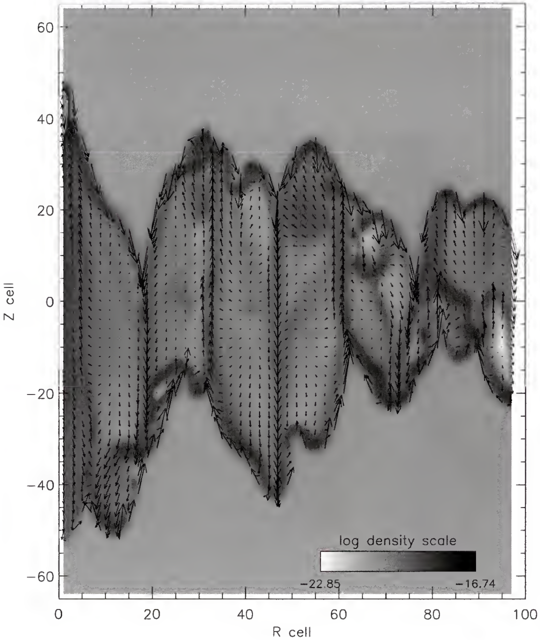

Figure 5.39: Morphology of a self-gravitating, perturbed disk with $v_i = 7.5\,km\,s^{-1}$ at $7.0 \times 10^{12} s$. Velocity vectors are superimposed upon a grayscale image of $\log_{10}(\rho)$. Only velocity vectors with a magnitude below $5 \times 10^5 cm\,s^{-1}$ are plotted. Line contours highlight the densest regions.

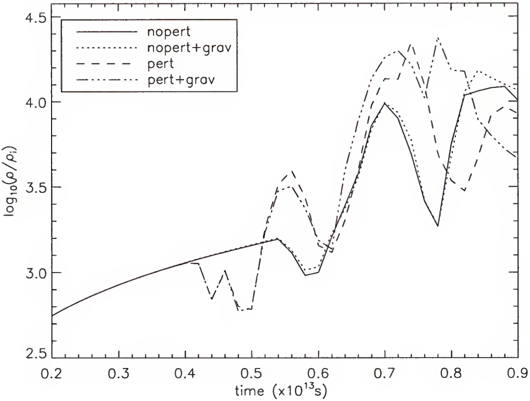

Figure 5.40: Maximum density along the symmetry axis versus time for models with $v_i = 7.5\,km\,s^{-1}$. Represented are the unperturbed, non-gravitating case (solid line), the unperturbed, self-gravitating case (dotted line), the perturbed, non-gravitating case (dashed line), and the perturbed, self-gravitating case (dashed-dotted line).

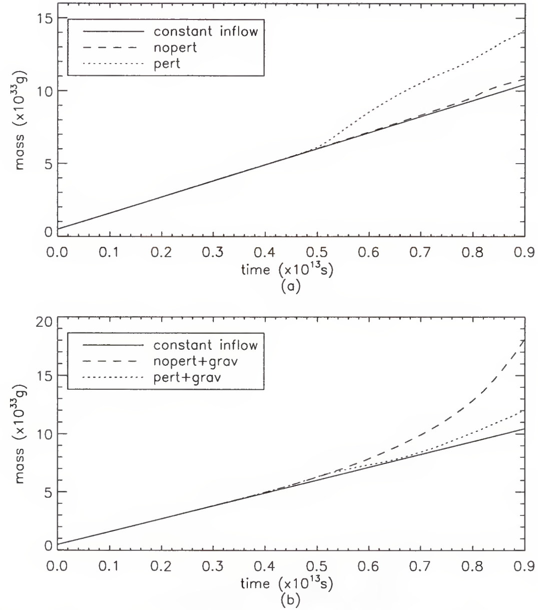

Figure 5.41: Total mass versus time for models with $v_i = 7.5\, km\, s^{-1}$. The total mass is compared to the mass due to the constant inflow from the horizontal boundaries for a)non-gravitating models; and b)gravitating models.

formation of collapsing clumps. Cylindrical models differ from the Cartesian models in that geometric focusing (and gravity, if applied) leads to the development of dense filaments along the symmetry axis. Models with lower cooling rates appear to be better at developing dense clumps approaching collapse, but this result is clouded by the boundary effects inherent in a grid code. Further studies with larger grids are in order. Altering the minimum temperature allowed in the simulations does not alter the general behavior of non-gravitating disks. However, the changes in total mass and maximum clump density over time do vary amongst the models. This is further evidence of the sensitive dependence of the NTSI upon the thermodynamic properties of the gas.

In this chapter, attention was given to the effects of altering the nature of the outer radial boundary. When flows are allowed to pass through the outer boundary, unperturbed models show an additional inflow prior to the onset of instability. Perturbed models (when $v_i = 5\,km\,s^{-1}$) exhibit a net outflow of material unless gravity is included. Gravity pulls a large amount of material onto the grid through the outer boundary. When a reflective boundary is used to prohibit flows across the outer boundary, the results near the symmetry axis are largely unchanged. In fact, collapsing clumps arise a bit sooner since no material escapes the grid once the disk is perturbed.

Distinct clumps of high density are seen in all perturbed models. These results agree with observations of dense filaments with embedded clumps in the Orion molecular cloud 1 (Murata et al. 1990) and the Taurus molecular cloud (Ungerechts and Thaddeus 1987). The upward trend in density among perturbed, gravitating models may be inferred to lead to collapsing regions. (The use of either higher inflow densities or larger cell sizes would likely remove all doubt.) Thus, the interaction of supersonic flows does give rise to structures conducive to star formation, as HWSK concluded. This has clear implications for the theory of triggered or sequential star formation (Elmegreen and Lada 1977). A first generation of massive stars generates winds and shocks capable of spurring the creation of further generations of lower mass stars.

Both the cylindrical and Cartesian models suffer from several limitations. In all models, the gas was treated as purely molecular; phase transitions were not allowed. Furthermore, the cooling rates were determined by NLM for fully shielded (high extinction) molecular clouds; no photodissociation by UV radiation was allowed. Non-shielded regions would have different chemistries and hence different cooling rates. The method used to implement the cooling function into CFDLIB uses the assumption that cooling dominates over heating inside the cloud. The only manifestation of heating is the minimum temperature attributable to diffuse cosmic ray heating. A more thorough evaluation of both cooling and heating processes would make for better models.

In the ISM, head-on collisions are rare. The consideration of obliquely colliding flows provides another basis for future study. Further consideration of the effects of altering the flow speeds is also warranted. Faster flows are expected to be more disruptive, and as such may lead to faster fragmentation of the disk. Indeed, the NTSI shows a much faster growth for the $v_i = 7.5\,km\,s^{-1}$ models than for the $v_i = 5\,km\,s^{-1}$ models. Stronger shocks may prove disruptive enough to prevent the coalescence of dense filaments into collapsing clumps. Another obvious omission from this work is the consideration of magnetic fields. As the instability grows, any magnetic field lines embedded in the gas would become tangled, providing a support mechanism against collapse. A more complete model will allow for ionization of atomic species and the presence of magnetic fields.

# CHAPTER 6
# CONCLUDING REMARKS

The study of the interstellar medium involves many difficulties. Observational efforts are hindered by a lack of time resolution and projection effects onto the two dimensional celestial sphere. Analytic studies of the ISM are restricted to limiting cases by its nonlinear nature. Computational simulation remains as the best tool for developing theoretical models of the ISM. In this dissertation, I have described my efforts to use computational simulations to examine two very different types of instabilities. The first was an interfacial instability driven by self-gravity. Simulations of this instability were begun from a state of hydrodynamic equilibrium to isolate its behavior. The second instability was a dynamic instability which occurs when supersonic gas streams collide. Due to the computational techniques employed, I was able to consider both static and supersonic problems with the same code. In this final chapter, I summarize the main results from the previous chapters and comment on further work to be done.

## 6.1 The Self-Gravity Interfacial Instability

Any planar interface of discontinuous density is unstable due to self-gravity. I have followed up the study by HWL by modeling the SGI in two dimensions to test the theoretical predictions and examine the nonlinear growth. Simulations were performed in the limit of a hydrostatic, incompressible, adiabatic gas. In this regime, the theoretical predictions hold up very well. The simulations confirm that the growth rate for the SGI is independent from the perturbation wavelength. The experimental growth rates agree well with predictions (see Table 3.3).

The SGI exhibits behavior that is in some ways very comparable to the RT instability but in other ways is very different. Both act to destabilize an interface of discontinuous density; the SGI in the presence of self-gravity, and the RT instability when a dense gas is accelerated into a tenuous gas. Both instabilities preserve the perturbation wavelength well into the nonlinear regime. Otherwise, the two develop in very different manners. The growth of the SGI is characterized by thin fingers of tenuous material streaming into the denser material. In the case of an interface with a low density ratio, the dense medium is displaced very little. The RT instability develops in the opposite manner. Thin, dense columns stream into the tenuous medium. When the RT instability acts upon interfaces with different density ratios, the growth rate changes, but the resultant morphologies remain very much the same. The SGI gives rise to very different morphologies when the density ratio is altered. The current results indicate that the SGI growth accelerates in the nonlinear phase; whereas, the RT growth rate slows in the nonlinear regime. Despite these differences, the SGI and the RT instability give rise to similar structures under the proper conditions. A larger density ratio at the interface leads to a greater similarity among SGI and RT models.

The models presented in chapter 3 represent the first computational study of the SGI. Further research will expand the parameter space of the study. In particular, a greater variety of density ratios is desirable. Larger grids will allow simulations to run for a longer time without the incitation of boundary effects. Once the SGI is well understood in the incompressible, static limit, restrictions on the models will be loosened to incorporate additional physics. The ultimate goal is to understand the role the SGI may play in the ISM when coupled with other instabilities and in the presence of dynamic forces. Density interfaces are ubiquitous in the ISM, so the SGI should be widespread. The question remains as to whether conditions anywhere in the

ISM are such that the SGI growth rate is not dominated by some other dynamically, thermodynamically, or magnetically driven process.

## 6.2 The Nonlinear Thin Shell Instability

A dense disk bounded by accretion shocks is unstable due to the continuous ram pressure from incoming flows and efficient cooling within the disk. Models done in both Cartesian and cylindrical geometries demonstrate the controlling influence of thermodynamics over the evolution of the instability. The Cartesian models presented in chapter 4 showed very little difference between non-gravitating and gravitating models, but large differences are apparent amongst models with different cooling rates. A perturbed slab with strong cooling is prone to the development of short wavelength modes which override the initial perturbation. Slabs with weak cooling tend to preserve the perturbation wavelength for long times. Short wavelength modes are suppressed. In all cases, the slab density decreases as the gas is spread over a larger volume. Streaming motions within the slab give rise to filaments and vortices. The slab ultimately fragments into a few dense islands of material, but no collapsing clumps are observed.

Unlike the Cartesian models, the cylindrical models show large differences between non-gravitating and gravitating models. The combined effects of geometric focusing and self-gravity give rise to dense filaments along the symmetry axis. Clumps within the filaments show signs of collapse. Thus, the collision of supersonic flows gives rise to collapsing regions which would otherwise not be gravitationally bound, provided the post-shock flows are allowed to cool. A lower cooling rate appears to quicken the development of a collapsing clump, but this result is clouded by the boundary effects inherent in a grid code. Further examination is needed with larger grids and a greater range of inflow velocities. Faster flows are more likely to rend apart any accumulation of material before collapse can commence.

By and large, the results of HSWK and KW are reproducible when different cooling rates are used. A notable exception is the assertion by KW that adiabatic flows exhibit the NTSI, provided the shock compression is a least a factor of ten. I find no evidence for the NTSI in any adiabatic models. I attribute my results to either a lack of sufficient resolution or inherent differences between the collisions of finite clouds considered by KW and the continuous inflow used in my models. Comparisons to the theory of Vishniac (1994) are difficult since he considered only isothermal flows. His description of the NTSI as a purely nonlinear phenomenon is supported by failed attempts to produce the instability in the linear regime.

## 6.3 Further Considerations

A great deal of work remains to be done to fully understand instabilities in the ISM. If a comprehensive model for the ISM is to be formed, simulations need to continue along two complementary paths. Models designed for the careful study of particular phenomena (such as the SGI and the NTSI) are needed to better understand the underlying physical processes. At the same time, more complicated models that are more representative of the ISM are needed. Thermodynamic properties must be carefully considered, as must mechanisms for driving and dissipating turbulence on multiple scales. Complex models which incorporate numerous physical processes will provide insight into the evolution of the ISM. Simpler models of isolated physical processes will allow the proper interpretation of the complex models.

The implementation of a comprehensive model is still far off. A major complication is that the chemistry, thermodynamics, and other characteristics of the ISM vary on different length scales. The incorporation of multiple generations of star formation, and the outflows and supernovae which result, is a Herculean task. Codes utilizing a three dimensional adaptive mesh framework will be crucial. Fortunately, new technologies are driving rapid advances in both computational and observational techniques. Through the combined work of many researchers, the common goal of understanding the ISM and the star formation process may be realized.

# REFERENCES

Adams, J.C., 1989, *Applied Math. and Comp.*, **34**, 113

Adams, J.C., 1991, *Applied Math. and Comp.*, **43**, 79

Addessio, F.L., Baumgardner, J.R., Dukowicz, J.K, Johnson, N.L., Kashiwa, B.A., Rauenzahn, R.M., and Zemach, C. 1992, *CAVEAT: A Computer Code for Fluid Dynamics Problems with Large Distortion and Internal Slip*, LANL document LA-10613-MS

Ballesteros-Paredes, J., Vázquez-Semadeni, E., and Scalo, J. 1999a, *Ap.J.*, **515**, 286

Ballesteros-Paredes, J., Hartmann, L., and Vázquez-Semadeni, E. 1999b, *Ap.J*, **527**, 285

Bergin, E.A., Melnick, G.J., Stauffer, J.R., Ashby, M.L.N., Chin, G., Erikson, N.R., Goldsmith, P.F., Harwit, M., Howe, J.E., Kleiner, S.C., Koch, D.G., Neufeld, D.A., Patten, B.M., Plume, R., Schieder, R., Snell, R.L., Tolls, V., Wang, Z., Winnewisser, G., and Zhang, Y.F. 2000, *Ap.J*, **539**, L129

Bernstein, I.B., Frieman, E.A., Kruskal, M.D., and Kulsrud, R.M. 1958, *Proc. R. Soc. London A*, **244**, 17

Binney, J., and Tremaine, S. 1987, *Galactic Dynamics* (Princeton: Princeton University Press)

Blitz, L. 1993, In *Protostars and Planets III*, eds. E.H. Levy and J.I. Lunine (Tuscon: University of Arizona Press)

Briggs, W.L. 1987, *A Multigrid Tutorial* (Philadelphia: SIAM)

Calder, A.C., Fryxell, B., Rosner, R., Dursi, L.J., Olson, K., Ricker, P.M., Timmes, F.X., Zingale, M., MacNeice, P., and Tufo, H.M. 2000, *BAAS*, **32**, 1537

Chandrasekhar, S. 1939, *An Introduction to the Study of Stellar Structure* (University of Chicago Press)

Chandrasekhar, S. 1961, *Hydrodynamic and Hydromagnetic Stability* (Oxford: Oxford University Press)

Chandrasekhar, S., and Münch, G. 1952, *Ap.J.*, **115**, 103

Crutcher, R.M. 1999, *Ap.J.*, **520**, 706

Draine, B.T., and McKee, C.F. 1993, *AAR&A*, **31**, 373

Elmegreen, B.G. 1993a, In *Protostars and Planets III*, eds. E.H. Levy and J.I. Lunine (Tuscon: University of Arizona Press)

Elmegreen, B.G. 1993b, *Ap.J.*, **419**, L29

Elmegreen, B.G., and Lada, C.J. 1977, *Ap.J.*, **214**,725

Falgarone, E., and Puget, J.-L. 1986, *Astronomy and Astrophysics*, **162**, 235

Field, G.B. 1965, *Ap.J.*, **142**, 531

Fleck, R.C. 1996, *Ap.J.*, **458**, 739

Frank, A., Jones, T.W., Ryu, D., and Gaalaas, J.B. 1996, *Ap.J.*, **460**, 777

Harlow, F.H. and Amsden, A.A. 1971, *Fluid Dynamics*, LASL monograph LA-4700

Hirt, C.W., Amsden, A.A., and Cook, J.L. 1974, *J.Comp.Phys.*, **14**, 227

Hunter, J.H. Jr. 1979, *Ap.J*, **233**, 946

Hunter, J.H. Jr., and Fleck, R.C. 1982, *Ap.J.*, **256**, 505

Hunter, J.H. Jr., Sandford, M.T., Whitaker, R.W., and Klein, R.I. 1986, *Ap.J.*, **305**, 309 (HSWK)

Hunter, J.H. Jr., and Whitaker, R.W. 1987, In *Chaotic Phenomena in Astrophysics*, eds. J.R. Buchler and H.K. Eichhorn (Annals of the New York Academy of Science, 497)

Hunter, J.H. Jr., and Whitaker, R.W. 1989, *Ap.J.Suppl*, **71**, 777

Hunter, J.H. Jr., Whitaker, R.W., and Lovelace, R.V.E. 1997, *Ap.J.*, **482**, 852 (HWL)

Hunter, J.H. Jr., Whitaker, R.W., and Lovelace, R.V.E. 1998, *Ap.J.*, **508**, 680

Jeans, J.H. 1929, *Astronomy and Cosmogony, 2nd ed.* (Cambridge: Cambridge University Press)

Jun, B.-I., Norman, M.L., and Stone, J.M. 1995, *Ap.J.*, **453**, 332

Kashiwa, B.A., Padial, N.T., Rauenzahn, R.M., and Vanderheyden, W.B. 1994, In *Numerical Methods in Multiphase Flows*, eds. C.T. Crowe, R. Johnson, A. Prosperetti, M. Sommerfeld, and Y. Tsuji (FED-Vol. 185, ASME, New York)

Klein, R.I., and Woods, D.T. 1998, *Ap.J.*, **497**, 777 (KW)

Klessen, R.S., Heitsch, F., and Mac Low,M.-M. 2000, *Ap.J.*, **535**, 887

Lada, C.J., and Shu, F.H. 1990, *Science*, **248-4955**, 564

Lada, E.A., Strom, K.M., and Myers, P.C. 1993, In *Protostars and Planets III*, eds. E.H. Levy and J.I. Lunine (Tuscon: University of Arizona Press)

Larson, R.B. 1981, *MNRAS*, **194**, 809

Leisawitz, D., Bash, F.N., and Thaddeus, P. 1989, *Ap.J.Suppl.*, **70**, 731

Miniati, F., Jones, T.W., Ferrara, A., and Ryu, D. 1997, *Ap.J.*, **491**, 216

Murata, Y., Kawabe, R., Ishiguro, M., Morita, K., Kasuga, T., Takano, T., and Hasegawa, T. 1990, *Ap.J.*, **359**, 125

Murray, S.D., White, S.D.M., Blondin, J.M., and Lin, D.N.C. 1993, *Ap.J*, **407**, 588

Neufeld, D.A., Lepp, S., and Melnick, G.J. 1995, *Ap.J. Suppl.*, **100**, 132 (NLM)

Parker, E.N. 1966, *Ap.J.*, **145**, 811

Press, W.H., Teukolsky, S.A., Vetterling, W.T., and Flannery, B.P. 1992, *Numerical Recipes in FORTRAN: the art of scientific computing 2nd edition* (New York: Cambridge University Press)

Stevens, I.R., Blondin, J.M., and Pollack, A.M.T. 1992, *Ap.J.*, **386**, 265 (SBP)

Stone, M.E. 1970a, *Ap.J.*, **159**, 277

Stone, M.E. 1970b, *Ap.J.*, **159**, 293

Tohline, J.E., Bodenheimer, P.H., and Christodoulou, D.M. 1987, *Ap.J.*, **322**, 787

Ungerechts, H., and Thaddeus, P. 1987, *Ap.J.Suppl.*, **63**, 645

van Leer, B. 1977, *J.Comp.Phys.*, **23**, 276

Vázquez-Semadeni, E., Passot, T., and Pouquet, A. 1996, *Ap.J.*, **473**, 881

Vázquez-Semadeni, E., Ostriker, E.C., Passot, T., Gammie, C.F., and Stone, J.M. 2000, In *Protostars and Planets IV*, eds. V. Mannings, A.P. Boss, and S.S. Russell (Tuscon: University of Arizona Press)

Vietri, M., Ferrara, A., and Miniati, F. 1997, *Ap.J.*, **483**, 262

Vishniac, E.T. 1994, *Ap.J.*, **428**, 186

von Weizsäcker, C.F. 1951, *Ap.J*, **114**, 165

Weymann,R.J. 1960, *Ap.J.*, **132**, 452

Whitworth, A.P., and Clarke, C.J. 1997, *MNRAS*, **291**, 578

Williams, J.P. 1999, In *Interstellar Turbulence*, eds. J. Franco and A. Carramiñana, (Cambridge: Cambridge University Press)

Youngs, D.L. 1984, *Physica D*, **12**, 32

# BIOGRAPHICAL SKETCH

Robert Michael Hueckstaedt was born and raised in northern Illinois. The third child of Robert and Deanna Hueckstaedt, he developed a passion for science at an early age. Upon finishing high school, he enrolled in the physics program at the University of Illinois at Urbana-Champaign. He found that among the many disciplines available for study, particle physics and astrophysics best captured his interest. Ultimately, astrophysics won out. Seeking a large department with a diversity of research topics (and a warmer climate), Robert choose to continue his scholastic career at the University of Florida.

At UF, Robert sought to enhance his skills in the field of computational science. His first foray into the field came in the form of a summer study of the virial behavior of an N-body system performed with Dr. H.C. Smith Jr. Shortly thereafter, he began working with Dr. J.H. Hunter Jr. in adapting a hydrodynamics code for astrophysical use. Thus began the journey culminating in this work. Along the way, Robert has spent time at Los Alamos National Laboratory and Goddard Space Flight Center honing his craft. He looks forward to continuing his studies of the hydrodynamical state of the of the ISM, as well as broadening his horizons through future endeavors.

I certify that I have read this study and that in my opinion it conforms to acceptable standards of scholarly presentation and is fully adequate, in scope and quality, as a dissertation for the degree of Doctor of Philosophy.

James H Hunter, Jr.

James H. Hunter Jr., Chairman
Professor of Astronomy

I certify that I have read this study and that in my opinion it conforms to acceptable standards of scholarly presentation and is fully adequate, in scope and quality, as a dissertation for the degree of Doctor of Philosophy.

Haywood C. Smith Jr.

Haywood C. Smith Jr.
Associate Professor of Astronomy

I certify that I have read this study and that in my opinion it conforms to acceptable standards of scholarly presentation and is fully adequate, in scope and quality, as a dissertation for the degree of Doctor of Philosophy.

Robert E. Wilson

Robert E. Wilson
Professor of Astronomy

I certify that I have read this study and that in my opinion it conforms to acceptable standards of scholarly presentation and is fully adequate, in scope and quality, as a dissertation for the degree of Doctor of Philosophy.

Elizabeth A. Lada

Elizabeth A. Lada
Associate Professor of Astronomy

I certify that I have read this study and that in my opinion it conforms to acceptable standards of scholarly presentation and is fully adequate, in scope and quality, as a dissertation for the degree of Doctor of Philosophy.

Steven L. Detweiler
Professor of Physics

This dissertation was submitted to the Graduate Faculty of the Department of Astronomy in the College of Liberal Arts and Sciences and to the Graduate School and was accepted as partial fulfillment of the requirements for the degree of Doctor of Philosophy.

August 2001

Dean, Graduate School